

BOSTON UNIVERSITY  
GRADUATE SCHOOL OF ARTS AND SCIENCES

Dissertation

**MEASUREMENT OF THE MAGNETIC ANOMALY OF  
THE MUON TO X PARTS PER BILLION IN RUN 1 OF  
THE FERMILAB MUON  $g - 2$  EXPERIMENT**

by

**NICHOLAS BRENNAN KINNAIRD**

B.S., University of Texas at Austin, 2013  
B.S., University of Texas at Austin, 2013  
M.A., Boston University, 2016

Submitted in partial fulfillment of the  
requirements for the degree of  
Doctor of Philosophy

2019

© 2019 by  
NICHOLAS BRENNAN KINNAIRD  
All rights reserved

Approved by

First Reader

---

B. L. Roberts, PhD  
Professor of Physics

Second Reader

---

R. M. Carey, PhD  
Professor of Physics

## **Dedication**

I dedicate this thesis to

## Acknowledgments

Here go all your acknowledgments. You know, your advisor, funding agency, lab mates, etc., and of course your family.

As for me, I would like to thank Jonathan Polimeni for cleaning up old LaTeX style files and templates so that Engineering students would not have to suffer typesetting dissertations in MS Word. Also, I would like to thank IDS/ISS group (ECE) and CV/CNS lab graduates for their contributions and tweaks to this scheme over the years (after many frustrations when preparing their final document for BU library). In particular, I would like to thank Limor Martin who has helped with the transition to PDF-only dissertation format (no more printing hardcopies – hooray !!!)

The stylistic and aesthetic conventions implemented in this LaTeX thesis/dissertation format would not have been possible without the help from Brendan McDermot of Mugar library and Martha Wellman of CAS.

Finally, credit is due to Stephen Gildea for the MIT style file off which this current version is based, and Paolo Gaudiano for porting the MIT style to one compatible with BU requirements.

Janusz Konrad  
Professor  
ECE Department

**MEASUREMENT OF THE MAGNETIC ANOMALY OF  
THE MUON TO X PARTS PER BILLION IN RUN 1 OF  
THE FERMILAB MUON  $g - 2$  EXPERIMENT**

(Order No. )

**NICHOLAS BRENNAN KINNAIRD**

Boston University, Graduate School of Arts and Sciences, 2019

Major Professor: B. L. Roberts, Professor of Physics

**ABSTRACT**

This abstract was copied from my departmental seminar, and it needs to be updated for my thesis: One of the few indications for new physics is the discrepancy between the theoretical and experimental values for the anomalous magnetic moment of the muon. There is a 3 to 4 sigma discrepancy between theory and the last experimental measurement held at Brookhaven National Laboratory in 2001, which measured the muon g-2 to 540 parts per billion. This discrepancy has been consistent for many years now with ever improving theoretical calculations and other experimental measurements. In order to resolve or confirm this difference, a new experiment is underway at Fermilab to measure the muon g-2 to 4 times higher precision at 140 ppb. Muon g-2 at Fermilab gathered its first production data in 2018, and is currently taking data now. I will describe the principles of the experiment and detail two specific parts of the analysis that I have been involved in. These include track fitting and precession frequency analysis of the Run 1 data.

# Contents

<b>1</b>	<b>Introduction</b>	<b>1</b>
1.1	Magnetic moments of particles . . . . .	2
1.2	Standard Model contributions to $a_\mu$ . . . . .	3
1.2.1	QED . . . . .	3
1.2.2	Electroweak . . . . .	4
1.2.3	Hadronic . . . . .	5
1.2.4	Combined Standard Model value . . . . .	9
1.3	Experimental value of $a_\mu$ and discrepancy with $a_\mu^{\text{SM}}$ . . . . .	11
1.4	Beyond the Standard Model and the purpose of E989 . . . . .	11
<b>2</b>	<b>Principal Techniques of E989</b>	<b>15</b>
2.1	Measuring $\omega_a$ . . . . .	17
2.2	Measuring the magnetic field . . . . .	22
2.3	Production of polarized muons . . . . .	27
2.4	Injection of muons . . . . .	30
2.5	Storage of muons . . . . .	31
2.5.1	Kicker . . . . .	34
2.5.2	Electrostatic quadrupoles . . . . .	36
2.6	Muon beam dynamics . . . . .	38
2.6.1	Coherent betatron oscillation . . . . .	41
2.6.2	Beam debunching . . . . .	43
2.7	Corrections to $\omega_a$ . . . . .	44

2.7.1	Electric field correction . . . . .	44
2.7.2	Pitch correction . . . . .	47
2.8	Run 1 in E989 . . . . .	50
<b>3</b>	<b>Detector Systems</b>	<b>54</b>
3.1	Auxiliary detectors . . . . .	54
3.1.1	T0 . . . . .	54
3.1.2	Inflector Beam Monitoring System . . . . .	55
3.1.3	Fiber harps . . . . .	56
3.2	Calorimeters . . . . .	57
3.2.1	Requirements and systematic effects . . . . .	58
3.2.2	Hardware . . . . .	59
3.2.3	Laser calibration system . . . . .	61
3.3	Straw trackers . . . . .	62
3.3.1	Tracker readout electronics . . . . .	67
<b>4</b>	<b>Track Reconstruction and Analysis</b>	<b>73</b>
4.1	Track finding . . . . .	73
4.2	Track fitting . . . . .	76
4.2.1	Error propagation and coordinate systems . . . . .	76
4.2.2	$\chi^2$ minimization . . . . .	84
4.2.3	Fits to idealized tracks in vacuum . . . . .	87
4.2.4	Material correlations . . . . .	88
4.2.5	Fits to simulated tracks including material effects . . . . .	92
4.2.6	Left-right ambiguity and fit modes . . . . .	100
4.2.7	Fits to tracks from data and comparison with Monte-Carlo . .	102
4.3	Track extrapolation . . . . .	105
4.4	Muon beam measurements . . . . .	105

<b>5</b>	<b><math>\omega_a</math> Measurement</b>	<b>114</b>
5.1	Reconstruction of decay positron hits . . . . .	114
5.2	Construction of positron hit energy and time spectra . . . . .	120
5.2.1	Pileup subtraction . . . . .	123
5.2.2	Ratio Method . . . . .	132
5.3	Fitting the data . . . . .	138
5.3.1	CBO terms . . . . .	142
5.3.2	VW term . . . . .	144
5.3.3	Lost muons . . . . .	147
5.3.4	Fit procedures and parameters . . . . .	154
5.4	Fit results . . . . .	155
5.4.1	Individual calorimeter fits . . . . .	162
5.4.2	Fit start and end scans . . . . .	167
5.4.3	Energy threshold scans . . . . .	174
5.4.4	Fits to bunch number . . . . .	176
5.4.5	Fits to many random seeds . . . . .	178
5.5	Systematic errors . . . . .	181
5.5.1	Pileup systematic errors . . . . .	181
5.5.2	Gain systematic errors . . . . .	191
5.5.3	CBO systematic errors . . . . .	191
5.5.4	Lost muon systematic errors . . . . .	191
5.5.5	Ratio construction systematic errors . . . . .	196
5.5.6	Binning systematic errors . . . . .	196
5.5.7	Random seed systematic errors . . . . .	197
5.5.8	Systematic error summary . . . . .	197

<b>6 Conclusion</b>	<b>198</b>
6.1 Run 1 value of $a_\mu$ . . . . .	198
<b>A Straw measurement angular correction</b>	<b>199</b>
<b>B Ratio Method Derivation</b>	<b>202</b>
B.1 Ratio form and function . . . . .	202
B.2 Ratio errors . . . . .	207
<b>C Pileup Modified Errors</b>	<b>208</b>
C.1 Pileup errors for the ratio function . . . . .	211
<b>D Fit Result Correlation Matrices</b>	<b>213</b>

# List of Tables

2.1	Uncertainties in the magnetic field measurement . . . . .	27
2.2	Muon beam frequencies in the E989 experiment . . . . .	40
2.3	Run 1 datasets . . . . .	53
4.1	Run 1 dataset muon beam parameters . . . . .	111
5.1	Parameters used in the construction of $\omega_a$ time spectra . . . . .	120
5.2	Dataset CBO frequency model parameters . . . . .	143
5.3	Asymmetry values in Run 1 datasets with VW time randomization .	146
5.4	Lost muon cuts . . . . .	149
5.5	Fit procedure parameters . . . . .	155
5.6	Fit results for Run 1 precession frequency analysis datasets . . . . .	159
5.7	Random seed fit results . . . . .	178
5.8	Uncertainties in the precession frequency measurement . . . . .	181
5.9	Systematic error due to pileup amplitude . . . . .	187
5.10	Systematic error due to pileup time shift . . . . .	189
5.11	Systematic error due to fixed pileup energy scale factor . . . . .	190
5.12	Total pileup systematic errors . . . . .	191
5.13	Effect on fitted R value due to lost muon cuts in the 9d and Endgame datasets . . . . .	192
5.14	Systematic error due to fixed $\kappa_{loss}$ . . . . .	194

C.1 Number of doublet counts added to pileup histogram from shadow method . . . . .	209
--	-----

# List of Figures

1.1	QED diagrams contributing to the magnetic moment . . . . .	4
1.2	Electroweak diagrams contributing to the magnetic moment . . . . .	5
1.3	First order hadronic vacuum polarization diagram contributing to the magnetic moment . . . . .	7
1.4	HVP calculations for $a_\mu$ from various groups . . . . .	8
1.5	Hadronic light-by-light diagrams contributing to the magnetic moment	9
1.6	Comparison between theoretical and experimental values for $a_\mu$ . . .	10
1.7	General diagram for new physics . . . . .	13
1.8	Citations for E821 publications vs year . . . . .	13
2.1	Feynman diagram for muon decay . . . . .	18
2.2	Muon decay for maximum and minimum energy decay positrons . .	18
2.3	Number distribution and asymmetry for muon decay in the muon rest frame and lab frame . . . . .	20
2.4	$g - 2$ time spectrum example . . . . .	21
2.5	Magnet cross section . . . . .	23
2.6	FID signal . . . . .	24
2.7	Azimuthally averaged magnetic field sample . . . . .	25
2.8	Fermilab accelerator layout for muon delivery to E989 . . . . .	28
2.9	Fermilab accelerator pulse train . . . . .	29
2.10	Muon injection point through inflector . . . . .	32
2.11	Superconducting inflector magnet . . . . .	32

2.12	The E989 experiment . . . . .	33
2.13	Vacuum chamber map . . . . .	35
2.14	Electrostatic quadrupoles installed in a vacuum chamber . . . . .	37
2.15	Electrostatic quadrupole potentials . . . . .	38
2.16	Tune plane . . . . .	41
2.17	Coherent betatron oscillation . . . . .	43
2.18	Beam debunching fast rotation . . . . .	45
2.19	Pitching beam motion . . . . .	48
2.20	Electrostatic quadrupole high voltage traces . . . . .	52
3.1	T0 counter and pulses . . . . .	55
3.2	IBMS Models . . . . .	56
3.3	IBMS Positions . . . . .	56
3.4	Fiber harp and measurement . . . . .	57
3.5	Calorimeters . . . . .	60
3.6	SiPM pulse . . . . .	61
3.7	Straw tracker drift circles . . . . .	64
3.8	Tracker module . . . . .	65
3.9	Tracker module coordinate system . . . . .	66
3.10	Model view of tracker station . . . . .	67
3.11	Muon perspective view of tracker station . . . . .	68
3.12	Tracker ASDQs and associated components . . . . .	70
3.13	Tracker feedthrough board . . . . .	71
3.14	Tracker readout boards and housing . . . . .	71
3.15	Front-end tracker electronics readout chain . . . . .	72
4.1	Track candidate selection . . . . .	75
4.2	Vertical and radial magnetic fields calculated in Opera2D . . . . .	78

4.3	Free and surface tracking coordinate systems . . . . .	80
4.4	Tracker reference frame . . . . .	80
4.5	Transport and error matrices for straw tracker planes . . . . .	82
4.6	Natural tracker measurement system . . . . .	84
4.7	P value and $\chi^2$ distribution for fitted tracks in vacuum . . . . .	88
4.8	Track parameter truth pulls for fitted tracks in vacuum . . . . .	89
4.9	Material scattering error in tracker . . . . .	90
4.10	$\chi^2$ for fitted tracks including material effects but no correlations . . .	91
4.11	P value and $\chi^2$ distribution for fitted tracks in the $g - 2$ Geant4 simulation with material effects included . . . . .	93
4.12	Simulated true energy loss vs Geant predicted energy loss for tracks .	94
4.13	Track parameter truth pulls for fitted tracks in the $g - 2$ Geant4 simulation with material effects included . . . . .	95
4.14	Number of iterations for the track fitting to converge . . . . .	96
4.15	Number of planes hit for fitted tracks . . . . .	96
4.16	Fitted track momentum distribution and corresponding residuals to truth . . . . .	97
4.17	Fitted track vertical and horizontal momenta and corresponding residuals to truth . . . . .	98
4.18	Fitted track vertical and horizontal positions and corresponding residuals to truth . . . . .	99
4.19	P value distribution for fitted tracks in data . . . . .	103
4.20	Fitted tracks in data compared to Monte-Carlo, track times and total momentum . . . . .	103
4.21	Fitted tracks in data compared to Monte-Carlo, radial and vertical momentum and position distributions . . . . .	104

4.22	Birds eye view of extrapolation in ring . . . . .	106
4.23	Extrapolated muon beam distribution cross-section . . . . .	109
4.24	Muon beam radial and vertical distributions . . . . .	109
4.25	Muon beam radial and vertical distributions as a function of time in-fill	110
4.26	Muon beam radial and vertical distribution means as a function of time in-fill . . . . .	110
4.27	CBO frequency as a function of time . . . . .	112
4.28	CBO amplitude as a function of time . . . . .	113
5.1	Template fit to SiPM trace . . . . .	116
5.2	In-fill gain function fit for a single calorimeter crystal . . . . .	118
5.3	Calorimeter cluster from SiPM traces fit with templates . . . . .	119
5.4	Sample energy spectrum . . . . .	121
5.5	Determination of optimal energy threshold . . . . .	122
5.6	Pileup example . . . . .	125
5.7	Shadow pileup method . . . . .	127
5.8	Cluster energies vs pileup energies . . . . .	129
5.9	Non-corrected and pileup corrected cluster energies . . . . .	130
5.10	Cluster energies divided by pileup energies . . . . .	130
5.11	Cluster times above 3.5 GeV . . . . .	131
5.12	Pileup time spectrum above threshold . . . . .	132
5.13	Ratio formation functions . . . . .	136
5.14	Cancellation of effect in Ratio Method versus frequency . . . . .	137
5.15	FFT of five parameter fit residuals . . . . .	139
5.16	FFT of three parameter ratio fit residuals . . . . .	141
5.17	VW amplitude resonance in the 60h dataset . . . . .	144
5.18	VW envelope in Ratio Method Toy MC data with and without FR effect	145

5.19	Lost muon $\Delta t$ and energy deposition distributions . . . . .	148
5.20	Lost muon $\Delta t_{12}$ distribution as a function of time in-fill . . . . .	150
5.21	Deuteron population at late times . . . . .	151
5.22	Final $\Delta t_{12}$ distribution for selected lost muons . . . . .	152
5.23	Lost muon triples spectrum compared to quadruples and accidental background . . . . .	152
5.24	Single random seed fits to calorimeter summed data of Run 1 precession frequency analysis datasets . . . . .	158
5.25	Pulls and FFT of residuals for the ratio fit to the 60h dataset . . . .	160
5.26	60h ratio fit correlation matrix . . . . .	161
5.27	$\chi^2/\text{NDF}$ versus calorimeter number . . . . .	163
5.28	$R$ versus calorimeter number . . . . .	163
5.29	Endgame fit parameters versus calorimeter number . . . . .	165
5.30	Endgame fit parameters versus calorimeter number . . . . .	166
5.31	Examples of fit start scans when effects are improperly accounted for in fitting . . . . .	167
5.32	$\chi^2/\text{NDF}$ and $R$ versus fit start time . . . . .	170
5.33	Fit start scans for free parameters in the Endgame dataset . . . .	172
5.34	$R$ versus fit end time . . . . .	173
5.35	$R$ versus energy threshold . . . . .	175
5.36	$R$ versus bunch number . . . . .	177
5.37	$\chi^2$ 's for fits to many random seeds . . . . .	179
5.38	$R$ values for fits to many random seeds . . . . .	180
5.39	Pileup shadow dead time scan without automatic pileup amplitude scaling . . . . .	183
5.40	Pileup shadow dead time scan with automatic pileup amplitude scaling	184

5.41	Pileup shadow gap time scan with automatic pileup amplitude scaling	185
5.42	Pileup multiplier scan . . . . .	187
5.43	Pileup time-shift scan . . . . .	188
5.44	Pileup energy scale scan . . . . .	190
5.45	Lost muon $\Delta t_{13}$ distribution as a function of time in-fill . . . . .	193
5.46	Scan over fixed $\kappa_{loss}$ . . . . .	194
5.47	Fractional muon losses in the analyzed Run 1 datasets . . . . .	195
A.1	Angular correction for measured DCAs . . . . .	200
D.1	HighKick ratio fit correlation matrix . . . . .	214
D.2	9d ratio fit correlation matrix . . . . .	215
D.3	Endgame ratio fit correlation matrix . . . . .	216

# List of Abbreviations

ADT	.....	artificial dead time
ASDQ	.....	Amplifier Shaper Discriminator with charge (Q)
ASIC	.....	application specific integrated circuit
BNL	.....	Brookhaven National Laboratory
BSM	.....	beyond the standard model
CBO	.....	coherent betatron oscillation
E821	.....	Brookhaven Muon $g - 2$ Experiment
E989	.....	Fermilab Muon $g - 2$ Experiment
EW	.....	electroweak
FID	.....	free-induction decay
FNAL	.....	Fermi National Accelerator Laboratory
Geane	.....	Geometry and Error Propagation
Geant	.....	Geometry and Tracking
HLbL	.....	hadronic light-by-light
HVP	.....	hadronic vacuum polarization
IBMS	.....	inflector beam monitoring system
MIP	.....	minimum-ionizing particle
NMR	.....	nuclear magnetic resonance
PCB	.....	printed circuitry board
PMT	.....	photo-multiplier tube
ppb	.....	parts per billion
ppm	.....	parts per million
ppt	.....	parts per trillion
QCD	.....	quantum chromodynamics
QED	.....	quantum electrodynamics
RMS	.....	root mean square
SDT	.....	shadow dead time
SGT	.....	shadow gap time
SiPM	.....	silicon photo-multiplier
SM	.....	Standard Model
STDP	.....	short-term double pulse
VW	.....	vertical waist
WFD	.....	waveform digitizer

# Chapter 1

## Introduction

The prevailing theory of particle physics, the Standard Model (SM), has had tremendous success in describing our universe. It has been used to predict and explain a wide variety of phenomena, particle properties, and interactions to great precision. However, in spite of its success in explaining nearly all experimental results, there remain unanswered questions about our universe. Some of these include the matter-antimatter asymmetry, the source of mass for the neutrinos, the existence of dark matter, and reconciling general relativity and quantum mechanics. Many particle physics experiments around the world are being devised and conducted in order to shed light on these questions and improve our understanding of reality. One such experiment is the Fermilab Muon  $g - 2$  Experiment (E989), underway at the Fermi National Accelerator Laboratory (FNAL) located in Batavia, Illinois.

I have been a part of the E989 experiment since I began my graduate degree six years ago. This dissertation will describe the E989 experiment and the work which I have done for it in detail. Chapter 1 will provide experimental and theoretical background to the experiment, as well its motivation. Chapter 2 will describe the experimental principle and specifics of muon production and storage. Chapter 3 will describe the various detector systems. Chapter 4 will describe the straw tracking reconstruction, including the track fitting algorithm that I developed, as well as some analysis results. Chapter 5 will describe the precession frequency measurement portion of the experiment, and detail my analysis results from data taken in the

experiment’s first run in 2018. Chapter 6 will conclude the thesis and the results contained within.

## 1.1 Magnetic moments of particles

In order to understand the purpose of the Fermilab Muon  $g - 2$  Experiment, first we need to understand the meaning of the  $g$  in  $g - 2$ , which is what the experiment is measuring. All particles have intrinsic properties. One property of charged particles is the magnetic dipole moment.<sup>1</sup> This property of a particle is related to its spin through the equation

$$\vec{\mu} = g \frac{q}{2m} \vec{s}, \quad (1.1)$$

where  $\vec{\mu}$  is the magnetic dipole moment of a particle,  $\vec{s}$  is its spin vector,  $m$  is its mass,  $q = \pm e$  where  $e$  is the elementary charge, and  $g$  is the so called “Landé g-factor”.  $g$  is a measurable and predictable constant. Since the torque on a particle in a magnetic field is

$$\vec{N} = \vec{\mu} \times \vec{B}, \quad (1.2)$$

the rate at which a particle’s spin precesses in a magnetic field will depend on  $g$ . This is one of the key physics principles in the E989 experiment as will be discussed later.

In a Dirac theory,  $g$  is equal to 2 for spin- $\frac{1}{2}$  particles with no internal structure [1]. A simple derivation of this result is given in Reference [2]. However, even for these types of particles,  $g$  is not quite equal to 2. Motivated by early experimental measurement discrepancies such as the measurements of the hyperfine structure in hydrogen [3], in 1948 Schwinger calculated the first “radiative correction” to the electron magnetic moment [4]. In a quantum field theory, interactions of the particle

---

<sup>1</sup>*Magnetic dipole moment* and *magnetic moment* are equivalent when talking about particles.

with virtual particles in loops will contribute to the value of  $g$ . In this context, for charged leptons, it is convenient to recast the magnetic dipole moment formula as

$$\begin{aligned}\vec{\mu} &= 2(1+a)\frac{q}{2m}\vec{s}, \\ a &= \frac{g-2}{2},\end{aligned}\tag{1.3}$$

where  $a$  is called the “magnetic anomaly,” and contains all higher order corrections to  $g$ . The first correction to  $a$ , calculated by Schwinger, was  $a = \alpha/2\pi \approx 0.00116$ , where  $\alpha$  is the fine structure constant. By measuring  $a$ , the SM theory can be tested and extensions to it constrained. A precise measurement of the magnetic anomaly, or the anomalous magnetic moment of the muon, is the main goal of the Fermilab Muon  $g - 2$  Experiment.

## 1.2 Standard Model contributions to $a_\mu$

Any complete theory must agree with experimental observations. The latest theoretical predictions for the muon magnetic moment will be presented here. The contributions to  $a_\mu$  can be divided into three SM classes. These include the quantum-electrodynamics (QED) corrections purely from other leptons and photons, the electroweak (EW) corrections from interactions involving the weak force bosons  $W^\pm$  and  $Z^0$ , and the hadronic corrections from interactions with strongly-interacting hadrons:

$$a_\mu^{\text{SM}} = a_\mu^{\text{QED}} + a_\mu^{\text{EW}} + a_\mu^{\text{Had}}\tag{1.4}$$

### 1.2.1 QED

The QED contributions to  $a_\mu$  stem solely from loops with virtual leptons and photons. They are very well understood and have been calculated to very high order, having been calculated up to five-loop level from over 12,000 Feynman diagrams. This has



Figure 1.1: The first of many QED diagrams contributing to  $a$ . B is an external magnetic field. Feynman diagrams made with References [5, 6].

been done with both analytical and numerical methods. The first couple of diagrams, including the Dirac  $g = 2$  and Schwinger diagrams, are shown in Figure 1.1. The value is [7, 8]

$$a_\mu^{\text{QED}} = \sum_{n=1}^{\infty} C_n \left(\frac{\alpha}{\pi}\right)^n, \quad (1.5)$$

$$= (11658471.8971 \pm 0.0007) \times 10^{-10},$$

where in the first line  $a_\mu^{\text{QED}}$  is expressed as a perturbative expansion in the fine structure constant, and the value comes from the expansion up to  $n = 5$ .  $C_1 = 1/2$  is the Schwinger result mentioned previously, stemming from the diagram shown in Figure 1.1b. While over 99% of the value of  $a_\mu$  comes from the QED sector, the error is much smaller than the EW and hadronic contributions.

### 1.2.2 Electroweak

The electroweak contributions to  $a_\mu$  are known to two-loop level, with some three-loop parts estimated. The different one loop diagrams are shown in Figure 1.2. In even the simplest EW diagram propagators from both the leptons and EW gauge bosons will be included. Per usual Feynman rules, the propagators will contain the



Figure 1.2: First order weak diagrams contributing to  $a$ . B is an external magnetic field. Feynman diagrams made with References [5, 6].

masses of the interacting leptons and bosons. The heavy masses of the gauge bosons will produce contributions with characteristic scales of  $\sim (m_l/m_{Z^0,H,W^\pm})^2$ . Because the mass of the gauge bosons are so much larger than the muon, these processes are necessarily suppressed and the electroweak contributions to  $a_\mu$  are small. For this reason knowing these contributions only up to two loop level is sufficient, since higher order diagrams will be suppressed even further. To this degree of accuracy, the value of the electroweak contributions is [9, 10]

$$a_\mu^{\text{EW}} = (15.12 \pm 0.01) \times 10^{-10}, \quad (1.6)$$

with improvements having been made recently. Again the error on these contributions is small compared to the that on the hadronic contributions discussed next.

### 1.2.3 Hadronic

The hadronic contributions to  $a_\mu$  arise from loop diagrams with virtual hadrons. Because QCD couplings are large at low energies, the amplitudes for these processes cannot be calculated perturbatively and their errors dominate the theoretical uncertainty in the SM calculation. This makes their error estimation extra important when

comparing to experiment. Most active work on  $a_\mu$  in the theoretical community is in this sector. These contributions can be separated into two parts:

$$a_\mu^{\text{Had}} = a_\mu^{\text{HVP}} + a_\mu^{\text{HLbL}} \quad (1.7)$$

### Hadronic Vacuum Polarization

The first term in Equation 1.7 refers to contributions from hadronic vacuum polarization (HVP), the first order diagram of which is shown in Figure 1.3a. There are two main prescriptions for calculating these contributions. The first is to use a dispersive approach to introduce a virtual hadron bubble into the integral calculation for the photon propagator<sup>2</sup>, and then utilize the optical theorem to relate the imaginary part of that propagator to the total cross-section of electron-positron annihilation to hadrons [12]. While this could be solved perturbatively for a lepton bubble in place of the hadron bubble, this is instead a data driven approach when considering non-perturbative QCD. The leading order contribution can be written as

$$a_\mu^{\text{HVP;LO}} = \left( \frac{\alpha m_\mu}{3\pi} \right)^2 \int_{m_\pi^2}^{\infty} \frac{ds}{s^2} K(s) R(s) \quad (1.8)$$

where  $K(s)$  is some calculable kinematic factor, and  $R(s)$  is a ratio of cross-sections

$$R(s) = \frac{\sigma(e^+e^- \rightarrow \text{hadrons})}{\sigma(e^+e^- \rightarrow \mu^+\mu^-)}. \quad (1.9)$$

The cross-section data for this relation has been measured in different energy ranges by various experiments, including KLOE, CLEO, BaBar, and BESIII [13, 14, 15, 16].

---

<sup>2</sup>The details of dispersion theory will not be described here but a pedagogical introduction is given in Reference [11].



(a) The first order HVP diagram. The bubble H in the middle indicates any combination of hadrons which satisfy the Feynman rules.

(b) The Feynman diagram for electron positron annihilation to hadrons.

Figure 1.3: The first order HVP diagram on the left, which can be related to the diagram on the right by making a ‘cut’ across the virtual hadrons bubble. B is an external magnetic field. Feynman diagrams made with References [5, 6].

The analysis by Keshavarzi et al. [17] gives results as

$$\begin{aligned} a_\mu^{\text{HVP;LO}} &= (693.26 \pm 2.46) \times 10^{-10}, \\ a_\mu^{\text{HVP;NLO}} &= (-9.82 \pm 0.04) \times 10^{-10}, \end{aligned} \quad (1.10)$$

where  $a_\mu^{\text{HVP;NLO}}$  is the next-to-leading order calculation. This evaluation is consistent with Davier et al. [18].

The second prescription for estimating the HVP contributions is a first principles approach, using lattice QCD and QED. Lattice QFT is a gauge theory defined on a matrix of points in time and space. In the limit that the matrix is taken infinitely large with the spacing between the points infinitely small, the behavior from a continuous theory is recovered. The lattice-based estimates of  $a_\mu^{\text{HVP;LO}}$  are consistent with those provided above, though the error is larger [19]. If the calculation is supplemented with the cross-section data described above, then this method provides the most precise determination of  $a_\mu^{\text{HVP;LO}}$  as shown in Figure 1.4.



Figure 1.4: HVP calculations for  $a_\mu$  from various groups. The green points are lattice calculations, the purple points are dispersive results, and the orange point is a combination approach [19].

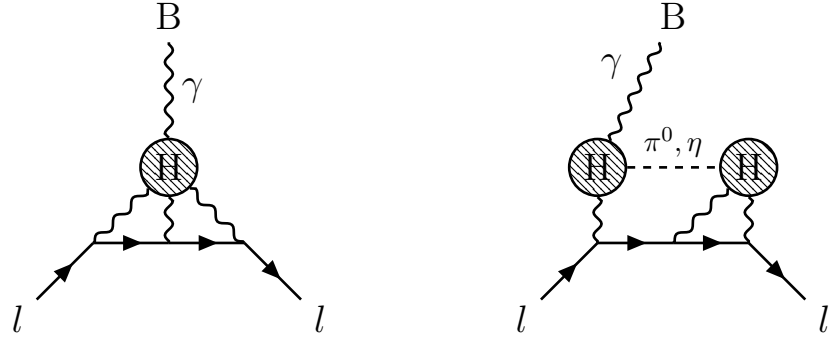
### Hadronic Light-by-Light

The second of these hadronic contribution parts is a higher-order four-photon interaction, termed hadronic light-by-light (HLbL). Diagrams are shown in Figure 1.5. Again perturbation theory is unable to assist in the calculation of these contributions. The calculation of these diagrams has historically been model dependent, and has therefore been the most contentious part of the SM calculation. In more recent years, there have been efforts to produce results using dispersive [20, 21, 22] and lattice approaches [23, 24, 25]. A cumulative report on recent progress is given by N. Asmussen et al. [26]. The error on this contribution is large in each of these various approaches<sup>3</sup>, comparable to that of the  $a_\mu^{\text{HVP;LO}}$  term, even though the size of this contribution is small. The value of the HLbL contributions to  $a_\mu$  given by Nyffeler [27] comes from model estimates and is

$$a_\mu^{\text{HLbL}} = (9.8 \pm 2.6) \times 10^{-10}. \quad (1.11)$$

---

<sup>3</sup>A range of credible models produces a range of results.



(a) The first HLbL diagram, where three photons are exchanged with some virtual hadrons bubble.

(b) A second HLbL diagram, where three photons are exchanged with two virtual hadrons bubbles, that are connected with some virtual charge-less propagator.

Figure 1.5: HLbL diagrams contributing to  $a_\mu$ . B is an external magnetic field. Feynman diagrams made with References [5, 6].

#### 1.2.4 Combined Standard Model value

The sum of the  $a_\mu$  contributions listed here is [7, 8, 9, 10, 17, 27]

$$\begin{aligned} a_\mu^{\text{SM}} &= a_\mu^{\text{QED}} + a_\mu^{\text{EW}} + a_\mu^{\text{Had}}, \\ &= (11659180.26 \pm 3.58) \times 10^{-10}. \end{aligned} \quad (1.12)$$

The relative uncertainty of this result is 307 parts per billion (ppb). Other analyses with different values for the various contributions typically agree well, as shown on the left side of Figure 1.6. In general the consistency of the theory has been stable for almost ten years now. Depending on which calculations are used, the discrepancy between theory and experiment ranges between 3 to 4 standard deviations. The latest experimental result is described in the following section.

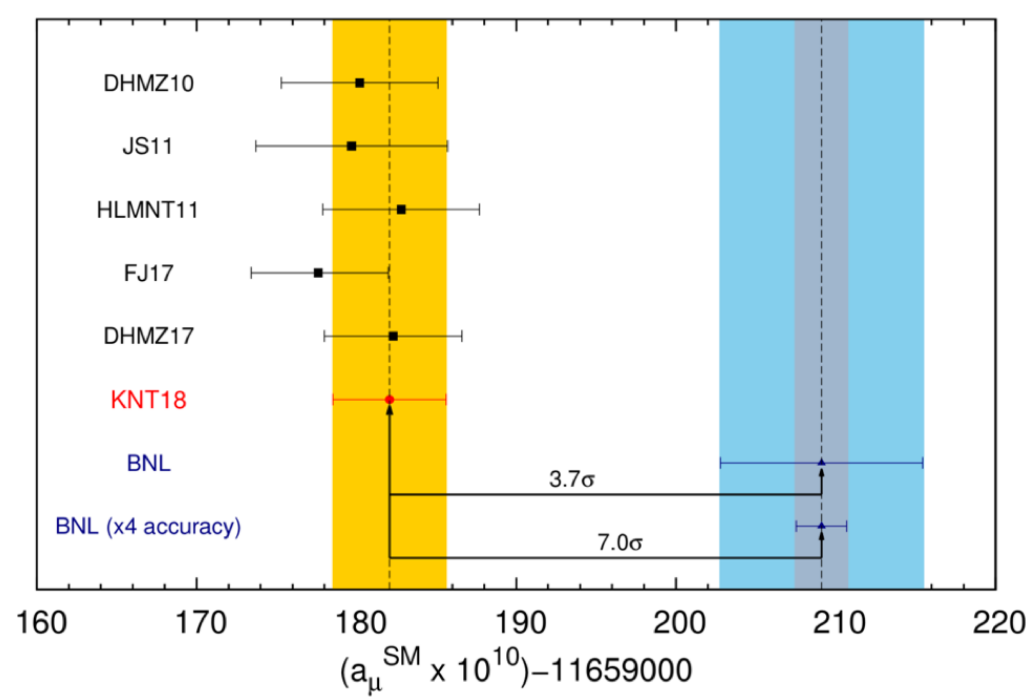


Figure 1.6: Various theoretical values for  $a_\mu$  on the left, as compared to the most recent and extrapolated experimental result on the right [17].

### 1.3 Experimental value of $a_\mu$ and discrepancy with $a_\mu^{\text{SM}}$

The theoretical contributions to  $a_\mu$  listed in the previous sections have improved over time as methods have matured and more experimental data has been gathered. Similarly, work on the direct experimental measurement of  $a_\mu$  has been going on for decades, with more precise results being determined over time [28]. The most recent experiment to measure  $g - 2$  was the Brookhaven Muon  $g - 2$  Experiment (E821) held at Brookhaven National Laboratory (BNL), which collected data from 1997 to 2001. That experiment measured a value for  $a_\mu$  of [29, 30]

$$a_\mu^{\text{Exp}} = (11659208.9 \pm 6.3) \times 10^{-10}, \quad (1.13)$$

which corresponds to a 540 ppb relative uncertainty. Note that the uncertainty of the experimental measurement is comparable to that of the theory, necessitating a precise understanding of all the different theoretical parts. The difference between the experimental and theoretical values presented here is

$$a_\mu^{\text{Exp}} - a_\mu^{\text{SM}} = (28.64 \pm 7.25) \times 10^{-10}, \quad (1.14)$$

corresponding to a discrepancy of nearly four standard deviations from zero.

### 1.4 Beyond the Standard Model and the purpose of E989

While the discrepancy between experiment and theory might be attributed to miscalculations in the theory or systematic errors in the E821 experiment, no such errors have been found despite repeated attempts to resolve the two. Indeed the discrepancy has only grown over time as the theoretical calculations have matured. The most intriguing and exciting source of the discrepancy would be physics beyond the standard model (BSM), Figure 1.7. Since the value of  $a_\mu$  receives contributions from

all particles that couple to the muon through virtual loops, unknown particles might be the source of this discrepancy. Specifically, since the contribution to the magnetic moment from heavy virtual particles goes as

$$a \sim \frac{m^2}{\Lambda^2}, \quad (1.15)$$

where  $\Lambda$  is the mass scale of the new physics and  $m$  the mass of the lepton in question, the sensitivity of the muon as compared to the electron to large mass scales is  $m_\mu^2/m_e^2 \approx 43,000$  times greater. For this reason, it is possible that even though the g-factor of the electron has been measured extraordinarily precisely, to .26 parts per trillion (ppt) corresponding to a .23 ppb relative uncertainty in  $a_e$  [31, 30], it has not yielded a definitive difference between theory and experiment, whereas the magnetic moment of the muon might do so<sup>4</sup>.

Because the discrepancy from the previous experiment was not at the five standard deviation level necessary to classify it as a discovery, the E989 experiment was undertaken. Indeed with the lack of new physics results coming out of most other experiments, E989 is especially positioned to uncover something new at a time when there are so few hints of new physics. Because of this, the interest in the E821 experiment and its successor E989 has grown over time. The number of citations for the E821 results has been consistently high for 20 years as shown in Figure 1.8.

The E989 experiment has the goal of measuring  $a_\mu$  to 140 ppb over the course of several years. This would be a factor of four improvement over the E821 result stemming from a twenty times increase in statistics, which was dominate error in the previous experiment. Assuming the same central value for  $a_\mu$  is obtained, this would push the statistical significance of the discrepancy over to approximately seven

---

<sup>4</sup>A recent measurement of the fine structure constant  $\alpha$  to the highest precision yet [32] has yielded a new value of  $a_e$  for which the difference between theory and experiment is 2.5 standard deviations, but with the opposite sign as compared to  $a_\mu$ .



Figure 1.7: A general Feynman diagram, where the leptons couple to an external magnetic field  $B$  through some BSM physics. Feynman diagrams made with References [5, 6].



Figure 1.8: The number of citations for the BNL experiment publications as a function of year [33]. **Update this plot before submission - also should maybe be citing Mark here instead of Lee.**

standard deviations, as shown in Figure 1·6. The data comprising Run 1, gathered between April and July of 2018, is the subject of this thesis, and corresponds to a statistical uncertainty comparable to the E821 result. The possibility is that we will measure something new and exciting, either in Run 1 or the following runs. However, even if we do not, it is valuable in itself to resolve this theoretical and experimental conflict.

## Chapter 2

# Principal Techniques of E989

A particle with non-zero spin in a magnetic field will experience a torque which attempts to line up the magnetic dipole moment of the particle with the external field. Because of this, in a dipole field a particle's spin will turn at the spin precession frequency [34]

$$\vec{\omega}_s = -g \frac{q}{2m} \vec{B} - (1 - \gamma) \frac{q}{\gamma m} \vec{B}, \quad (2.1)$$

where  $m$  is the particle's mass,  $q = \pm e$  where  $e$  is the positive elementary charge,  $g$  is the g-factor,  $\gamma$  is the Lorentz relativistic factor, and  $B$  is an external magnetic field. The first term is the usual Larmor frequency and the second term is a relativistic correction to the precession frequency in an accelerating frame called Thomas precession. Similarly, a particle with some momentum perpendicular to the magnetic field will orbit at the cyclotron frequency

$$\vec{\omega}_c = -\frac{q}{\gamma m} \vec{B}. \quad (2.2)$$

By taking the difference between these two frequencies we arrive at the “spin difference frequency”

$$\vec{\omega}_a = \vec{\omega}_s - \vec{\omega}_c = -\frac{g-2}{2} \frac{q}{m} \vec{B} = -a \frac{q}{m} \vec{B}, \quad (2.3)$$

a frequency that is directly proportional to the anomaly  $a$ . If  $g = 2$ , as in a Dirac theory, then the particle's spin would turn at the same rate as the momentum vector, and  $\omega_a$  would be identically zero. If  $\omega_a$  for a muon and the external magnetic dipole field can be measured, then the anomalous magnetic moment of the muon  $a_\mu$  can be determined.

As will be detailed in Section 2.2, the measurement of the magnetic field is related to the Larmor precession frequency of free protons in water

$$\omega_p = -g_p \frac{e}{2m_p} B, \quad (2.4)$$

where  $g_p$  and  $m_p$  are the g-factor and mass of the proton respectively. Replacing  $B$  and solving for  $a_\mu$ , we arrive at

$$a_\mu = \frac{g_p}{2} \frac{\omega_a}{\omega_p} \frac{m_\mu}{m_p}. \quad (2.5)$$

Using the magnetic moment formulae for the proton, electron, and muon as shown in Equation 1.1, Equation 2.5 can be transformed into

$$a_\mu = \frac{g_e}{2} \frac{\omega_a}{\omega_p} \frac{m_\mu}{m_e} \frac{\mu_p}{\mu_e}, \quad (2.6)$$

where the  $p$ ,  $e$ , and  $\mu$  subscripts stand for the relevant quantities for the proton, electron, and muon respectively. The experimental error on  $a_\mu$  then becomes the quadrature sum of each individual quantity error. As mentioned in Section 1.4 the electron g-factor  $g_e$  has been measured to extremely high precision, 0.26 ppt [30, 31]. The muon-electron mass ratio,  $m_\mu/m_e$ , has been measured to 22 ppb [30, 35]. Finally the proton-electron magnetic moment ratio,  $\mu_p/\mu_e$ , has been measured to 3 ppb [30]. These are small compared to the target statistical error on  $\omega_a$  of 100 ppb, and target systematic errors on  $\omega_a$  and  $\omega_p$ , both at 70 ppb<sup>1</sup>. These errors added in quadrature

---

<sup>1</sup>The measurement of  $\omega_p$  has negligible statistical error.

is approximately 140 ppb, which is the target of the E989 experiment.

## 2.1 Measuring $\omega_a$

How can  $\omega_a$  for muons be measured? The answer lies with two key points in the dynamics of muon decay. Positive muons decay to a positron and two neutrinos, as shown in Figure 2·1. The first point is that because of the parity violating nature of the weak interaction, the decay positron will be preferentially emitted right-handed, with its spin directed in the same direction as its momentum [36]. The second key point is that angular momentum must be conserved. Consider the most extreme examples of maximum and minimum energy positrons as shown in Figure 2·2. In the muon rest frame, decay positrons with maximum energy will be emitted opposite to the two neutrinos, both emitted in the same direction. Since neutrinos and anti-neutrinos must be left and right-handed respectively, thus having their spins anti-parallel and parallel to their momentum, by the law of conservation of angular momentum the positron must have its spin be parallel to the spin of the muon at the time of the decay. By the opposite argument, decay positrons emitted with minimum energy such that the neutrinos are ejected opposite to one another must have their spins be anti-parallel to that of the muon at the time of decay. Together, these two points mean that higher energy decay positrons will preferentially be emitted in directions parallel to the muon spin at the time of decay, while lower energy decay positrons will preferentially be emitted in directions anti-parallel to the muon spin at the time of the decay.

This correlation between the direction of an emitted high energy decay positron and the spin of the muon is the signature needed to measure  $\omega_a$ . Muons placed within a magnetic storage ring will orbit at the cyclotron frequency and their spins will precess at the spin precession frequency. As they go around the ring they will



Figure 2·1: Feynman diagram for muon decay.  $\mu^+$  decay through a  $W^+$  boson to a positron, muon anti-neutrino, and an electron neutrino. This process consists of nearly 100% of the muon decay branching ratio, with other decay states including radiative processes.



Figure 2·2: Muon decay in the rest frame for maximum (top) and minimum (bottom) energy decay positrons. Due to the conservation of angular momentum and the single possible helicity states of the decay neutrinos, the spin of the decay positron is exactly parallel to the spin of the muon at the time of the decay for maximum energy decay positrons, or anti-parallel for minimum energy decay positrons.

decay to positrons whose energy and decay directions contain information about the spin of the muon. If the muon ensemble is un-polarized, then the decay distribution for all positrons will be isotropic and in general un-useful. If the muon ensemble is polarized, then the decay distribution for each muon will be the same, and allow for a measurement of  $\omega_a$ , as described in the following text.

The differential decay distribution for positive muons in the muon rest frame is described by [36]

$$dP(y, \theta) \propto N(y)[1 + A(y)\cos(\theta)]dyd\Omega, \quad (2.7)$$

where  $y = E/E_{max}$  is the energy fraction of the positron and  $\theta$  is the angle between the spin of the muon and the momentum of the positron at the time of decay.  $N(y)$  is the number distribution of decay positrons and  $A(y)$  is the so called ‘asymmetry,’ encoding the energy-dependent correlation between the muon spin and the decay positron direction. Here the energy of the positron is assumed to be much greater than its mass. The number distribution and asymmetry are given by [36]

$$N(y) = 2y^2(3 - 2y), \quad (2.8)$$

$$A(y) = \frac{2y - 1}{3 - 2y}, \quad (2.9)$$

and are shown in Figure 2·3a.

In the lab frame, nearly all high energy positrons are emitted parallel to the muon momentum, making it challenging to select purely on the decay angle of the positron. That is not a problem however, as we already know that decay positrons with the highest rest-frame energies will be emitted parallel to the muon spin at the time of decay. Essentially, the energy distribution of detected high energy positrons is modulated by  $\omega_a$ , or  $\theta = \omega_a t + \phi$ . The number of detected positrons at some time and energy in the lab frame for some initial number  $N_0$  of muons can then be described



Figure 2.3: Decay number distribution  $N$  and asymmetry  $A$  in the muon rest frame (left) and in the lab frame (right) as a function of positron energy with a maximum positron energy of 3.1 GeV.  $N$  is multiplied by arbitrary factors in both pictures.

by

$$N_d(t, E) = N_0(E) \cdot e^{-t/\gamma\tau_\mu} \cdot [1 + A(E) \cos(\omega_a t + \phi(E))], \quad (2.10)$$

where the  $d$  subscript stands for ‘detected,’ the muons are decaying with a lifetime of  $\gamma\tau_\mu$ , and all the relevant parameters are energy dependent. Here  $N_0(E)$  and  $A(E)$  have been transformed from Equations 2.8 and 2.9 to the lab frame:

$$N_0(E) \propto (y - 1)(4y^2 - 5y - 5), \quad (2.11)$$

$$A(E) = \frac{-8y^2 + y + 1}{4y^2 - 5y - 5}, \quad (2.12)$$

where as a reminder  $y = E/E_{max}$ . Here the polarization of the muons is assumed to be unity. These relations are shown in Figure 2.3b. All positrons above some energy threshold cut  $E_{th}$  can be taken as the observable,

$$N_d(t, E_{th}) = N_0(E_{th}) \cdot e^{-t/\gamma\tau_\mu} \cdot [1 + A(E_{th}) \cos(\omega_a t + \phi(E_{th}))], \quad (2.13)$$

where the number and asymmetry of the detected positrons is now calculated by



Figure 2.4: The number of detected positrons above some energy threshold ( $y \sim 0.55$ ) as a function of time, where the data plotted come from Run 1 and correspond to nearly  $1 \times 10^9$  counts. The time axis is wrapped around every  $100\text{ }\mu\text{s}$ . See Chapter 5 for the fitting of such a histogram.

simply integrating Equations 2.11 and 2.12 from  $y_{th}$  to 1,

$$N_0(E_{th}) \propto (y_{th} - 1)^2(-y_{th}^2 + y_{th} + 3), \quad (2.14)$$

$$A(E_{th}) = \frac{y_{th}(2y_{th} + 1)}{-y_{th}^2 + y_{th} + 3}, \quad (2.15)$$

where  $y_{th} = E_{th}/E_{max}$ . By counting decay positrons above some energy threshold and fitting the resulting time spectrum with Equation 2.13,  $\omega_a$  can be extracted. A sample of data adhering to such a time spectrum is shown in Figure 2.4.

The statistical error on the  $\omega_a$  measurement, assuming bin errors are Gaussian and a  $\chi^2$  minimization is used with the fit function described in Equation 2.13, is [37]

$$\frac{\sigma_{\omega_a}}{\omega_a} = \frac{\sqrt{2}}{\sqrt{N_{\text{total}}} A \gamma \tau_\mu \omega_a}, \quad (2.16)$$

where  $N_{\text{total}}$  is the total number of counts included in the above-threshold time spectrum. This equation assumes a weighting of one for every count included in the fitted time spectrum. Other weighting schemes exist which slightly improve the statistical precision of the  $\omega_a$  measurement [37], but they are not used in this analysis. What Equation 2.16 reveals is that the statistical precision of  $\omega_a$  is maximized when the quantity  $NA^2$  is at a maximum. It was found for E989 that the optimal energy threshold was about 1.7 GeV as shown in Figure 5·5, which includes detector acceptance effects and corresponds to an asymmetry of about  $A = 0.37$ . Equation 2.16 can be rearranged in order to solve for the number of positrons needed to be collected above threshold for a specific precision goal. For a statistical error of 100 ppb on  $\omega_a$ , the required number of positrons above threshold is approximately  $170 \times 10^9$ , determined from the values  $A = 0.37$ ,  $\gamma = 29.3$  (described later),  $\tau_\mu = 2.2 \mu\text{s}$ , and  $\omega_a = 1.44 \text{ rad}/\mu\text{s}$ . This statistical error of  $\omega_a$  combined with the systematic uncertainties given in Table 5.8, provide the total error on  $\omega_a$ .

## 2.2 Measuring the magnetic field

In order to measure the magnetic moment of the muon to 140 ppb, the field needs to be both highly uniform, and measured to extreme precision. The E989 goal for the field measurement is 70 ppb. As shown in Equation 2.6, the measurement of the magnetic field has equal weight to that of the precession frequency. A cross-section of the magnetic storage ring used in E989 is shown in Figure 2·5. It is an approximately 14 m diameter C magnet, where the muons are stored within a 4.5 cm radius cylindrical storage region at the center of a 1.451 T magnetic field. This corresponds to an approximately  $0.28 \text{ m}^3$  or  $10 \text{ ft}^3$  total volume around the inside of the ring. The magnetic field is made uniform by manipulating many magnetic ‘knobs’ built into the  $g - 2$  storage ring, including the main magnet current, pole



Figure 2·5: Cross-section of the  $g - 2$  magnet. The muons live in the 4.5 cm radius circular storage region shown in red. The main magnetic field is excited by superconducting coils shown in yellow. Pole pieces, wedges, edge shims, top hats, and other magnetic knobs allow for sub-ppm level tuning of the magnetic field.

pieces, wedges, top hats, and thousands of small magnetic shims placed around the storage region, as shown in Figure 2·5. There is also an active feedback system which stabilizes the average magnetic field over time using current carrying coils near the storage region. After a several month shimming campaign by many members of the field team, a precision on the magnetic field of approximately 25 ppm RMS (root mean square) was achieved.

The magnetic field is measured using a nuclear magnetic resonance (NMR) technique, hence the measurement on  $\omega_p$  as shown in Equation 2.4. NMR was chosen as it provides a field measurement precision on the order of 10 ppb with negligible statistical uncertainty [38]. NMR probes consist of pickup coils located around a sample of protons in some fluid, typically water or petroleum jelly. The pickup coils



Figure 2·6: An example FID signal. The current picked up in the coils around the proton sample will oscillate as the spins precess around the main magnetic field, and decay as the spins return to alignment with the external field.

deliver a “ $\pi/2$  pulse” which rotates the proton sample magnetization  $90^\circ$  out of phase from equilibrium. The proton spins will begin precessing at the Larmor frequency ( $\approx 61.79$  MHz). As the spins interact with local magnetic field gradients and inhomogeneities, the magnetization of the proton sample will relax back to equilibrium with the external field, typically on the order of several milliseconds. This so-called free-induction decay signal (FID), an example of which is shown in Figure 2·6, is measured using the same pickup coils that delivered the initial  $\pi/2$  pulse

It is not solely  $\omega_p$  that needs to be measured. What really matters is the average magnetic field that the muons see, namely the time-averaged spatially-weighted magnetic field. The scheme devised to measure this is two-fold. First, the magnetic field in the muon storage region is measured by a trolley which travels around the inside of the ring. This trolley holds 17 NMR probes which measure the field at approximately 6000 locations around the inside of the ring. However, because the trolley cannot be in the storage region when the muons are present in the ring, during data taking it



Figure 2·7: A sample of the azimuthally-averaged magnetic field within the storage region [39]. The contours are normalized to the field value at the center of the storage region. The scale of the field differences is approximately  $\pm 1.5$  ppm. The black dots in the picture correspond to the location of the trolley probes.

is retracted and the field is instead monitored by 378 fixed NMR probes located in the high magnetic field region, just outside the storage region on the outside of the vacuum chambers. The prescription is that the storage ring field is measured every few days by the trolley probes, and the field between trolley runs is interpolated using measurements from the continually-sampling fixed probes. In this way the magnetic field can be mapped over time and over the space in which the muons are stored. A sample of the azimuthally-averaged magnetic field measured with trolley and fixed probes is shown in Figure 2·7.

Lastly, it is the free proton precession frequency in the field that is of interest, but the frequency that the trolley probes measure will be different due to the molecular

properties of the proton sample as well as the material properties of the probe itself. The frequency of the induction signal that the probes measure can be re-cast as

$$\omega_{p,\text{probe}} = \omega_{p,\text{free}}(1 - \sigma(\text{H}_2\text{O}, T) + \delta_b + \delta_p + \delta_s), \quad (2.17)$$

where  $\sigma(\text{H}_2\text{O}, T)$  is the temperature-dependent diamagnetic shielding of protons in a water molecule, and the  $\delta$ 's come from corrections due to the bulk susceptibility of the water sample, paramagnetic impurities in the water sample, and the magnetic effects of the probe itself, respectively [38]. In order to correct for these effects two additional special probes are used, both of which live in a single section of the ring which has been shimmed to extra uniformity. The first is a calibration probe which measures the free proton precession frequency at the center of the storage region, corresponding to the position of the central trolley probe. The calibration probe is made of materials which are designed to reduce the effects listed in Equation 2.17, and has been characterized in a dedicated highly uniform solenoidal magnetic field. The second special probe is called the ‘plunging probe.’ This probe is located inside the vacuum chamber and moves into the storage region to measure the field at each of the 17 trolley probe locations, using a three dimensional motion system. By using these two probes, the calibration to the free proton precession frequency can be transmitted to each of the trolley probes, providing an absolute scale for the measurements inside the muon storage region. The uncertainty on the calibration procedure is estimated to be 35 ppb, about half the total permitted by the experimental error budget of 70 ppb.

Other pieces of the systematic uncertainty include the calibrations of the probes, errors in the trolley measurements, the interpolation with the fixed probes, the uncertainty of the magnetic field relative to the muon distribution, and others such as time dependent external magnetic fields, Table 2.1.

<b>Magnetic Field Measurement Uncertainties</b>	
Source of uncertainty	E989 Goal (ppb)
Absolute calibration of standard probe	35
Calibration of trolley probes	30
Trolley measurements	30
Fixed probe interpolation	30
Muon distribution weighted average	10
Time dependent external fields	5
Others	30
Quadrature sum	70

Table 2.1: Systematic errors in the magnetic field measurement. Unlisted sources of error include the measurement of higher field multipoles, trolley temperature and power supply voltage response effects, and eddy currents from the kicker, among others.

### 2.3 Production of polarized muons

As explained in Section 2.1, in order to measure  $\omega_a$  the muons injected into the storage ring must be polarized. The BNL E821 experiment observed on the order of 10 billion positrons above threshold, and its final result was statistics limited. In order to reach the goal of 140 ppb, approximately 20 times that number of positrons needs to be gathered, and hence a large number of polarized muons produced. Fermilab has the facilities to produce such a large number of polarized muons.

Polarized muon beams are constructed using the physics of pion decay. Using the same parity-violation and spin momentum conservation logic as explained in the discussion of muon decay, it is determined that pion decay produces muons that are 100% polarized in the pion rest frame, due to the pion having zero spin. It is also important to note that pions decay to muons with a  $\sim 99.98\%$  branching ratio due to the parity violating nature of the weak interaction [40]. Thus by producing a large number of polarized pions a large number of polarized muons can be acquired.



Figure 2.8: The layout of accelerator beam-line components Fermilab uses to provide polarized muons to E989. Protons start in the Linac, traverse around the Booster and then Recycler, and are converted to pions at AP0. The pions are gathered and then decay to muons in the Delivery Ring before being sent to the  $g - 2$  storage ring. [38].



Figure 2.9: General timing structure of beam pulses sent to E989.

The production of polarized muons for E989 at the Fermilab accelerator complex involves a number of stages. A map of the various relevant accelerator beam-line components is shown in Figure 2.8. Details of the full accelerator production of polarized muons can be found in Reference [41], and here a summary of the process will be given. First,  $H^-$  ions are produced and accelerated in a linear accelerator. They are stripped down to protons and then transported to a 75 m radius circular storage ring called the “booster,” which accelerates them up to 8 GeV/c and batches them together. A single booster batch contains on the order of  $4 \times 10^{12}$  protons. The protons are then injected into a ring called “recycler,” which separates them into four separate bunches of  $1 \times 10^{12}$  protons, each with a time width of approximately 120 ns. (This is less than the cyclotron period of the storage ring of 149 ns.) This re-bunching process is done in order to reduce the instantaneous rates observed by the detectors, and thus reduce the level of pileup in the E989 detectors; see Section 3.2.1. For a single accelerator supercycle of 1.4 s, E989 receives four booster batches corresponding to sixteen recycler bunches at an average rate of 11.4 Hz, with the time separation between bunches greater than 10 ms. The timing structure is shown in Figure 2.9, where trains of eight bunches are sent to E989 with some time separation between them<sup>2</sup>. Although it remains relatively constant, this timing structure may be modified in response to the requirements of other experiments.

---

<sup>2</sup>These eight bunches are sometimes referred to as pulses, and the gathered data is tagged by which bunch or pulse it originates from.

Each bunch is sent to a target hall, where it is directed on to an Inconel target. This Inconel target is made of a nickel-iron alloy, and is optimized for the production of a large number of pions with a small momentum spread, approximately  $1 \times 10^{-5} \pi^+$  per proton on target with  $|dp/p| < 2\%$  [41]. The pions are focused by the magnetic field of a lithium lens, located just downstream of the production target. The lens, a cylinder of lithium 1 cm in radius and 15 cm long, carries a large current down its length which provides a radial focusing effect for particles passing down the cylinder [42]. A pulsed magnet just after the lithium lens is then used to select pions and residual particles, mainly protons, centered at 3.115 GeV.

The resultant pion beam and these residual particles are then injected into another ring called the “delivery ring”<sup>3</sup>. Here it should be noted that in a pion beam the highest and lowest energy decay muons are forwards and backwards polarized, respectively. The delivery ring is used to momentum select polarized muons and separate out the non-desired particles which will have differing velocities compared to the muons, reducing the contamination in the final polarized muon beam [41]. Forward emitted polarized muons are momentum selected at their decay energies of 3.094 GeV with  $\Delta p/p = 2\%$ . Particles that fall outside the momentum acceptance are lost, and the residual protons are kicked into a beam dump. The polarized muon beam is then sent to the E989 building where it passes through four magnetic quadrupole focusing magnets before being injected into the E989 storage ring.

## 2.4 Injection of muons

The injection of the muon beam into the E989 storage ring is a specialized process. In order to measure the magnetic field to the precision described in Section 2.2, the storage ring must be a single monolithic magnet with no end effects. This prohibits

---

<sup>3</sup>By the time the pions have gotten to the delivery ring, most of them have decayed to muons.

the usual design of separated magnetic elements through which the muons might be injected. Therefore the beam must be injected through the storage ring magnet yoke. This introduces the design constraint where the main magnet field must be eliminated within the injection tunnel, such that muons are not lost due to deflection into the magnet itself. Any solution to this problem must have it's cancellation field localized to the injection tunnel, such that there is no residual fringe field that contaminates the main storage ring dipole field.

A specialized magnet called the “Superconducting Inflector” magnet, or just inflector, is used to solve these design constraints. This inflector is placed just after a bored out tunnel in the storage ring magnet yoke, on the inside of the C shape. See Figure 2·10 for a view of the injection point. The inflector has an 18 mm wide by 56 mm high aperture through which the muons must pass down its 1.7 m length. The inflector is made up of superconducting coils wrapped in a truncated double cosine theta design around an aluminum mandrel [43]. See Figure 2·11. This design serves to contain the majority of the inflector magnet field, while eliminating the the storage ring field for the muons passing down its length. The inflector is contained within a superconducting shield which traps the fringe field of the inflector such that the storage ring magnet field is unaffected. As shown in Figure 2·11, windings cover both ends of the inflector such that an appreciable fraction of muons are lost due before being injected into the ring. In order to increase the muon flux for future runs of E989, a new inflector magnet is being designed with open ends [38].

## 2.5 Storage of muons

Once the muons have been injected into the ring, they will begin orbiting clockwise around the ring, decaying with a lifetime of 64.4  $\mu\text{s}$ . The E989 experiment and storage ring are shown in Figure 2·12. By necessity, the inflector must be out of the stored



Figure 2.10: A plan view of the inflector and injection point into the storage ring [43].

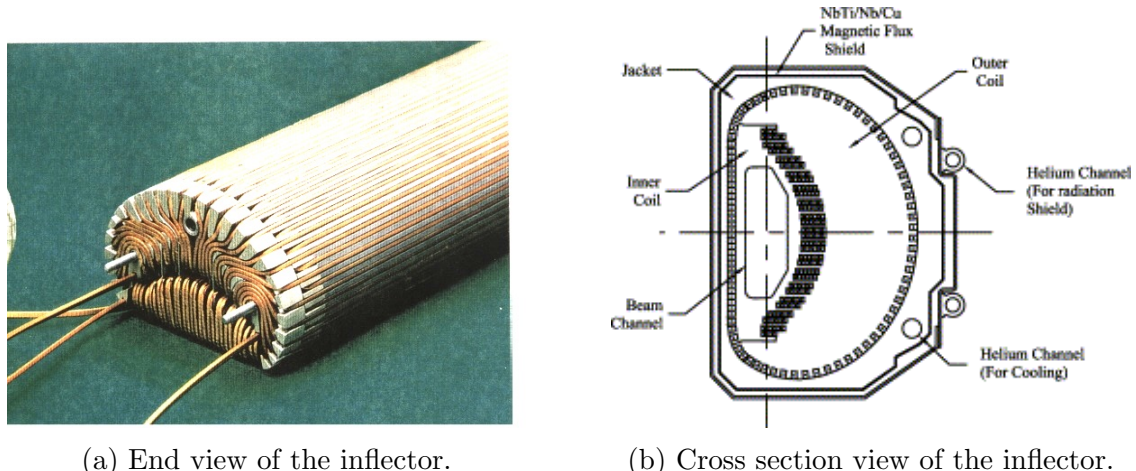


Figure 2.11: The inflector magnet (left) and a cross section view of the inflector windings and associated shield (right) [43].

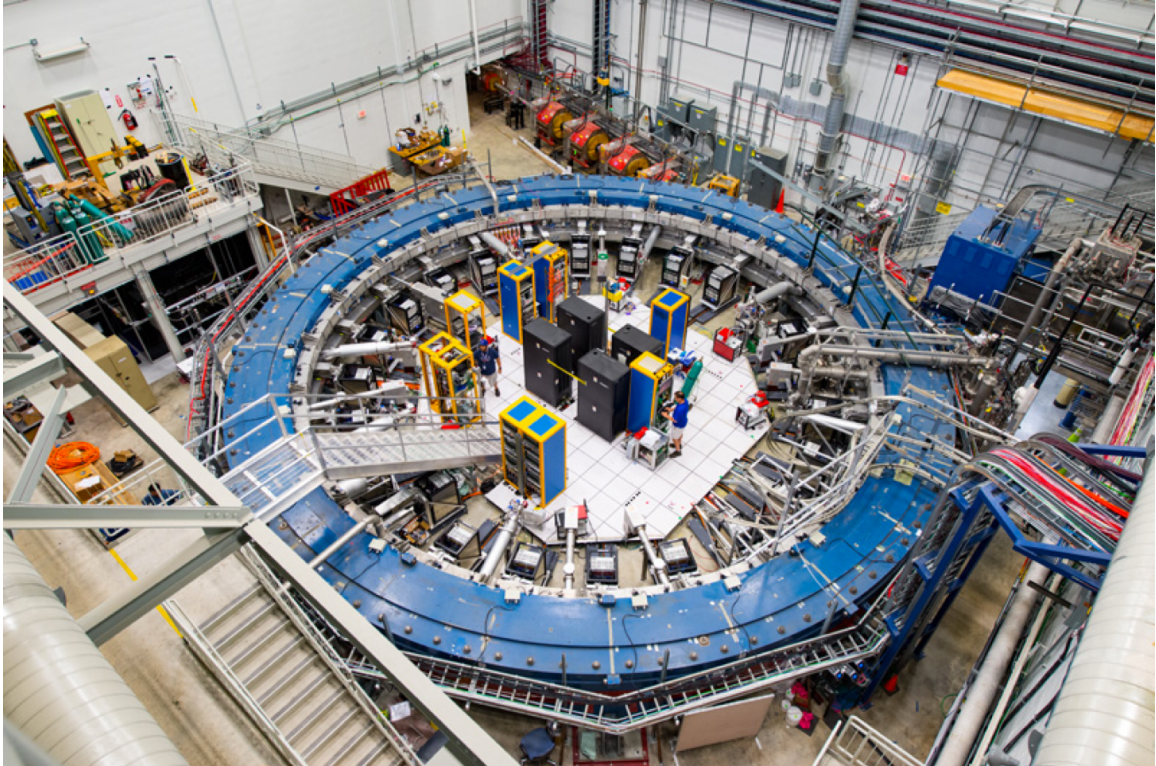


Figure 2.12: The E989 experiment. The blue storage ring can be seen to surround a variety of detectors and electronics. Muons from the accelerator enter at the top of the picture, and are transported to the storage ring through a series of magnetic quadrupoles. Muons are injected through the inflector into the ring, where they orbit in a clockwise direction. The ring is approximately 16 m in diameter to the outside edge of the ring, and about 3 m high. People in the center of the ring give a sense of scale to the picture.

muon beam path, otherwise a large fraction of the muons would be lost upon the return to the injection point as the muons would strike the inflector. Therefore the muon beam must be kicked to move the beam path from the injection orbit onto the central orbit of the storage ring. The muon beam must also be contained vertically. To perform the former, a magnetic “kicker” is used to shift the orbits of the muons. To perform the latter, a series of electrostatic quadrupoles focus the beam vertically. Approximately 2% of the injected muons are stored with  $\Delta p/p = 0.1\%$  centered around 3.094 GeV/c, corresponding to a design goal of  $\mathcal{O}(10,000)$  stored muons per fill.

### 2.5.1 Kicker

The kicker is made up of three separate pulsed magnets located 90° from the exit of the inflector, where the injection orbit crosses the central orbit. The placement of the kickers is shown in Figure 2.13. The kicker must be located within the precision magnetic field of the ring, and must therefore contain no magnetic elements in the hardware itself. For this reason each kicker magnet is made up of two thin 1.27 m long aluminum plates, separated by 10 cm, which carry the current used to create the kicking magnetic field. Due to the bunched nature of the muon beam and the short cyclotron period of 149 ns, ideally the kicker moves all injected muons onto the central orbit and then turns off quickly such that by the time the muons orbit back around to the kicker there is no residual kick to the beam. Any residual eddy currents must die away quickly enough such that the magnetic field seen by the stored muons is unperturbed. The design deflection of the beam is approximately 10 mrad using a vertical pulsed field of around 300 Gauss (corresponding to kicker plate voltages of  $\mathcal{O}(155 \text{ kV})$ ) with a pulse length of about 120 ns [38]. The operational kicker performance in Run 1 was less, as described in Section 2.8.

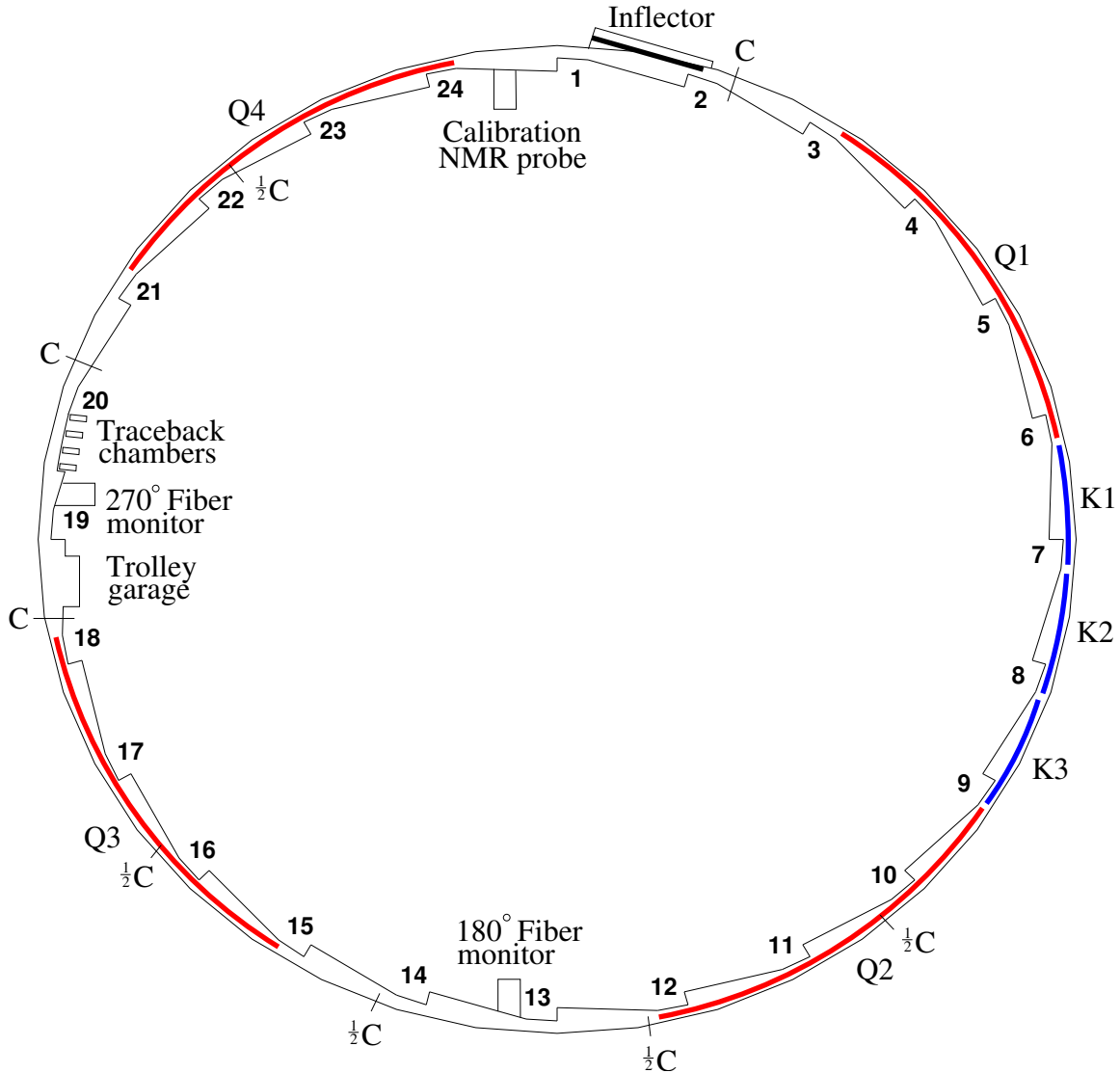


Figure 2·13: A map of the vacuum chambers in E989. K1-K3 show the locations of the kicker magnets, while Q1-Q4 show the locations of the electrostatic quadrupoles. Also shown is the location of the inflector, the two fiber monitors, and one of the tracker stations.

### 2.5.2 Electrostatic quadrupoles

There are four electrostatic quadrupoles located around the ring as shown in Figure 2.13, which provide vertical focusing for the beam. Although the quadrupoles are defocusing in the horizontal plane, the main dipole magnetic field provides net horizontal focusing. Just as with the kickers, the quadrupoles must be operated in vacuum. E989 uses electrostatic focusing elements instead of magnetic ones in order to avoid magnetic field gradients which would limit the precision of the magnetic field measurement. The quadrupoles occupy 43% of the ring circumference, with four quads having been chosen in order to maximize the symmetry of the beam motion, reduce its amplitude, and leave space for other experimental elements around the ring [38]. Each quad is made up of two segments, a short segment of 13° and a long segment of 26° corresponding to 1.61 m and 2.62 m respectively, with each segment consisting of four plates. To minimize multiple scattering of incident decay positrons, the quadrupoles are made as thin as possible. A picture of the quadrupoles installed into one of the vacuum chambers is shown in Figure 2.14. A calculation of the equipotential lines of the quadrupoles is shown in Figure 2.15. The original design of the quadrupoles is detailed in Reference [44].

Some of the stored muons will be lost during data taking that can adversely affect the measurement of the spin difference frequency  $\omega_a$ . See Section 5.3.3. In order to reduce the number of lost muons, a procedure called “scraping” is used to remove those muons sitting at the edge of the storage region that are more likely to be lost at later times. This scraping procedure involves powering the quad voltages in an asymmetric way such that the beam is pushed to the outside of the storage region, where the edges of the beam will intersect copper collimators. These collimators have a radius of 45 mm and define the storage region aperture. Muons which hit the collimators will lose energy and be lost as they spiral out of the ring. The scraping



Figure 2·14: Electrostatic quadrupoles installed into a vacuum chamber [44]. There are four plates mounted to the chamber through insulator standoffs, with the distance between opposing quad plates equal to 10 cm. Also shown are the rails on which the magnetic field trolley rides. Note that as the trolley makes its way through the storage volume, it must pass between both the various sets of quadrupole and kicker electrodes.



Figure 2.15: An OPERA model of the quadrupoles and their equipotential contours [38]. The top and bottom plates sit at positive voltage while the left and right plates are at negative voltage. The muon storage region is shown by the blue circle.

procedure is performed early in the fill and ends at  $8\text{ }\mu\text{s}$ , such that by  $30\text{ }\mu\text{s}$  the beam is stable and centered due to the characteristic RC time constant of the system. The operational performance of the quadrupoles in Run 1 is described in Section 2.8, where it was found that the quads had a longer RC time constant than the design.

## 2.6 Muon beam dynamics

Muons injected into the storage ring will occupy a region in phase space of momenta and positions defined by the injection and collimator apertures. Individual muons will undergo betatron motion within the storage ring in both the vertical and horizontal directions. The horizontal ( $x$ ) and vertical ( $y$ ) equations of motion, including the

effects of the discrete quadrupoles, are given by

$$x = x_e + A_x(s) \cos(\nu_x \frac{s}{R_0} + \phi_x), \quad (2.18)$$

$$y = A_y(s) \cos(\nu_y \frac{s}{R_0} + \phi_y), \quad (2.19)$$

where  $x_e$  is the radial equilibrium orbit of the beam relative to  $R_0$ ,  $A_x(s)$  and  $A_y(s)$  are the amplitudes of the motions containing the effects of the discreteness of the quadrupoles, and  $s$  is the arc length of the trajectory. Here  $\nu_x$  and  $\nu_y$  are the so-called horizontal and vertical “tunes” of the beam motion, which are ratios of the betatron frequencies to the cyclotron frequency  $f_c$ :

$$\begin{aligned} \nu_x &= f_{x_{BO}}/f_c = \sqrt{1-n} \\ \nu_y &= f_{y_{BO}}/f_c = \sqrt{n} \end{aligned} \quad (2.20)$$

These are related to the field index  $n$ , where the field index characterizes the strength of the electrostatic focusing in relation to the magnetic field strength:

$$n = \frac{\kappa R_0}{\beta B_0}, \quad (2.21)$$

where  $\kappa$  is the electric quadrupole gradient,  $B_0$  is the magnetic field strength,  $R_0$  is the central storage ring radius, and  $\beta \cdot c$  is the velocity of the muon beam. Technically  $n$  is the average field index around the ring, where this approximation is justified due to the four-fold symmetry of the discrete quadrupoles and the fact that the betatron oscillations have wavelengths much greater than the length of the quads. A table of the important frequencies in E989 is shown in Table 2.2. Lastly, the maximum angular acceptance of the ring can be determined from the betatron oscillations and

Muon Beam Frequencies				
Name	Symbol	Expression	Frequency (MHz)	Period
$g - 2$	$f_a$	$a_\mu Be/2\pi mc$	0.23	4.365 $\mu$ s
cyclotron	$f_c$	$v/\pi R_0$	6.71	149 ns
horizontal betatron	$f_{x_{BO}}$	$\sqrt{1-n}f_c$	6.34	158 ns
vertical betatron	$f_{y_{BO}}$	$\sqrt{n}f_c$	2.21	452 ns
coherent betatron	$f_{CBO}$	$f_c - f_{x_{BO}}$	0.37	2.703 $\mu$ s
vertical waist	$f_{VW}$	$f_c - 2f_{y_{BO}}$	2.31	433 ns

Table 2.2: Frequencies seen in the  $g - 2$  experiment due to beam motion. Parameter values are from a subset of Run 1 corresponding to an  $n$  value of 0.108 or a quad voltage of 18.3 kV.

the field index as

$$\begin{aligned}\psi_{x_{max}} &= \frac{x_{max}\sqrt{1-n}}{R_0}, \\ \psi_{y_{max}} &= \frac{y_{max}\sqrt{n}}{R_0},\end{aligned}\tag{2.22}$$

where  $x_{max}$  and  $y_{max}$  are both equal to the radius of the storage region aperture at 45 mm.

As the muon beam goes around the ring, the muons will experience local field gradients and inhomogeneities. The muons will inevitably pass through the perturbations many times. However, if they don't pass through the perturbations at the same phases of their betatron motion, the amplitude of the would-be resonant oscillation won't continue to grow. The tunes are chosen to avoid these resonances by having the muons sample the entire azimuth of the ring equally, thus keeping the beam stored. The general resonance condition is [45]

$$a\nu_x + b\nu_y = c,\tag{2.23}$$

where  $a$ ,  $b$ , and  $c$  are integers. We know from Equation 2.20 that

$$\nu_x^2 + \nu_y^2 = 1,\tag{2.24}$$



Figure 2.16: The tune plane, with the  $\nu_x^2 + \nu_y^2 = 1$  constraint in red. The chosen value of  $n$  lies on this circle. The original design goals for E989 were the  $n$  values as shown by the red points, but due to hardware issues smaller  $n$  values of 0.108 and 0.120 were chosen as described in Section 2.8.

which constrains the available  $n$  values that can be chosen. Figure 2.16 shows the intersections of the resonant lines of Equation 2.23 along with the circular arc of Equation 2.24 in the tune plane, for which a chosen value of  $n$  will lie on a resonance. The operational  $n$  values and corresponding quad voltages in Run 1 are described in Section 2.8.

### 2.6.1 Coherent betatron oscillation

The muon beam consists of many muons, each individually undergoing betatron oscillations. If the phase of the oscillations of the individual muons are incoherent, then the beam can be thought of as a static entity, constant in time around the ring. However, due to injection and kicker effects which induce a particular phase space distribution on the injected beam, the beam itself can be said to oscillate. The beam

is then described by a width and mean dependent on the injection process, and the strength and phase of the kicker pulse, such that the phase distribution of the beam oscillates coherently every betatron wavelength<sup>4</sup>. Due to the mismatching of betatron wavelengths to the ring circumference in order to avoid resonances, a singular time slice of the distribution can be said to move around the ring over time. Individual detectors around the ring measure the beam in discrete pieces based on their individual azimuthal acceptances, where these acceptances depend on the radial and vertical characteristics of the beam. Because the radial betatron frequency is larger than half the cyclotron frequency, there is an aliasing effect such that the radial betatron motion of the beam is instead observed as an apparent slow-moving oscillation. We call the measurable signal of this coherent radial motion coherent betatron oscillation (CBO). See Figure 2.17 for a pictorial view of this phenomenon. Since the acceptance of the calorimeters depend on the beam properties, the CBO will modulate the  $\omega_a$  signal.

The frequency of the CBO is just the beat frequency between the cyclotron frequency and the horizontal betatron frequency

$$f_{CBO} = f_c - f_{x_{BO}}. \quad (2.25)$$

There is also a vertical CBO effect, but the non-aliased rate of oscillation is fast enough such that the effect tends to average out. However, the detectors are sensitive to oscillations of the vertical width of the beam, which is aliased in a similar way to the radial oscillation. Though the principles are the same, we call this effect the vertical waist (VW),

$$f_{VW} = f_c - 2f_{y_{BO}}, \quad (2.26)$$

---

<sup>4</sup>The four-fold quadrupole symmetry was chosen in order to minimize this beam ‘breathing.’



Figure 2.17: Marked by the black vertical lines are integer steps in the circumference of the ring, corresponding to the cyclotron wavelength  $\lambda_c$ . The blue line shows the motion of the beam due to the betatron oscillations  $\lambda_x$ . Since  $\lambda_x > \lambda_c/2$ , there is an aliasing effect in the observed signal, which is identified by the red line. To a single detector the beam appears to move slowly back and forth with  $f_{CBO}$ .

where the term *waist* refers to the minimum vertical width. Both of these frequencies are included in Table 2.2. The phase of the CBO signal varies systematically by detector, from 0 to  $2\pi$  around the ring. When adding all of the detector signals together, the CBO oscillations tend to cancel out. However, due to acceptance differences between the different detectors, the CBO oscillations are still observable in the data. When fitting the data to extract  $\omega_a$ , these effects must be accounted for in the fit function, as will be discussed in Section 5.3.1.

### 2.6.2 Beam debunching

As described in Sections 2.3 and 2.4, the muon beam is injected into the ring with a time spread of 120 ns and a range of momenta. At early times the beam will occupy a portion of the ring less than the whole since the cyclotron period is  $\sim 149$  ns. Therefore early in the fill the detectors located at discrete points around the ring will measure counts from the beam where there will be a fast oscillation in the signal due to this cyclotron period. As time increases throughout the fill, the momentum distribution of the muons will cause the beam to spread out within the storage ring

until the entire azimuth is filled. Since almost all muons are at the same momentum, it turns out that the lower momentum muons at smaller radii catch up to the tail of the higher momentum muons at the outer radii after many turns around the ring. By 30  $\mu$ s the muon beam has gone around the ring two hundred times. As the beam fills the storage ring, the cyclotron frequency in the data decreases and the beam debunches. This phenomena is referred to as the “fast rotation.” This debunching signal is seen in the data as shown in Figure 2.18. When dealing with the data and attempting to extract  $\omega_a$ , the typical procedure is to both bin out the fast rotation in periods of the cyclotron frequency, and to randomize each hit time by  $\pm T_c/2$  where  $T_c$  is the cyclotron period. In this way the fast rotation is removed entirely and the five parameter function described in Equation 2.13 remains satisfactory, barring other effects.

## 2.7 Corrections to $\omega_a$

Equation 2.3 is an idealized version of the spin difference frequency which ignores two important beam dynamics effects: torques exerted by the electric field and changes in the rest frame magnetic field resulting from the vertical pitching motion of the muons. Including practical experimental concerns, these two corrections must be applied to  $\omega_a$ .

### 2.7.1 Electric field correction

In the presence of an electric field, the spin difference frequency is altered to

$$\vec{\omega}_a = -\frac{q}{m}[a\vec{B} - \left(a - \frac{1}{\gamma^2 - 1}\right)(\vec{\beta} \times \vec{E})], \quad (2.27)$$

where now there is an extra term dependent on the electric field strength and the momentum of the particles. This extra term originates from the motional magnetic



Figure 2.18: In the data, the fast rotation signal is a fast (149.2 ns) modulation on top of the slower (4.365  $\mu$ s)  $\omega_a$  frequency. The plots here are from a subset of data from Run 1. In individual calorimeters at early times the fast rotation signal is seen to be very large, as shown on the top left. As time passes and the beam debunches, the amplitude of the fast rotation signal diminishes as shown on the top right. When adding all calorimeters together, the signal is reduced as shown in the bottom two plots, due to the fast rotation signal being unaligned in phase for the different detectors.

field  $\vec{\beta} \times \vec{E}$  that relativistic particles experience in an electric field. This is necessary to include since we use electrostatic quadrupoles for vertical focusing as described above. The second term cancels to first order for a specific momentum or value of  $\gamma$ . This “magic momentum” can be understood as the momentum at which a relativistic particle moving through an electric field has its spin exactly follow its momentum. This magic momentum is 3.094 GeV for muons, hence the momentum value of the injected muons. This value sets the energy and time scales of the experiment and has driven many of the design constraints, including the size of the storage ring, choice of the magnetic field magnitude, etc.

Not all muons will have the magic momentum however as described in the Section 2.6.2, and therefore a correction to the measured  $\omega_a$  frequency needs to be applied. Approximating the storage ring as having an electric field applied over the whole azimuth of the ring, the spin difference frequency for muons with momentum  $p \neq p_m$  (where  $p_m$  is the magic momentum) becomes

$$\omega'_a = \omega_a \left[ 1 - \beta \frac{E_r}{cB_y} \left( 1 - \frac{1}{a\beta^2\gamma^2} \right) \right]. \quad (2.28)$$

Here the motion of the beam is assumed purely azimuthal. This additional term is the electric field correction that then serves to lower the measured  $\omega_a$  frequency. Using the relation  $p = \beta\gamma m = (p_m + \Delta p)$ , after a little bit of simplification the electric field correction can be written as

$$C_E = \frac{\Delta\omega_a}{\omega_a} = -2 \frac{\beta E_r}{cB_y} \frac{\Delta p}{p_m}. \quad (2.29)$$

The last fraction can be related to the field index described in Equation 2.21 by

$$\frac{\Delta p}{p_m} = (1 - n) \frac{\Delta R}{R_0} = (1 - n) \frac{x_e}{R_0}, \quad (2.30)$$

since we know that the magic momentum muons are at the central radius  $R_0$  of

the storage ring. In this equation  $x_e = \Delta R$  is the equilibrium radius of the muon relative to the central storage radius. Noting that the radial electric field strength for a quadrupole is

$$E = \kappa x = \frac{n\beta c B_y}{R_0} x, \quad (2.31)$$

and assuming that it is perfectly radial, the electric field correction reduces to

$$C_E = -2n(1-n)\beta^2 \frac{xx_e}{R_0^2}. \quad (2.32)$$

Taking the time average of the beam motion, where  $x$  is simply equal to  $x_e$ , the correction becomes

$$C_E = -2n(1-n)\beta^2 \frac{\langle x_e^2 \rangle}{R_0^2}. \quad (2.33)$$

Since the equilibrium radius of the beam is set by the momentum distribution of the muons, this electric field correction can be determined by a measurement of the momentum spread of the beam which comes from an analysis of the fast rotation [46, 47]. For the precision goal of E989, the assumptions made in this derivation are acceptable [38] and results will be cross-checked with spin-tracking simulations as was done in E821 [29]. In E821 the electric field correction was approximately 500 ppb on  $\omega_a$  [29]. In E989 the scale of the correction will be the same considering the experimental principles are identical.

### 2.7.2 Pitch correction

Particles injected into the  $g - 2$  storage ring will have a vertical component of momentum which is parallel to the magnetic field vector (hence the need for vertically focusing electrostatic quadrupoles). This will slightly reduce the magnetic field seen by the muons in their rest frame. Including this motion into the spin difference



Figure 2.19: Beam motion  $\beta$  relative to the vertical and azimuthal axes Y and Z respectively.  $\psi$  is the pitch angle of the beam, and the dashed lines represent the parallel and perpendicular motions of the beam.

frequency,  $\omega_a$  becomes

$$\vec{\omega}_a = -\frac{q}{m}[a\vec{B} - a\left(\frac{\gamma}{\gamma+1}\right)(\vec{\beta} \cdot \vec{B})\vec{\beta}], \quad (2.34)$$

where now there is an extra term dependent on the vertical betatron motion of the beam. Similar to the electric field case, this term can be neglected to first order as the muon momentum is nearly all perpendicular to the field, but a correction again needs to be applied to  $\omega_a$  to account for this effect.

Since the muons in the storage ring will be oscillating vertically as they are focused by the quadrupoles, their momentum vectors will be pitching up and down relative to the azimuthal motion. This pitch angle will oscillate as

$$\psi = \psi_0 \cos(\omega_y t), \quad (2.35)$$

where  $\psi_0$  is the amplitude of the oscillation and  $\omega_y$  is the vertical betatron frequency. Shown in Figure 2.19 is an exaggerated example of the beam motion relative to the vertical and azimuthal axes. Assuming that the field is purely vertical,  $\vec{B} = B_y \hat{y}$  and

that the beam motion is in the vertical-azimuthal plane,

$$\vec{\beta} = \beta_y \hat{y} + \beta_z \hat{z} = \beta \sin(\psi) \hat{y} + \beta \cos(\psi) \hat{z}, \quad (2.36)$$

then  $\omega_a$  becomes

$$\vec{\omega}_a = -\frac{q}{m} [a B_y \hat{y} - a \left( \frac{\gamma}{\gamma+1} \right) \beta_y B_y (\beta \sin(\psi) \hat{y} + \beta \cos(\psi) \hat{z})]. \quad (2.37)$$

Using the small angle approximation such that  $\cos(\psi) \approx 1$  and  $\sin(\psi) \approx \psi$ ,  $\vec{\omega}_a$  can be separated into its vertical and azimuthal components

$$\omega_{ay} = \omega_a \left[ 1 - \left( \frac{\gamma-1}{\gamma} \right) \psi^2 \right], \quad (2.38)$$

$$\omega_{az} = -\omega_a \left( \frac{\gamma-1}{\gamma} \right) \psi. \quad (2.39)$$

Looking at Figure 2.19 again, it can be seen that the spin difference frequency can be resolved into its parallel and perpendicular components  $\omega_{\parallel}$  and  $\omega_{\perp}$  respectively. As the pitch angle of the beam motion oscillates about the azimuthal axes at a frequency much greater than the  $g - 2$  frequency, it can be seen that the parallel component averages to 0 over time. We then only care about the perpendicular oscillation of the beam, which can be determined with a simple rotation matrix such that

$$\omega_a \approx \omega_{\perp} = \omega_{ay} \cos(\psi) - \omega_{az} \sin(\psi) \approx \omega_a \left[ 1 - \frac{\psi^2}{2} \right], \quad (2.40)$$

where in the last approximation the small angle approximation was used once again, but this time with  $\cos(\psi) \approx 1 - \psi^2/2$ . The pitch correction then is the additional term which serves to lower the measured spin difference frequency. Taking the time average,

$$C_P = \frac{\Delta \omega_a}{\omega_a} = -\frac{\langle \psi^2 \rangle}{2}. \quad (2.41)$$

The pitch angle of the beam cannot be measured directly, however we know from Equation 2.22 that the angle of the beam can be related to the vertical distribution of the beam, such that

$$C_P = -\frac{n}{2} \frac{\langle y^2 \rangle}{R_0^2}, \quad (2.42)$$

where once again  $n$  is the field index,  $R_0$  is the radius of the ring at the center of the storage region, and  $\langle y^2 \rangle$  is the vertical width of the beam. The first two are known and the last can be measured experimentally by the straw tracking detectors. Just as in the case of the electric field correction, the assumptions made in this derivation are acceptable for the precision goal of E989, and results will be cross-checked with spin-tracking simulations. In E821 the pitch correction was approximately 300 ppb on  $\omega_a$  [29], and the scale for the E989 correction will be the same.

## 2.8 Run 1 in E989

Run 1 for E989 was conducted in the first half of 2018. Production data were gathered from March 22nd through June 29th. Because of accelerator, experimental, and practical concerns production data taking was interrupted at various dates. Due to hardware issues both kicker and quad voltages were originally lowered from their technical design values. Various voltage set points for both systems were identified and used in separate periods of the data taking, depending on the stabilities of the systems. The distinct designated precession frequency analysis datasets gathered by E989 and their associated parameters are shown in Table 2.3.

Due to the lower kicker voltages, the muon beam was stored on a central radius  $\sim 6$  mm offset from the central orbit of the storage ring, as shown in Figure 4.23. The chosen quad  $n$  values were 0.108 and  $0.120^5$ , corresponding to quad voltages

---

<sup>5</sup>The associated betatron wavelengths are 1.06 and 3.04 times the circumference of the storage ring respectively.

of 18.3 and 20.4 kV respectively [48]. During Run 1 it was discovered that some of the quad resistors were damaged, leading to longer RC time constants such that the quad voltages had not reached storage nominal at the beginning of the designated analysis portion of the data at 30  $\mu$ s, and were still changing over the course of a fill. See Figure 2-20. The muon beam was therefore seen to move as a function of time in-fill. See Section 4.4 for a summary of the muon beam characteristics for Run 1. As described in various sections in this chapter and in Section 4.4, these muon beam characteristics fold into the measurement of  $g - 2$  in a variety of ways, for which work is still on-going. The associated number of stored muons per fill for Run 1 as a result of these effects combined with injection was  $\mathcal{O}(4,000)$ , down from the  $\mathcal{O}(10,000)$  design goal.

All data listed in Table 2.3 was quality checked. If run conditions were found to be unstable or wrong in some way, the associated data was flagged and ignored in the analysis. A summary of the data quality control procedure is given in Reference [49], and the exact data quality parameters for the 60H dataset is detailed in Reference [50]. The total number of detected positrons above threshold that passed the data quality control was approximately  $1 \times 10^{10}$ , corresponding to a statistical error on  $\omega_a$  of  $\sim 400$  ppb, as calculated with Equation 2.16. See Chapter 6 for the final value for  $\omega_a$ .

**-mention that there are other datasets that are not included in the precession frequency analysis**



Figure 2.20: Traces for the high voltages as a function of time on some of the quad plates. The different plates are identified in the legend, where for instance Q1LT stands for the top long plate of quad 1. The beam is injected at the green line and the scraping procedure occurs until the quad voltages reach their design values, in this case 20.4 kV. As shown some of the high voltage traces do not behave in a smooth and fast exponential manner, due to damaged quad resistors. The traces in orange and brown are for good quad resistors, while the traces in red and blue show the results from damaged quad resistors.

Run 1 Precession Frequency Analysis Datasets						
Name	Date Acquired	Number $e^+ > E_{\text{Th}}$	n Value	Quad Voltage (kV)	Kicker Voltage (kV)	
60h	4/22–4/25	$9.34 \times 10^8$	0.108	18.3	128–132	
HighKick	4/26–5/02	$8.70 \times 10^8$	0.120	20.4	136–138	
9d	5/04–5/12	$2.13 \times 10^9$	0.120	20.4	128–132	
Endgame	6/06–6/29	$4.10 \times 10^9$	0.108	18.3	122–127	
Total Positrons Above Threshold		$8.03 \times 10^9$				

Table 2.3: The primary datasets acquired during Run 1 of E989 in 2018 and their associated parameters [51]. Other datasets were gathered but they are not used in the calculation of the precession frequency. Update the number of positrons column once all of the datasets have been opened and energy thresholds chosen. Potentially also add further columns of interest or split into multiple tables. Decide whether to include all datasets or just the ones I’ve analyzed. Fix up what I want for last row.

# Chapter 3

# Detector Systems

There is a variety of different detector systems used in E989. The primary detectors are the calorimeters which measure the  $\omega_a$  signal. In support of that measurement there are several auxiliary systems used for monitoring injection and beam dynamics. These include the T0, IBMS, and fiber harps. There is also a straw tracking detector which measures decay positron trajectories which can be related to muon beam dynamics and calorimeter measurements. Each of these systems will be described in the following sections.

## 3.1 Auxiliary detectors

### 3.1.1 T0

During data taking, a reference time must be chosen so as to align all different detector systems in time. When taking data from fill to fill, decay positron spectra must be aligned in phase. Without this functionality, analyzing the data from different systems and comparing them would be impossible. To do this a “T0” counter is placed just on the outside of the ring before the inflector. It is made up of a scintillating paddle connected to two photo-multiplier tubes (PMTs) [52, 53]. See Figure 3·1a. One PMT, PMT A, has a 1% neutral density filter resulting in low photo-electron statistics, and acts primarily as a timing measurement. The other, PMT B, has a 10% neutral density filter resulting in higher statistics, and acts as a shape counter and proxy for fill intensity. (In general the signals are very similar.) Together they provide a



(a) The T0 counter is made up of a scintillator in the middle shown in green, which connects with light guides to PMTs on the left and right.

(b) Time profiles for the two PMTs in the T0 counter for one of the eight bunches we receive at a time as described in Section 2.3. Each profile is an average of 100 such profiles. The x axis is in clock ticks, each of which is 1.25 ns.

Figure 3.1: A model of the T0 detector (left) and the signal it measures per fill (right).

measure of the injected beam profile in time, from which the timing alignments can be made. Some measured T0 pulses are shown in Figure 3.1b. The shape of the incoming pulses has a somewhat trident-like shape, with a very large spike in the middle of the time width, and two spikes on the outside edges. This shape owes itself to the accelerator complex, and varies from bunch to bunch.

### 3.1.2 Inflector Beam Monitoring System

While the T0 provides timing and intensity measurements, the inflector beam monitoring system (IBMS) provides measurements of the beam position properties as it passes through the inflector. This is useful because the injection aperture is so tight, and incoming beam parameters are tightly constrained. The IBMS system serves to provide a direct diagnostic handle on the phase space matching between the last accelerator components and the  $g - 2$  storage ring, helping to optimize the number of stored muons per fill [54]. The IBMS is made up of two scintillating fiber detectors,

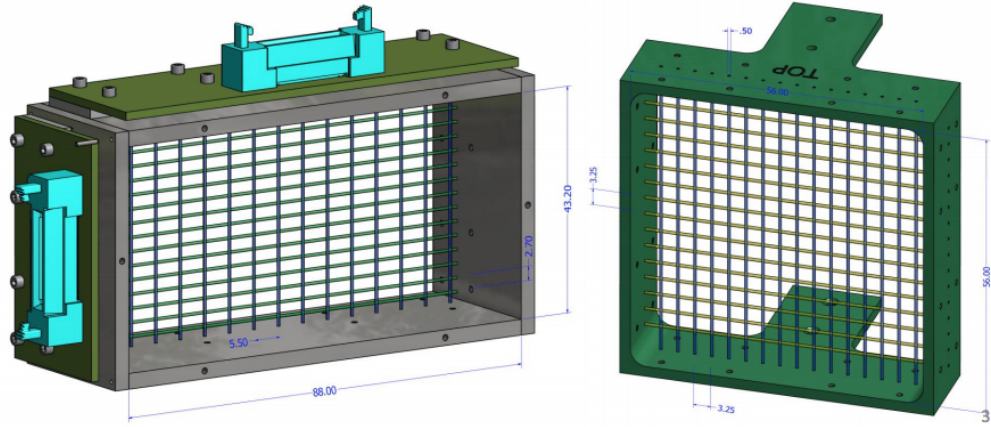


Figure 3·2: Models of the IBMS 1 and 2 detectors. Scintillating fibers form an array which detect particles as they pass through them.



Figure 3·3: The positions of IBMS 1, 2, and the planned 3rd device are shown with respect to the vacuum chamber and inflector.

as shown in Figure 3·2. These devices are placed at the outside of the magnet yoke before injection into the back hole of the magnet, and at the entrance to the inflector [55]. A third device is planned to be at or near the downstream end of the inflector. See Figure 3·3.

### 3.1.3 Fiber harps

The last auxiliary detector is the so called “fiber harp” system. It is made up of four scintillating fiber detectors that serve to measure the beam intensity as a function of time and position [56]. Two of the detectors measure the radial components of the



(a) Picture of one of the fiber harps. A row of seven scintillating fibers measures the beam intensity as a function of time at vertical or horizontal positions depending on which fiber harp is inserted.

(b) Shown are fiber harp beam intensity measurements for the horizontal fiber harp. Each spectra is from a single fiber, with the spectra at the top being at the greatest radial positions. The fast oscillations of the cyclotron frequency can be seen along with the slower oscillations of the CBO.

Figure 3·4: Fiber harp detector (left) and a sample of fiber harp measurements (right).

beam, and two measure the vertical components. Each pair of fiber harps are located  $180^\circ$  and  $270^\circ$  in azimuth clockwise from the inflector. One of these devices is shown in Figure 3·4a. The fiber can measure beam properties throughout the fill, providing a diagnostic tool which is sensitive to the scraping procedure and the CBO properties of the beam. An example of fiber harp measurements is shown in Figure 3·4b. However, because the fiber harps are a destructive measurement of the beam due to multiple scattering in the fibers, the system was designed to be retractable. They are inserted during special diagnostic or systematic runs, and are pulled out of the beam path during production data taking.

### 3.2 Calorimeters

Electromagnetic calorimeters are the primary detector in the E989 experiment, responsible for the  $\omega_a$  measurement. They measure arrival times and energies of the

decay positrons as they curl inward from the storage region.

### 3.2.1 Requirements and systematic effects

In order to determine  $\omega_a$  to the precision goal, there are specific requirements on the performance of the calorimeters. First, they must have a relative energy resolution of better than 5% at 2 GeV, in order for proper event selection above threshold [38]. The energy resolution requirement is modest but not strict because the important observable is the number of detected positrons above some energy threshold, where the optimal energy threshold can be determined empirically.

Second, they must have a timing resolution of better than 100 ps for positrons with energy greater than 100 MeV [38]. The calorimeters must be able to resolve multiple incoming hits through temporal or spatial separation at 100% efficiency for time separations of greater than 5 ns, or 66% of hits for time separations less than 5 ns, in order to reduce the pileup systematic effect. Pileup is the term used for when multiple particles impact the detector within the deadtime of the detector such that they are registered as a single hit. Unresolved pileup means that the number of detected positrons above threshold is mis-measured. Since pileup is a time-dependent effect, where pileup decays with a lifetime approximately equal to half the muon lifetime, this leads to a mis-measurement of  $\omega_a$ , see Section 5.2.1. The requirements stated here assist in reducing the pileup systematic error below a target goal of 40 ppb.

Third, the energy response of calorimeters for measured hits must be stable to  $< 0.1\%$  over a fill (700  $\mu$ s) [38]. The long term energy response stability over a time period of order seconds must be  $< 1\%$ . The energy response of a detector as a function of time is typically referred to as the gain of the detector, where technically the gain refers to the amount of current output per detected hit. The gain depends on the temperature stability and hit rate. After a hit, the measured energy fraction of a following hit drops sharply and then rises exponentially back to one. This is

referred to as the short-term double pulse (STDP) effect. At injection many particles are injected into the ring and there is a large amount of secondary particles incident on the calorimeters. The accumulation of all the individual STDP effects ends up causing a large gain drop at the beginning of each fill. This is typically referred to as the in-fill gain (IFG) effect. Hits with mis-measured energies due to these effects can thus be excluded from the fitted histogram if their energies drop below threshold, leading to another systematic effect and subsequent error in the  $\omega_a$  measurement. (Temperature changes vary over time scales greater than a fill, so they don't contribute to the systematic error.) The requirements stated here, along with the use of a laser calibration system (Section 3.2.3), assist in reducing the gain systematic error below a target goal of 20 ppb.

### 3.2.2 Harware

There are 24 calorimeters located symmetrically around the inside of the ring placed flush to the vacuum chamber wall, as shown in Figure 3.5a. (Indeed the shape of the vacuum chambers were designed so as to reduce multiple scattering of the decay positrons before entering the calorimeters.) Each calorimeter sits on a board extending out from a cart which contains the electronics that power the calorimeters and read out the data. The carts help to relocate magnetic materials away from the field region to avoid perturbing the magnetic field, and provide easy access to the electronics while removing them from the positron decay path region.

Each calorimeter consists of 54 channels of  $\text{PbF}_2$  crystals arrayed in a 6 high by 9 wide array, for a total of 1296 channels. Each crystal is  $2.5 \times 2.5 \times 14 \text{ cm}^3$  and is wrapped in black Tedlar® foil. The  $\text{PbF}_2$  material has an index of refraction of 1.8, and emits Cerenkov light as incident positrons with energy greater than 100 keV pass through the crystals [57]. Cerenkov light is naturally fast which improves the timing resolution of the incoming hits. The high density of the  $\text{PbF}_2$  ( $7.77 \text{ g/cm}^3$ ) gives it



(a) In black are the calorimeter carts, which house the electronics for the calorimeters. They hold up a board upon which the calorimeter rests. The calorimeter as shown is pushed flush to the vacuum chamber on the left.

(b) Shown is the backside of a calorimeter. The clear blocks are the PbF<sub>2</sub> crystals, each of which has a SiPM mounted onto the back of them.

Figure 3-5: Calorimeter systems relative to the vacuum chamber (left) and an individual calorimeter (right). **probably update these pictures at some point**

a short radiation length (9.3 mm), such that the energy deposition from the incident positrons is nearly 100% over the length of the crystal. The black foil is used to eliminate light transmission between crystals to improve position reconstruction, as well as reduce internal reflection to reduce pulse width and improve timing resolution [58]. The energy deposition from the incident positrons is typically restricted to only one or two crystals. The segmentation of the calorimeter combined with the black wrapping helps the spatial and temporal resolution of the detected pulses. See Figure 3-5b for a picture of the calorimeter crystals.

Each crystal is paired with a large area silicon photo-multiplier (SiPM) sensor which detects the emitted Cerenkov light. SiPMs are compact, operable in high magnetic field regions, have very linear responses for operation at MHz rates, are suited to measuring Cerenkov light due to their high photo-detection efficiency in the wavelengths of interest, and have a high degree of gain stability [58]. The SiPMs



Figure 3.6: Output pulse from a SiPM in black dots, overlayed with a fit template.

used are designed by Hamamatsu and detailed in Reference [58]. They sit on printed circuitry boards (PCBs) devoid of magnetic materials, which are designed to preserve the fast SiPM pulse shape. The combined properties of the chosen SiPMs, their electronic boards, and the  $\text{PbF}_2$  crystals results in an energy resolution of  $(4.6 \pm 0.3)\%/\sqrt{E/\text{GeV}}$ , a timing resolution of 20 ps, and a pulse width of 5 ns, satisfying the stated requirements earlier [57, 58]. Details of the pulse fitting algorithms are shared in Section 5.1. The SiPMs can be seen in Figure 3.5b. Finally, 12-bit waveform digitizers (WFD) sample each SiPM channel at a rate of 800 mega-samples per second with a 1 Gb memory buffer and the data are transferred to a bank of GPU processors for on-line data processing [59]. The timing resolution of these WFDs is  $< 50$  ps for most pulse amplitudes. A typical pulse from an incident positron is shown in Figure 3.6.

### 3.2.3 Laser calibration system

In order to satisfy the gain requirements of the calorimeter detectors, a laser calibration system is used. This system monitors the SiPM responses over short and long time scales to  $< 0.04\%$  [60]. The system consists of six different lasers and a suite of optical devices. The light from the six lasers is piped to a board mounted on the

front face of each calorimeter through optical fibers. This board contains right-angle prisms which deflect the laser pulses directly into each calorimeter crystal, for all 1296 channels. The lasers can be pulsed at various intensities, both in-fill to monitor the STDP or IFG effects, and out-of-fill to monitor for long term drifts due to changing temperatures or detector degradation. The SiPM measured response is compared to local known source monitors in order to calibrate the SiPM energy response. Corrections to the gain of the calorimeters can thus be determined and applied to the hit energies. Simultaneously the laser system allows for measuring the timing resolution of the SiPMs, and in general performing diagnostic tests with the calorimeter. Lastly, the laser system is used to time align the different calorimeter channels by outputting a sync pulse to each channel at the beginning of every muon fill.

### 3.3 Straw trackers

As described in Section 2.6, the muon beam moves as a whole within the storage ring. As explained in Section 2.2, the muon beam distribution ties into the measurement of the average magnetic field. The primary detector system used to measure this behavior and determine the muon beam distribution is the “straw tracker” system. The straw trackers characterize the beam in a non-destructive fashion by measuring decay positron trajectories and extrapolating them back into the storage ring. They serve to provide the direct measurement of the pitch correction as described in Section 2.7.2, determine the momentum distribution of the beam, and characterize parameters of the CBO which tie into the calorimeter  $\omega_a$  analysis. Decay positron trajectories can also be extrapolated forwards into the calorimeter, in order to cross-check calorimeter measurements to help resolve pileup. Finally, the trackers also serve as a measuring device to search for a possible muon electric dipole moment. The existence of such a thing would tilt the precession plane of the muons and subsequent decay positron tra-

jectories which the trackers are sensitive to. Details of the beginnings of such a search are given in Reference [61]. The details of the track reconstruction and analysis will be given in Chapter 4. Here will be given a description of the detectors themselves and how they work.

In general, straw tracking detectors work by measuring hits in gas filled straws [62]. Each straw is made up of a cylindrical piece of thin material, typically Mylar with a conductive aluminum coating, and contains a wire at the center of the straw held at high voltage,  $\mathcal{O}(1000\text{ V})$ . The minimal amount of material in straw trackers serves to reduce multiple scattering of incident particles, and was the reason a straw tracker system was chosen over other tracker types. Fast moving particles ionize the gas as they pass through it, and the resulting ions are drawn to the wire and straw surface (positive and negative charges respectively). As the ions move to the wire, they enter a high electric field region that causes them to speed up, hit other gas molecules, and create more ions. This produces an avalanche gain effect which amplifies the original signal. Once the ions reach the wire and straw surface, an electrical signal is read out telling what the drift time of the ions was, which can be related to the radius or distance of closest approach (DCA) the particle passed relative to the wire. The straws therefore measure drift circles in a plane perpendicular to their physical orientation. The calculations of these DCA's and their errors is done using a simulation program for gaseous detectors called Garfield [63, 64]. By combining several such measurements in time and space, we are able to reconstruct tracks of incident particles. See Figure 3.7.

Our straws are 5 mm in diameter and contain a 50:50 mixture of argon-ethane gas [65]. The argon component serves as the gas to be ionized. The fast moving ions near the wire in addition to producing more ions, will incite excited states of the gas, which emit photons when de-excited. These photons can restart the whole ionization

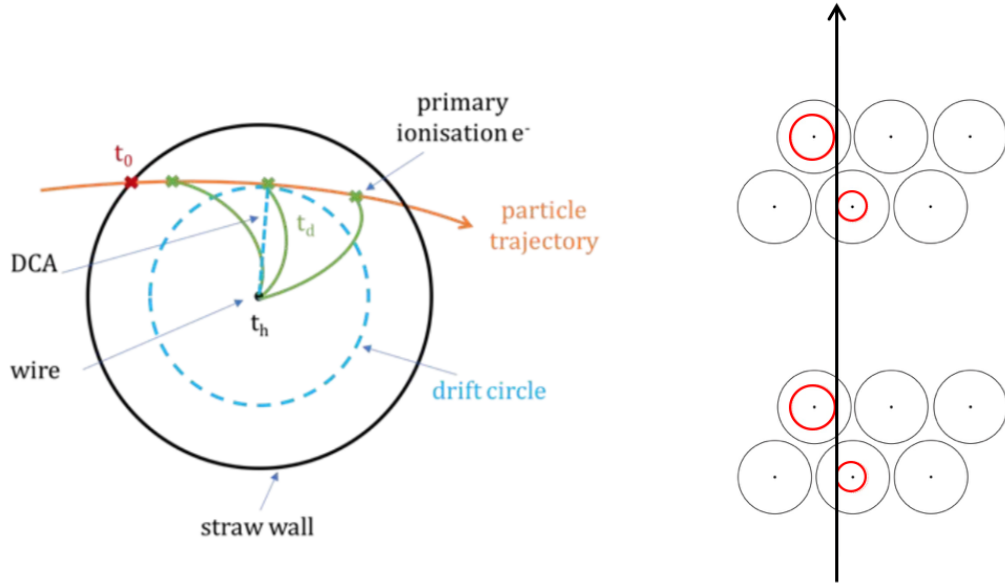


Figure 3.7: Diagrams showing the determination of a drift time  $t_d$  and hit time  $t_h$  from an incident ionizing particle (left) and the combination of several such hits to produce a track (right). Diagram on left courtesy of Saskia Charity.

and avalanche process over again as they can escape the avalanche region, leading to a break-down of the system. The ethane therefore serves to absorb the photons with its large number of molecular degrees of freedom and photo-absorption characteristics [65]. The wire has a radius of  $25\text{ }\mu\text{m}$  and is made up of gold-plated tungsten. The Mylar walls have a width of  $15\text{ }\mu\text{m}$  and are wound in a double spiral shape in order to improve the electrostatic shielding of the wire and reduce the gas leak rate of the straws [65]. The DCA resolution of hits within the straws is approximately  $120\text{ }\mu\text{m}$  to  $150\text{ }\mu\text{m}$ .

A single tracker module is shown in Figure 3.8. Each tracker module consists of 4 layers of 32 straws each with stereo angles of  $\pm 7.5^\circ$ , for a total of 128 straws per module. The first two straw layers are designated as “U” layers, and are oriented with the tops of the straws at a greater radial position than the bottoms of the straws. The second two layers are designated as “V” layers, and are oriented with



Figure 3·8: A straw tracker module. The first layer of silver Mylar straws with a stereo angle of  $7.5^\circ$  can be seen, with the other three straw layers hiding behind it. In black on the left is the carbon fiber post which holds the end of the module in a fixed position. Electronics live in the top and bottom manifolds above and below the straws, and cables connect from those electronics through small apertures to external electronics which plug in on the right.

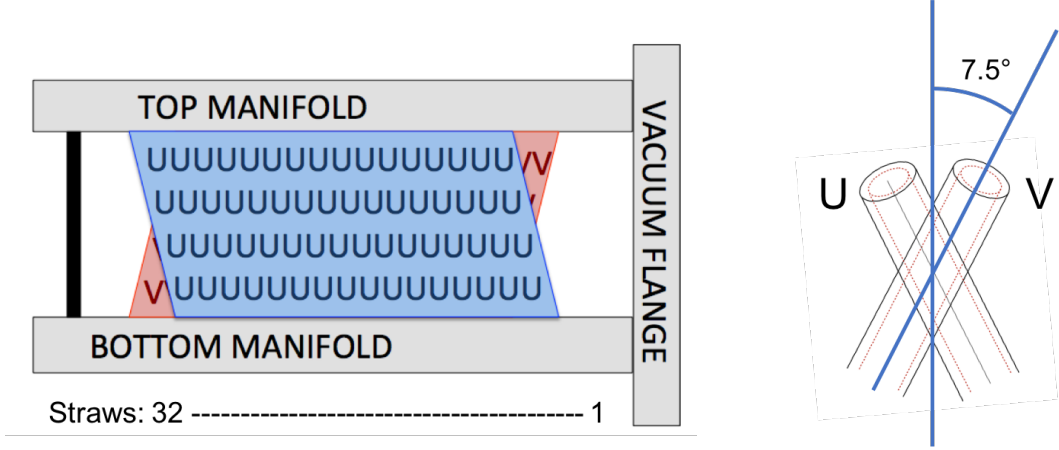


Figure 3.9: Orientation of U and V straws in the tracker module.

the bottoms of the straws at a greater radial position than the tops. Both U or V layers are collectively referred to as the U and V views of the module respectively. See Figure 3.9. The two layers in each view are shifted half a straw diameter horizontally from one another in order to help resolve which side of the wire any incident particles passed, Section 4.2.6. The two types of layers are non-parallel to each other in order to resolve incident tracks in 2D space. The small stereo angle both improves the straw measurement area as electronics can be kept out of the positron decay path region, and improves the radial momentum resolution of the fitted tracks, since both views measure mostly in the horizontal plane. The active straw measurement area is approximately 10 cm high by 20 cm wide. A carbon fiber post sits at the outside end of the module to provide structural rigidity to the module, and keep the straw wires under tension.

There are two tracker stations, each consisting of eight tracker modules. The two stations are located at positions in front of calorimeters 13 and 19, or at approximately 180° and 270° clockwise from the inflector. These are designated as Tracker Station 12 and Tracker Station 18 respectively, where the numbers come from which vacuum chamber the trackers reside in. There is also a third station just after the

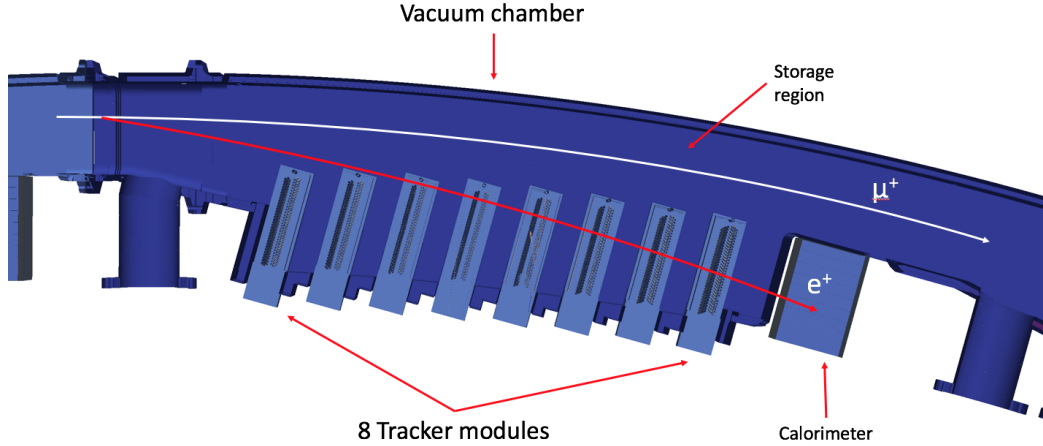


Figure 3·10: Birds eye view of a model of a vacuum chamber containing a tracker station, and the associated calorimeter. Each tracking station consists of eight tracker modules.

inflector, which currently sits empty of any tracker modules. The straw tracker modules sit inside the vacuum chamber in specially modified vacuum chamber sections in a staircase-like pattern that follows the curvature of the ring. See Figure 3·10 and Figure 3·11. The number of modules and their orientation in each station was chosen to provide a long measurement arm for precise momentum measurement of the incident tracks. The modules sit inside the vacuum in order to eliminate multiple scattering in air and produce better reconstructed tracks. Due to their proximity to the storage region, the tracker modules are located in a region of high field non-uniformity. Though the acceptances between the trackers and calorimeters are not identical, their close proximity facilitates comparison between the two measurement devices.

### 3.3.1 Tracker readout electronics

The readout electronics for the system are split into two groups, the front-end and back-end. The front-end electronics were built and tested in the Boston University Electronic Design Facility. They start with ASDQ (Amplifier Shaper Discriminator

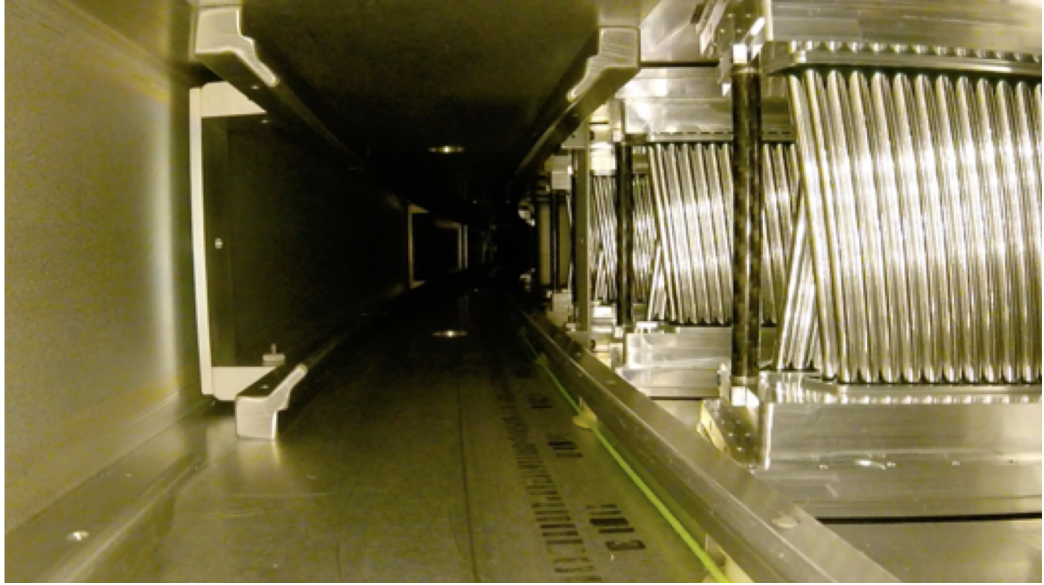


Figure 3.11: View of the tracker modules from within the storage ring. Muons move forward into the page, some of which decay to positrons which then pass through the trackers arrayed on the right. The carbon fiber post for each module can also be seen.

with charge ( $Q$ ) chips on boards that plug down directly onto the straws and provide the main signal, Figure 3.12a. Each ASDQ plugs onto sixteen straws. These ASDQ boards are application specific integrated circuits (ASICs) which read out the signal from one end of the straws and shape and discriminate that signal, as well as provide some baseline restoration and tail cancellation. The ASDQs and their associated components are contained within thin aluminum manifolds above and below the straws. The physical footprint of these boards and components was minimized in order to increase the straw measurement area. The signals from the ASDQs are passed through Flexi Cables to Time to Digital Converter (TDC) boards which time stamp the signals with 625 ps precision [65], Figure 3.12c. The Flexi Cables are flexible and thin such that the cables can be passed through the thin aperture shown on the right of Figure 3.8. High voltage is provided to the sense wires with high voltage boards, which pass the voltage through the ASDQs. A feedthrough board

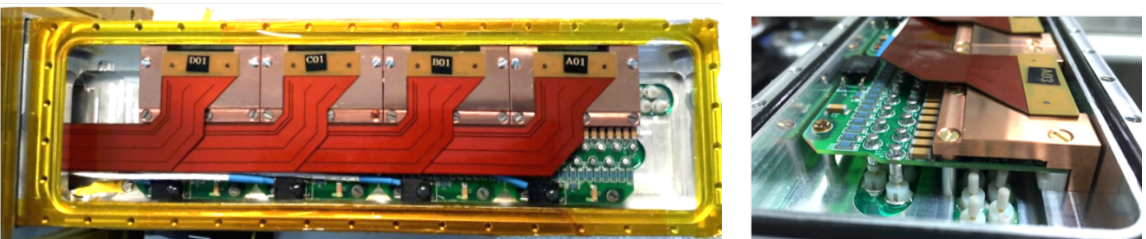
provides the interface between the TDCs and Flexi Cables, as well as the high voltage signal, Figure 3·13. They serve a dual purpose of providing the gas seal. Finally, there are logic boards that serve as the interface between the TDCs and the back-end electronics. They manage the clock and controls for the TDCs and store data onto FPGAs, which are piped out through a high throughput optical fiber connection. The logic boards, high voltage boards, and TDCs are all housed within an aluminum box which provides RF shielding, Figure 3·14. In each module there are eight ASDQs, four TDCs, two feedthrough boards, two high voltage boards, and two logic boards. An overview diagram of the front-end readout chain is shown in Figure 3·15. The back-end electronics consist of FC7s, one per tracker station, and a single AMC13 for all tracker stations. These modules provide clock and DAQ services to the whole tracker system, and ultimately pipe out the data to where it can be saved on disk.



(a) ASDQs contained within the aluminum manifold (left) that plug down onto the straws (right).



(b) Copper cooling bars (left) keep the ASDQs cool, and a high voltage spacer (right in white) keep the high voltage components isolated.

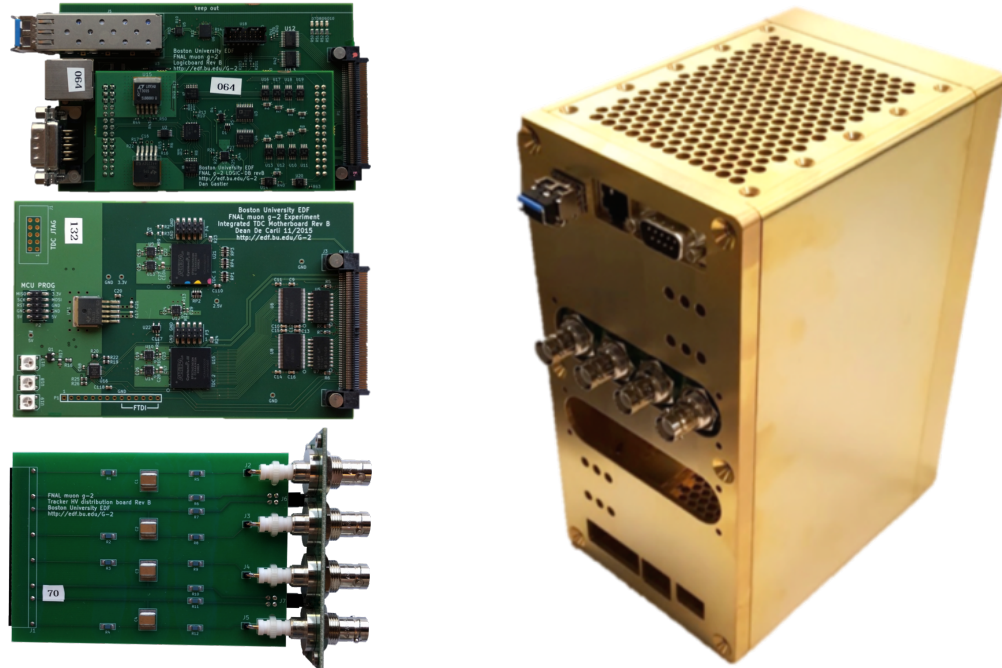


(c) Orange Flexi Cables plug down onto the ASDQ boards and run left through a small aperture in the tracking detector to the TDCs.

Figure 3-12: ASDQs and associated components which read out the signals from the straws. Images courtesy of James Mott.



Figure 3.13: Tracker feedthrough board. The feedthrough board plugs onto the end of the tracker snout to form a gas seal (left). Outside of the gas seal, a logic board, two TDCs, and a high voltage board all plug into the feedthrough board. Flexi Cables plug into the back side of the feedthrough board (right).



(a) A logic board (top), TDC (middle), and high voltage board (bottom).

(b) The aluminum housing which houses the front-end readout boards.

Figure 3.14: The front-end readout boards (left) and their housing (right). The logic and high voltage board connectors can be seen peeking out of their respective slots in the housing. Images courtesy of James Mott.



Figure 3.15: Front-end tracker electronics readout chain. Courtesy of James Mott.

## Chapter 4

# Track Reconstruction and Analysis

As described in section 3.3, the straw trackers are used to provide information about the muon beam, important for the calorimeter  $\omega_a$  analysis, calculating the  $\omega_a$  pitch correction, and determining the spatially weighted magnetic field seen by the muons. The track reconstruction is performed in three stages: First, individual hits in the tracker are grouped into individual tracks in the finding stage. Second, a best trajectory is fit to grouped hits in the fitting stage. Third, the best fit trajectory is extrapolated back to the storage region or forwards to the calorimeter in the extrapolation stage. A fourth refinement stage is planned but not yet implemented, which would add or remove hits in the finding stage based on the results of the fitting and extrapolation stages.

As a brief aside, every stage of the track reconstruction is performed in the event-processing framework known as *art* [66]. The *art* framework is a collection of modularized stages in a C++ framework useful for reading, reconstructing, filtering, analyzing, and writing data, among other things. Most Fermilab experiments now use *art*, including E989.

### 4.1 Track finding

The track finding stage consists of pattern recognition routines in order to group individual hits into separate sets corresponding to individual incident tracks. The general implementation of these pattern recognition routines is relatively straightforward [67],

68]. Hits across all modules are grouped in time windows called time islands, with an average width of 40 ns and a max width of 100 ns. Within those time islands hits are then grouped into clusters. Clusters consist of one or two hits for each U or V view per module. As a reminder the U and V views of a module consist of the two U or V layers in that module, Section 3.3. Hits are only clustered if they lie in close proximity in time and space to one another. The spatial constraint is defined as the difference in hit straw numbers, from 0 to 31 for the 32 straws per layer, which by default is limited to  $\leq 4$ . Neighboring hit clusters in the same module are then grouped to form seeds, one per module. Finally, seeds are grouped together module by module from one end of the tracker to the other to form what are called track candidates. The seeds are formed and grouped into track candidates again only if they lie close in time and space to one another. The entire track candidate formation process occurs for all hits in a time island to find as many real tracks as possible. See Figure 4.1.

After a track candidate has been formed a number of checks are made before passing it on to the fitting stage. If hits, clusters, or seeds are found to be shared among multiple track candidates, the candidates are dropped. Likewise, a track candidate is dropped if it is made from seeds consisting of only one type of view, or if the track candidate has less than six hits. There are also various small geometry and timing algorithms to improve the track candidates, such as removing hits from secondaries [69]. The  $t_0$  time for the track candidate is calculated as the mean time of all hits, with some fixed offset at the end. This  $t_0$  is helpfully constrained by geometry effects, where for a straight track passing through two layers in the same view, the sum of the drift times adds up to a constant. The track candidate is supplied with an original momentum and position guess at the start of the track by fitting a circle to the hit straw wires in the horizontal plane. The final track candidates are passed on to the fitting stage.



Figure 4·1: Hits in a tracker station in a single time island. The black dots indicate the position of the straw wires, while the blue and red points indicate hits. In blue is the first formed track candidate in the island, formed from separate seeds in different modules. The track finding algorithms will move onto the remaining hits in the time island to attempt to form other track candidates, one of which is easily observable by eye.

## 4.2 Track fitting

The track fitting stage takes the track candidates from the track finding stage, and outputs a best fit trajectory to those candidates. This includes optimal state vectors and error matrices for the track at each measurement plane and at a fictitious starting plane at the entrance to the straw tracking detector. The track fitting routines can roughly be split into two parts, error propagation and the actual fitting and improvement of the track. The implementation of these parts go hand in hand, and will be described in turn. Details of the track fitting code itself is described in Reference [70].

### 4.2.1 Error propagation and coordinate systems

The process of error propagation involves taking track parameters and error matrices (which describe the spread in those track parameters) and transporting them along discrete steps from one point to another, accounting for changes due to any present magnetic fields or material along the step paths. There is a set of error propagation routines originally written in Fortran by the EMC collaboration, called “Geometry and Error Propagation” or Geane [71]. Geane works by propagating particles along their average trajectories neglecting the effects of discrete processes, using a helix equation along small enough steps where the change in the magnetic field is small. These routines were used in the E821 experiment as well as the PANDA and FINUDA experiments with some success [72]. The Geane routines were at one point converted to C++ and added to Geant. The strength of using Geane within a Geant simulation lies in its direct access to the Geant geometry and field. This is crucially important for the E989 track fitting because the trackers live in a region of high field non-uniformity. Shown in Figure 4.2 is the location of the tracker with respect to the radial and vertical fields as calculated in Opera2D and included in the E989 Geant4

simulation. As shown the radial field in the tracker region rises from 0 T at the outer ends to roughly 0.3 T at the inner top and bottom ends, and the vertical field drops approximately 50% from the storage dipole field of 1.451 T. These large field gradients over the tracking measurement space must be handled appropriately, which Geane does nicely.

Predicted track parameters in Geane are a function of path length

$$p_l = F_{l,l_0}(p_0), \quad (4.1)$$

where  $p_0$  are some original tracker parameters and  $p_l$  are the updated ones. The path length  $l$  can be defined or limited how one wishes, and typically corresponds to a single step in the Geant4 simulation. The track parameter vectors  $p$  are defined in some coordinate system. In the Geane routines these track parameters are  $5 \times 1$  vectors either defined in the “free” (curvilinear) system

$$\frac{1}{p}, \lambda, \phi, y_\perp, z_\perp, \quad (4.2)$$

or the “surface” (detector) system

$$\frac{1}{p}, \frac{p_v}{p_u}, \frac{p_w}{p_u}, v, w. \quad (4.3)$$

In the free system, the  $\lambda$  and  $\phi$  parameters are the dip ( $\pi/2 - \theta$ ) and azimuthal angles respectively, while the  $y_\perp$  and  $z_\perp$  parameters are defined as being in the  $XY$  or  $XZ$  global Geant4 planes and orthogonal to  $x_\perp$ , where  $x_\perp$  is defined as being along the momentum vector of the particle. See Figure 4.3. In the surface system, the UVW coordinates are defined with any two orthogonal vectors  $V$  and  $W$ <sup>1</sup>. The surface system is most usefully defined in the tracker reference frame, where the modules are

---

<sup>1</sup>For clarification, the UVW surface system has nothing to do with the UV orientations of the straws at this time.



(a) Vertical magnetic field



(b) Radial magnetic field

Figure 4.2: Shown are the vertical (top) and radial (bottom) magnetic fields of the storage ring magnet in and around the storage region as calculated in Opera 2D. The horizontal and vertical axes are the radial and vertical coordinates of the ring respectively. The center of the storage region lies at 7.112 m along the horizontal axis. The contours represent the strengths of the vertical and radial magnetic fields. The black box shows the rough location of the tracker with respect to the ring. It can be seen that there is a large field non-uniformity within the tracker space.

staggered in a local Z coordinate, the local Y coordinate is vertical, and the local X coordinate increases with straw number. See Figure 4.4. The surface system is then defined as

$$\frac{1}{p}, \frac{p_x}{p_z}, \frac{p_y}{p_z}, x, y. \quad (4.4)$$

In both free and surface systems the track is represented by one momentum parameter, two directional parameters, and two position parameters. Needing six independent parameters to describe a particle in space and momentum (three momentum and three position parameters), one parameter is left out and taken as a known variable. For Geane this is taken either as a known path length in the free system, or a known U coordinate in the surface system (or known Z coordinate in our tracker reference frame). In our tracker reference frame, the 32 straw layers corresponding to a tracking station are defined at known local Z coordinates. The path lengths for steps in Geane can be set to be equal to the distance for a track to travel between between detector planes, and therefore the track parameter dependence on the path length can instead be replaced by a dependence on plane number. The number of degrees of freedom per track is the number of measurement planes it hits,  $N$ , minus 5 for the number of track parameters.

The  $5 \times 5$  error matrix on a plane calculated in Geane describing the expected distribution in true parameters about the average ones is defined as

$$\sigma_N^{ij} = \langle p_N^i p_N^j \rangle - \langle p_N^i \rangle \cdot \langle p_N^j \rangle, \quad (4.5)$$

where i and j are track parameter indices and  $N$  is some plane number. This error matrix will include effects from multiple scattering, delta ray production, ionization, and bremsstrahlung [71, 72, 73]. These matrices are transported from plane to plane by what are called transport matrices, where the  $5 \times 5$  transport matrix elements



Figure 4.3: Free (left) and surface (right) tracking coordinate systems.

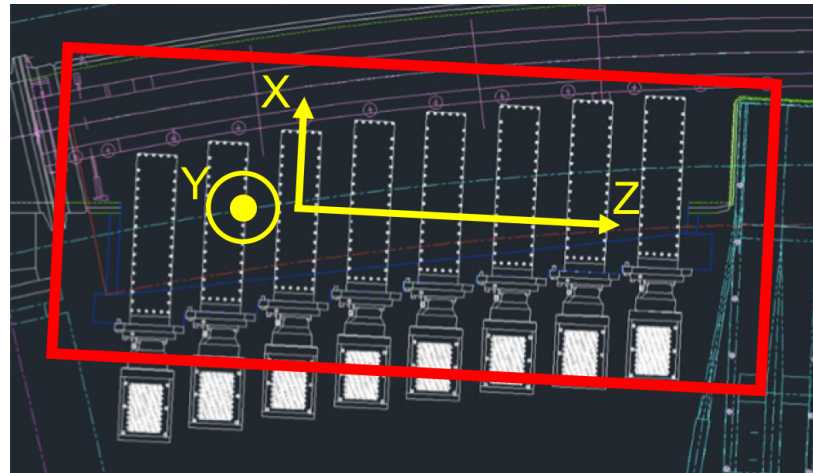


Figure 4.4: Shown is a model view of a tracker station in relation to the magnetic ring. Tracker modules are shown in white. Around the tracker measurement area is defined a coordinate system called the tracker reference frame. In that frame, the X coordinate is directed outward along the straws nearly radially, the Y coordinate is directed vertically up, and the Z coordinate is directed along the direction that the tracker modules are staggered.

between two planes are defined as

$$T_{N,N-1}^{i,j} = \frac{\partial p_N^i}{\partial p_{N-1}^j}. \quad (4.6)$$

The transport matrix  $T$  is a Jacobian between planes which expresses the infinitesimal changes in parameters at some plane (or path length) with respect to the parameters at some previous plane (or previous path length):

$$\delta p_N = T_{N,N-1} \delta p_{N-1} \quad (4.7)$$

Note that the transport matrix does not propagate the track parameters themselves as does an equation of motion. The error matrix is propagated forward from one plane to another by

$$\sigma_N = T_{N,N-1} \sigma_{N-1} T_{N,N-1}^T + \sigma_{\text{material}}, \quad (4.8)$$

where  $\sigma_{\text{material}}$  is the added error due to material effects between the planes. See Figure 4·5. The calculation of the transport matrices themselves is done within the Geane routines in the free system on a step by step basis, where the derivation of the transport matrix elements is given in Reference [74]. It should briefly be pointed out that the transport matrix between any two planes (or number of steps) is the multiple of all intermediate transport matrices,

$$T_{N,N-2} = T_{N,N-1} T_{N-1,N-2}, \quad (4.9)$$

regardless of what reference system the matrices are defined in (as long as they are all consistent). Geane can convert the transport matrices between the free system and the surface system using further Jacobians, also derived in Reference [74]. When



Figure 4·5: Transport matrices are defined between straw planes, and error matrices are defined on the planes.

converting a transport matrix from one reference system to another,

$$T_{N,N-1}^s = A_N T_{N,N-1}^f A_{N-1}^{-1}, \quad (4.10)$$

where the  $s$  and  $f$  superscripts stand for the surface and free reference systems respectively, and  $A$  is the Jacobian between reference frames which is defined at a specific point or plane ( $A_N \neq A_{N-1}$ ). The error matrices are converted between reference frames in the usual way,

$$\sigma_N^s = A_N \sigma_N^f A_N^T. \quad (4.11)$$

Finally, while the tracker reference frame is nominally defined in the local XYZ coordinates as described previously, the straws themselves don't measure in that frame directly. As described in Section 3.3, the straws measure drift circles in planes perpendicular to the straws themselves. The measurements from U and V straws therefore lie on the U and V measurement axes shown in Figure 4·6, where the measurement of the drift circle is instead taken as a U or V coordinate to the left or right of the straw wire. To first order the U or V coordinate is the DCA of the hit, which can be corrected with the angle of the track to get a better estimate, as shown in Appendix A. It's important to note that out of the five track parameters each straw only measures a single U or V position. The new coordinate system is

defined as

$$\frac{1}{p}, \frac{p_u}{p_z}, \frac{p_v}{p_z}, u, v, \quad (4.12)$$

where this  $Z$  variable is the tracker reference frame  $Z$ , and the U and V coordinates here are non-orthogonal and different to those in Equation 4.3. The transformation between the  $XYZ$  and  $UVZ$  systems is given by

$$p^{UV} = J_5 p^{XY} \quad (4.13)$$

$$(4.14)$$

where  $J_5$  is a  $5 \times 5$  matrix defined by

$$J_5 = \begin{pmatrix} 1 & 0 & 0 \\ 0 & J_2 & 0 \\ 0 & 0 & J_2 \end{pmatrix} \quad (4.15)$$

and  $J_2$  is a  $2 \times 2$  matrix given by

$$\begin{pmatrix} u \\ v \end{pmatrix} = J_2 \begin{pmatrix} x \\ y \end{pmatrix} = \begin{pmatrix} \cos \theta & -\sin \theta \\ \sin \theta & \cos \theta \end{pmatrix} \begin{pmatrix} x \\ y \end{pmatrix}. \quad (4.16)$$

$J_2$  is easily determined from Figure 4.6. In order to transform the transport or error matrices from the tracker reference frame to the tracker measurement frame, the same relations as in Equations 4.10 and 4.11 apply,

$$T_{N,N-1}^{UV} = J_5 T_{N,N-1}^{XY} J_5^{-1} \quad (4.17)$$

$$\sigma_N^{UV} = J_5 \sigma_N^{XY} J_5^T \quad (4.18)$$

where the superscripts of  $XY$  or  $UV$  identify which coordinate system the objects belong to.



Figure 4.6: The straw tracker measurement reference system. The XYZ system here is the straw tracker reference frame.  $\theta$  is the same angle as the stereo angle of the straws, at  $7.5^\circ$ . U straws measure along the U axis and V straws measure along the V axis.

#### 4.2.2 $\chi^2$ minimization

The method for fitting and improving the track is a global  $\chi^2$  minimization algorithm that uses the transport and error matrices as described previously [71, 75]. This straightforward global fitting algorithm works because of the minimal amount of material contained within the tracker and the resulting small correlations between planes. For denser detectors with greater correlations, other fitting algorithms such as a Kalman filter should be used [72]. The following derivations and minimization assume measurements on planes in the tracker measurement frame described by Equation 4.12, but it should be noted that the results apply to any reference frame. A derivation for a  $\chi^2$  including no material correlations is presented followed by one which includes material correlations.

The  $\chi^2$  for a track is defined as the residuals between predicted and measured parameters on a measurement plane, divided by their errors, summed over all hit planes:

$$\chi^2 = \sum_{i=1}^N [(p_i(p_s) - x_i)^T (\sigma_i^{-1})(p_i(p_s) - x_i)] \quad (4.19)$$

$x_i$  are vectors of the measured track parameters on plane  $i$ ,  $p_i$  are vectors of the average predicted track parameters which stem from some general starting parameters  $p_s$ , and  $\sigma_i$  are the  $5 \times 5$  error matrices on the planes<sup>2</sup>. To first order the error matrices consist only of the measurement errors on the U and V parameters and exclude the effects of random material processes. These errors are located in the U and V diagonal elements (3, 3) and (4, 4) respectively, with corresponding resolutions of approximately 150  $\mu\text{m}$  as described in Section 3.3. At second order the material error matrices as calculated by Geane are added to the measurement errors. Because the measured parameters consist of solely U or V measurements, the  $x_i$  vectors are  $5 \times 1$  objects where only the (3) or (4) elements have any meaning respectively<sup>3</sup>. The errors on the non-measured parameters in the diagonals of the error matrix are taken as infinite, such that when the error matrix is inverted all corresponding rows and columns of the final matrix calculation on each plane reduce to zero and contribute nothing to the  $\chi^2$ .

By minimizing this  $\chi^2$  with respect to the starting parameters  $p_s$ , and evaluating it at the target best starting guesses  $p'_0$ , which are the parameters of interest, the track can be fit:

$$\begin{aligned} \frac{\partial \chi^2}{\partial p_s} \Big|_{p_s=p'_0} = 0 &= \sum_{i=1}^N \left[ \left( \frac{\partial p_i(p_s)}{\partial p_s} \Big|_{p_s=p'_0} \right)^T (\sigma_i^{-1}) (p_i(p'_0) - x_i) \right. \\ &\quad + (p_i(p'_0) - x_i)^T \left( \frac{\partial (\sigma_i^{-1})}{\partial p_s} \Big|_{p=p'_0} \right) (p_i(p'_0) - x_i) \\ &\quad \left. + (p_i(p'_0) - x_i)^T (\sigma_i^{-1}) \left( \frac{\partial p_i(p_s)}{\partial p_s} \Big|_{p_s=p'_0} \right) \right] \end{aligned} \quad (4.20)$$

The middle term is small and can be neglected assuming that the error matrix doesn't change much with respect to the choice of starting parameters. This is true

---

<sup>2</sup>The vector  $p_s$  has no numerical value at this time.

<sup>3</sup>A straw tracker module as a whole can be approximated as measuring in 2D space, but this leads to correlations between measured parameters which must be taken into account, as compared to the natural tracker measurement frame in 1D space of U or V for which there are no measurement correlations [76]. A fitting algorithm which fits the true measurement space of the drift circles themselves would be even better.

as the error matrix is already small due to the low amount of material in the tracker. (In tandem the error matrix doesn't change much from one fitting iteration to the next as long as the path length through the material remains about the same.) The first and third terms are identical in value, and so must therefore both separately be equal to zero. Equation 4.20 is therefore reduced to

$$0 = \sum_{i=1}^N T_{i0}^T \sigma_i^{-1} (p_i(p'_0) - x_i), \quad (4.21)$$

where  $T_{i0}$  is the transport matrix between the point at which the starting parameters are defined and plane  $i$  given by Equation 4.6:

$$T_{i0} = \frac{\partial p_i(p_s)}{\partial p_s} \Big|_{p_s=p'_0} \quad (4.22)$$

In minimizing the  $\chi^2$  the desire is to update some original set of starting track parameters  $p_0$  to the new best ones  $p'_0$ . This difference,  $\Delta p_0$ , can be determined by substituting the following into Equation 4.21,

$$p_i(p'_0) = p_i(p_0) + T_{i0}\Delta p_0, \quad (4.23)$$

which follows from Equation 4.7. After simplifying one arrives at

$$\Delta p_0 = \sigma_{p_0} \sum_{i=1}^N T_{i0}^T (\sigma_i^{-1}) (x_i - p_i(p_0)), \quad (4.24)$$

where

$$\sigma_{p_0} = \left[ \sum_{i=1}^N T_{i0}^T (\sigma_i^{-1}) T_{i0} \right]^{-1}. \quad (4.25)$$

$\sigma_{p_0}$  is a  $5 \times 5$  covariance matrix of the starting fit parameters, where the diagonals describe the fit errors in the 5 track parameters at that point.

To summarize, an initial set of starting parameters  $p_0$  are propagated forwards

in Geant to produce predicted track parameters, transport matrices, and error matrices. These objects along with the measured parameters are plugged into the  $\chi^2$  minimization algorithm detailed here to provide a  $\chi^2$  describing the goodness of the fit corresponding to those original starting parameters, an improvement  $\Delta p_0$  to those starting track parameters, and the errors  $\sigma_{p_0}$  on those starting parameters. This consists of a single iteration of the track fitting. In order to determine the predicted parameters of the track corresponding to the improved starting parameters, the procedure needs to be repeated, or at least the error propagation part. The track fitting is iterated until the  $\chi^2$  no longer improves, at which point the track fitting is said to have converged. Typically three or four iterations are enough to get a best fit track, as shown in Figure 4.14. As a reminder the initial set of starting parameters is given by a circle fit to the hit straws as described at the end of Section 4.1. The starting parameters for a track are defined on a virtual 0 plane parallel to the measurement planes, where the placement of the 0 plane is defined based on a track by track basis and is placed at a point 1 cm in front of the first straw tracker module that was hit. Note that there is remarkable robustness with respect to the initial starting parameters in fitting the track. Of course if the initial starting parameters are too poor, then the fit will not converge.

#### 4.2.3 Fits to idealized tracks in vacuum

The tracking algorithm was first built and tested in a toy Monte-Carlo Geant4 simulation, and then ported over to the full E989 simulation in *art*. In the initial tests of the track fitting material was turned off and the measured hits were defined as the truth hits with some known smearing. (The truth hits are accessible within the Geant4 simulation by defined “dummy plane” detectors which record hits at the straw measurement planes.) Plots showing the goodness-of-fit for the fitted tracks are shown in Figure 4.7. Beyond the goodness-of-fit plots, the other measure of how good the track



(a) P value distribution for all tracks. (b)  $\chi^2$  distribution for tracks which hit 24 planes.

Figure 4.7: Goodness-of-fit distributions for fitted tracks in vacuum, with no material effects. The P value distribution is flat, and the  $\chi^2$  distribution matches a normalized  $\chi^2$  pdf for 19 degrees of freedom which is overlayed in red. ( $\chi^2$  distributions for tracks which hit other numbers of planes are very similar.) Only tracks which have failed due to Geant4 reasons are excluded.

fitting is performing is to plot the truth pulls of the fit parameters. The truth pulls are defined as the residual between the fitted parameter and the truth parameter, divided by the fit error on that parameter:

$$\frac{\Delta p_0^i}{\sigma_{p_0}^{ii}} = \frac{p_{0,\text{fit}}^i - p_{0,\text{true}}^i}{\sigma_{p_0}^{ii}} \quad (4.26)$$

Since the  $\chi^2$  minimization returns fit parameters and errors on the starting plane, this is where the truth pulls are defined. Plots of the truth pulls for the five track parameters are shown in Figure 4.8, where each pull is a unit Gaussian as they should be for idealized results.

#### 4.2.4 Material correlations

Random processes due to material contribute to the error matrix in Equation 4.5 as described in Section 4.2.1. The random scattering of a particle trajectory at one plane means that there is an extra correlated error in all further planes, see



Figure 4.8: Truth pulls for the five fitted track parameters at the starting plane of the track, for tracks in vacuum with no material effects. The plots are shown on a log scale, and each are fit to a Gaussian in red. Each fit is consistent to a unit Gaussian with a mean of zero and an RMS of 1, showing that the track fitting is working properly. Only tracks which have failed due to Geant4 reasons are excluded.

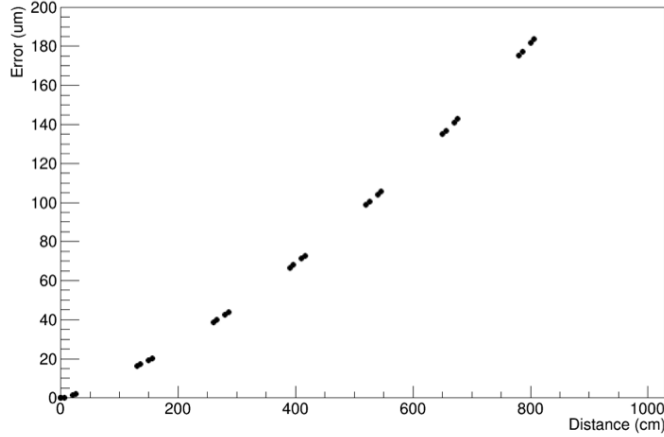


Figure 4.9: RMS error between the true track position and the average track position as a function of distance through the tracker. This error increases as a particle passes through more and more material. Each black point indicates the location of a straw measurement layer. If a track goes through the whole detector, on average the true position is nearly 200  $\mu\text{m}$  different from the average one.

Figure 4.9. Equation 4.19 does not take into account these material correlations between measurement planes when fitting the track. While it provides a decent approximation of the best fit track in the low material tracker, the  $\chi^2$  distribution is noticeably off as shown in Figure 4.10. To calculate a better estimate of the trajectory, a more general version of the  $\chi^2$  equation is used:

$$\chi^2 = (\vec{p} - \vec{x})^T (\sigma^{-1}) (\vec{p} - \vec{x}) \quad (4.27)$$

Here  $\vec{x}$  and  $\vec{p}$  are a  $5N \times 1$  vectors of the measured and predicted track parameters respectively, where  $N$  is the number of planes hit, and these objects are the combined vectors of the  $5 \times 1$  counterparts. Similarly,  $\sigma$  is a  $5N \times 5N$  matrix, where the  $5 \times 5$  diagonal block matrices are the individual plane error matrices described before, calculated between plane 0 and  $N$ . Calculating the  $\chi^2$  is now recasted from a sum over measurement planes into a single large linear algebra equation. At this point both calculations of the  $\chi^2$ 's are equivalent.



Figure 4.10: The  $\chi^2$  distribution for fitted tracks including material effects but excluding correlations in the calculation. The  $\chi^2$  distribution is noticeably different from the correct curve in red. **Axes labels and stats box don't look like previous plots, but not sure I can fix this besides overlaying stuff.**

The new format however allows for the material correlations between planes to be included, where these correlations are added as  $5 \times 5$  matrices in the off-diagonal blocks of the new large error matrix. The upper diagonals are given by

$$\sigma_{MN} = T_{MN}\sigma_N, \quad (4.28)$$

where  $\sigma_{MN}$  is the material correlation matrix between plane  $M$  and plane  $N$ ,  $T_{MN}$  is the transport matrix between the two planes, and  $\sigma_N$  is the ordinary error matrix as calculated from the 0 starting plane. **Need to cite or prove this equation, should do the latter but I can't quite remember the derivation at the moment.** The lower diagonals are just the transpose of Equation 4.28. The  $\chi^2$  is minimized in the same way as was done in the previous section such that the improvement to the starting track parameters  $\Delta p_0$  remains a  $5 \times 1$  vector and is given by

$$\Delta p_0 = \sigma_{p_0} \tau^T \sigma^{-1} (\vec{x} - \vec{p}), \quad (4.29)$$

$$\sigma_{p_0} = [\tau^T \sigma^{-1} \tau]^{-1}, \quad (4.30)$$

where  $\tau$  is a  $5N \times 5$  object of the individual transport matrices combined together.

Because  $\sigma$  is such a large matrix,  $5N \times 5N$  where  $N$  ranges from 6 to 32, inverting it is a slow process. The tracking must have a certain amount of speed for the data to be efficiently processed and fit, which makes these inversions unfeasible. Note however that the diagonal errors of infinity values for non-measured parameters would reduce all the corresponding rows and columns to 0 after the inversion, in the same way as described before. This fact can be taken advantage of by removing said rows and columns that would contribute nothing to the  $\chi^2$  anyway, and thus reducing the  $5N \times 5N$  size to  $N \times N$ . The corresponding rows and columns of the unmeasured parameters in the combined transport matrix  $\tau$  and residual vector are also removed, resulting in an  $N \times 5$  matrix for  $\tau$  and an  $N \times 1$  vector for the residuals. The covariance matrix  $\sigma_{p_0}$  remains a  $5 \times 5$  matrix. This improves the speed of the  $\chi^2$  calculation dramatically, while leaving the final calculation unaffected<sup>4</sup>. All pieces of the  $\chi^2$  calculation and minimization is done with a C++ linear algebra library optimized for speed called Eigen3 [77].

#### 4.2.5 Fits to simulated tracks including material effects

Once the material correlations are properly included, the  $\chi^2$  distribution is repaired, as shown in Figure 4.11. The plots in this section show the results of the track fitting in the full  $g - 2$  Geant4 simulation with material effects turned on. Truth measurements with 150  $\mu\text{m}$  smearing are once again used as the measured hits, and a cut of 3 MeV on the true simulated energy loss is made to remove tracks which would result in poor fits anyways (from hard energy loss physics processes). The comparison between the simulated and reconstructed energy loss for fitted tracks is shown in Figure 4.12. While there is a noticeable difference, the energy loss in general

---

<sup>4</sup>Note that these element removals are done just before the final calculation of the  $\chi^2$  and fit to the track and not at the beginning of the algebra, otherwise the plane material correlations are not properly included.



(a) P value distribution for all tracks. (b)  $\chi^2$  distribution for tracks which hit 10 planes.

Figure 4.11: Goodness-of-fit distributions for fitted tracks in the full  $g - 2$  Geant4 simulation with material effects included. The P value distribution is flat, and the  $\chi^2$  distribution matches a normalized  $\chi^2$  pdf for 5 degrees of freedom which is overlayed in red.

is small so it is acceptable. Truth pulls for the tracks are shown in Figure 4.13. It can be seen that there is a slight spread in results due to the material effects. This is to be expected and the vast majority of tracks still fit well. The number of iterations it takes to fit a track is shown in Figure 4.14. The number of planes a track hits and the corresponding momentum dependence is shown in Figure 4.15. The total momentum distribution and residuals to truth are shown in Figure 4.16. The track fitting has a momentum resolution of approximately 2% with just a slight dependence on the momentum of the track.

After the track fitting has determined the best fit parameters in the  $UV$  space, the returned parameters can be turned back into the tracker reference frame coordinates. Plots for the fitted vertical and horizontal momenta, positions, and corresponding residuals are shown in Figures 4.17 and 4.18. The forward momenta plots are omitted since the majority of the total momenta is in the forward direction. More extensive plots than what is shown here can be found in Reference [70].



Figure 4.12: Simulated true energy loss (black) vs Geane predicted energy loss (red) for fitted tracks. As shown there is a mismatch between the two. This is acceptable as the energy loss is in general very small compared to the total momentum of each track,  $200\text{keV} \ll 2\text{GeV}$ . Sources of energy loss come from ionization and bremsstrahlung processes, which account for the long Landau tail running off to infinity. Originally the Geane physics calculations were taking too much energy away due to bremsstrahlung processes in our low material tracker, so the energy loss calculations were modified slightly [70].



Figure 4.13: Truth pulls for the five fitted track parameters at the starting plane of the track for fitted tracks in the full  $g - 2$  Geant4 simulation with material effects included. The plots are shown on a log scale, and each are fit to a Gaussian in red. Each fit is close to a unit Gaussian with a mean of zero and an RMS of 1, but there are tracks which lie outside the Gaussian due to material effects and imperfect resulting fits.



Figure 4.14: Number of iterations for the track fitting to converge per track. The track fitting does not take less than three iterations, and the number of iterations is capped at ten.



(a) The number of planes hit peaks at 10, and falls off to the maximum number of planes at 32.

(b) The number of planes hit vs the momentum of the track. Tracks with higher momentum in general hit more planes.

Figure 4.15: Number of planes hit per track (left) and the momentum dependence (right).



(a) The fitted momentum distribution for tracks which tails off at approximately the magic momentum of 3.094 GeV.



(b) The residual between the reconstructed and true total momentum. The RMS is approximately 40 MeV, though there are some tails which spread out from the distribution.

(c) The relative residual between the reconstructed and true total momentum. The RMS is approximately 2.4 %. This plot includes tracks of all momenta; in general the resolution of the total momentum is around 2% for all energies.

Figure 4.16: Fitted track momentum distribution and corresponding residuals to truth.

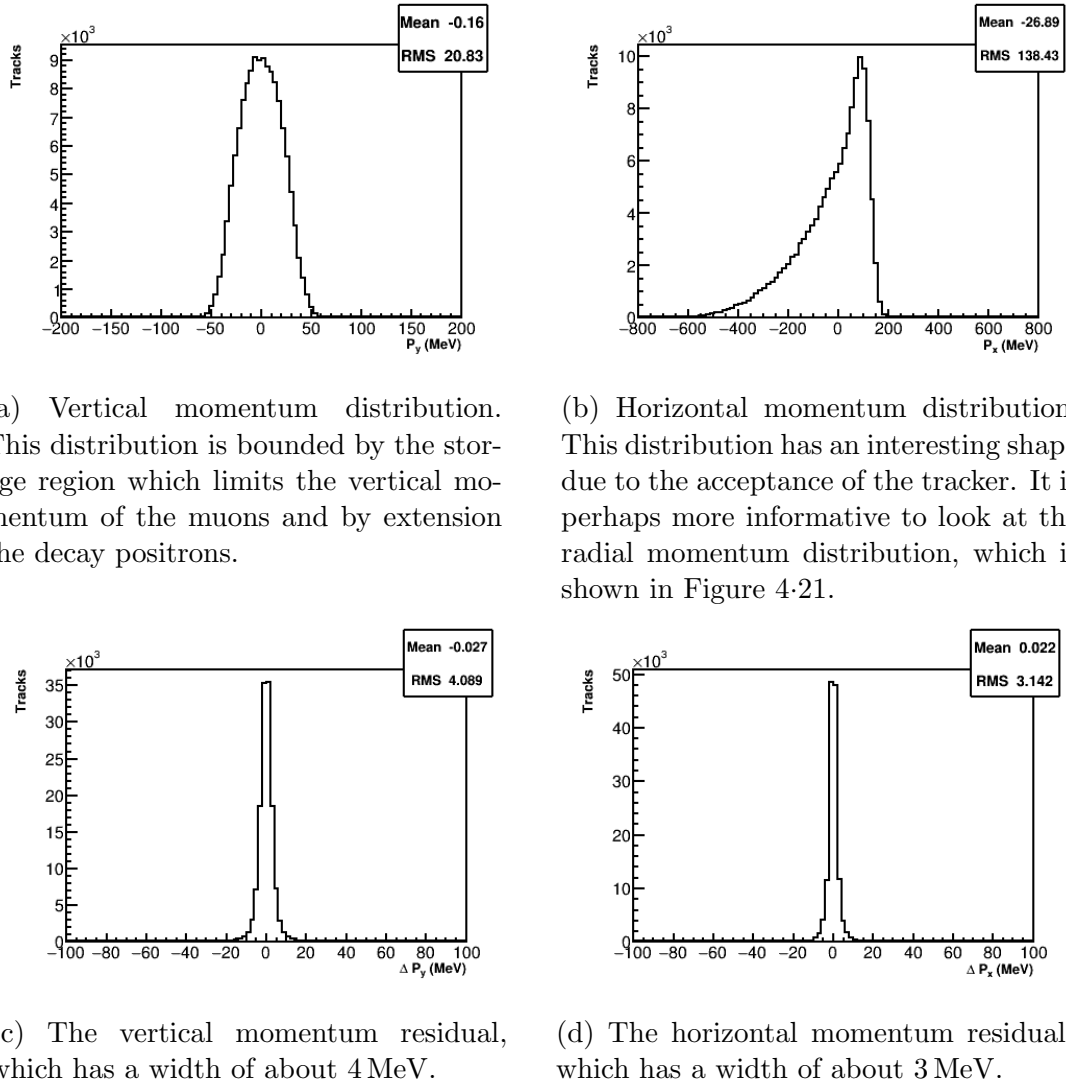


Figure 4.17: Shown are the fitted vertical and horizontal momentum components (top) for tracks at the entrance to the tracker, and their residuals to truth (bottom).



Figure 4.18: Shown are the fitted vertical and horizontal position components (top) for tracks at the entrance to the tracker, and their residuals to truth (bottom).

#### 4.2.6 Left-right ambiguity and fit modes

Before actual data can be fitted, the left-right ambiguity problem needs to be dealt with. Since straws only measure drift circles and not actual U or V positions, and since tracks are in general passing forwards through the detector, there is an ambiguity as to which side of the wire a particle passed for each hit. In general if even a single left-right choice for a hit is wrong then a track will fit poorly. There are a couple of different track fitting modes used to deal with this problem, which are detailed in Reference [70] and summarized here and in Reference [78].

##### `wireFit`

The first fit to any set of tracks in data is to do a fit to the wire centers, which requires no left-right information. The errors on the measured hits are set as the RMS of a uniform distribution with a width of a straw diameter. After a wire fit, an approximation of the best fit track is acquired which provides some left-right information. The number of fitting iterations is capped at three for the wire fit.

##### `mainfit`

The primary fit mode for analyzing data is called `mainFit`. After the wire fit is completed, the predicted track parameters at each measurement plane are compared to the locations of the wires for the straws that were hit. The left-right choices for each hit are set depending on which side of the wire the predicted track passed. The measured hit positions and errors are updated from the wire values to the angular-corrected DCA values based on the the left-right choices of each hit, and the fitting is repeated. At each iteration of the fitting, the left-right choices for each hit are updated based on where the previous predicted track parameters ended up. This is the fastest fit mode and with this method about 66% of tracks fit well. Since there is no shortage when it comes to statistics for positron tracks, this is acceptable.

### **fullSeqFit**

The secondary fit mode is called **fullSeqFit**. This fit mode does a better job of determining the left-right choices for the hits in a track, but is much slower than **mainFit**. Here is given a short summary, see Reference [70] for more technical details on all parts of this fitting mode.

After a wire fit, the geometry of the straw layers is used to resolve some of the left-right choices for a hit on a track. The left-right ambiguity is partially resolved through the shift in layers for each view as detailed in Section 3.3, where if a particle passes straight through both layers in a view it can be seen to go to the left of one wire and the right of the other. This implies that for curved tracks with certain angles through tracker modules, the left-right choices for some hits are known precisely [79]. For these hit planes the left-right choices are locked in and taken as known for the rest of the fitting.

For the remaining hits where the left-right choices are unknown, an approximate  $\chi^2$  is calculated for each combination of left-right choices,  $2^{N_{\text{unknown}}}$ . This  $\chi^2$  is calculated using the same formula as in the full fitting with the measured parameters set to the different left-right combinations, Equation 4.27, but using the Geane transport and error matrices calculated by the wire fit instead of from a fit to the left-right choice measured parameters. Calculating this  $\chi^2$  for each combination is slow, so this process is sped up by only checking the left-right combinations for the U or V hit layers at a time respectively,  $2^{N_{\text{U,unknown}}} + 2^{N_{\text{V,unknown}}} \ll 2^{N_{\text{unknown}}}$ . This  $\chi^2$  calculation allows for a measure of how good a left-right combination is to be determined without having to propagate every track in Geane for the full fitting. The tracks with the best combinations and smallest approximate  $\chi^2$ 's are then fit with the full Geane propagation and  $\chi^2$  minimization algorithm. Typically the best 10 to 15 combinations are fit, and the final track with the best  $\chi^2$  is taken as the true track. This gets the

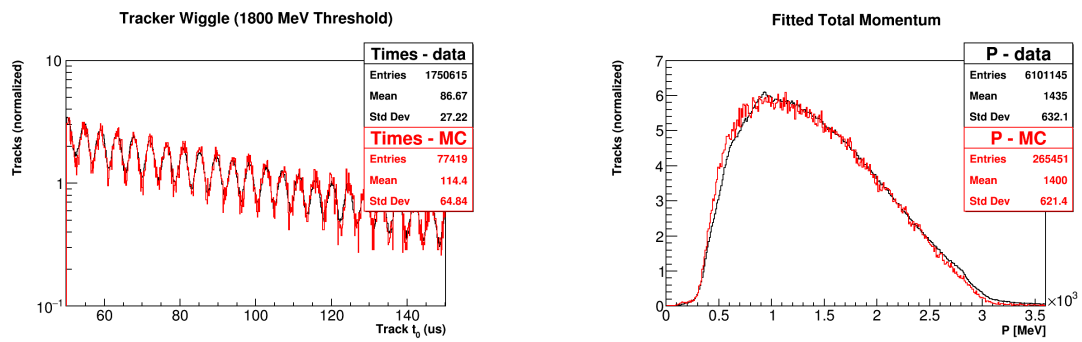
left-right choices for the fitted tracks right about 99% of the time with simulated data, but is very slow due to the combination checking and the Geane propagation for each of the best track left-right combinations. If the track fitting can be sped up significantly or a majority of the left-right choices constrained upstream somehow, then this fit mode would be more useful.

#### **4.2.7 Fits to tracks from data and comparison with Monte-Carlo**

Fits to data are done with `mainFit`. Due to imperfect left-right assignments and the use of real DCA and DCA error measurements, the tracks from data are naturally more messy. See Figure 4·19 for a plot of the goodness-of-fit for the tracks. While not all tracks are fit perfectly, enough of them are fit well in order to pass on the results to the extrapolation stage. Fitted tracks to Run 1 data are compared to results from Monte-Carlo. Track times and fitted total momenta are shown in Figure 4·20. Fitted track radial and vertical momentum and position distributions are shown in Figure 4·21. In general the results are very similar between the two. There are mismatches in the distributions because the idealized simulation did not reflect the real run conditions at the time of this track fitting analysis. As described in Section 2.8 and explored later in Section 4.4, the muon beam was imperfectly stored in the ring leading to the measured distributions here.



Figure 4.19: P value distribution for fitted tracks in data. A cut has been made at 1% to remove tracks which have entirely failed the fitting. The distribution can be seen to rise towards zero where tracks have been fit but imperfectly.



(a) Track times for tracks with energy greater than 1.8 GeV. The  $g - 2$  frequency can be seen in both the data and simulation.

(b) Fitted track total momentum, there is a very slight mismatch between data and Monte-Carlo.

Figure 4.20: Fitted track results in data (black) vs Monte-Carlo (red). The amount of entries in each are normalized to each other so that they can be compared. Shape differences between the two are due to a mismatch between simulation conditions and the real experiment, and not any problem with the track fitting.



Figure 4.21: Fitted track results in data (black) vs Monte-Carlo (red). The amount of entries in each are normalized to each other so that they can be compared. Shape differences between the two are due to a mismatch between simulation conditions and the real experiment, and not any problem with the track fitting.

### 4.3 Track extrapolation

The last stage of the track reconstruction is the track extrapolation. The extrapolation takes the fitted track results and either extrapolates them back to the storage region to the approximate position of the muon decay point, or forwards to the face of the calorimeter sitting right behind the tracker. The extrapolation stage utilizes a fourth order Runge-Kutta Nyström algorithm [61] which discretely steps a trajectory through the magnetic field in the full  $g - 2$  Geant4 simulation, similar in some respects to the error propagation. At each step of the extrapolation, the updated track position and covariance matrix are compared to physical volumes in the simulation to flag tracks which have been reconstructed as likely originating from outside the storage region [61, 80]. Because there is no fixed interaction point in the storage region, tracks are extrapolated backwards to the point of tangency where the radial momentum is equal to zero. Studies were done to verify that this approximation for the muon decay point was sufficient using Monte-Carlo, and it was found that a simple 1.1 mm correction to the radial decay position could be applied regardless of the momentum of the track [61]. The vertical extrapolated distribution was found to have no biases. (What about the azimuthal point? Mentioned a little bit in DocDB 8564 but do I really want to go into it?) A birds eye view for tracks extrapolated back into the storage ring is shown in Figure 4.22.

### 4.4 Muon beam measurements

All stages of the track reconstruction have ultimately lead to the goal of determining the characteristics of the muon beam. As described in Section 2.6, the muon beam is not a fixed entity. Where the muons live and how they move in the storage region ultimately affect the calculation of the E-field and pitch corrections, the weighting of the muon distribution with respect to the measured field, and the calorimeter preces-

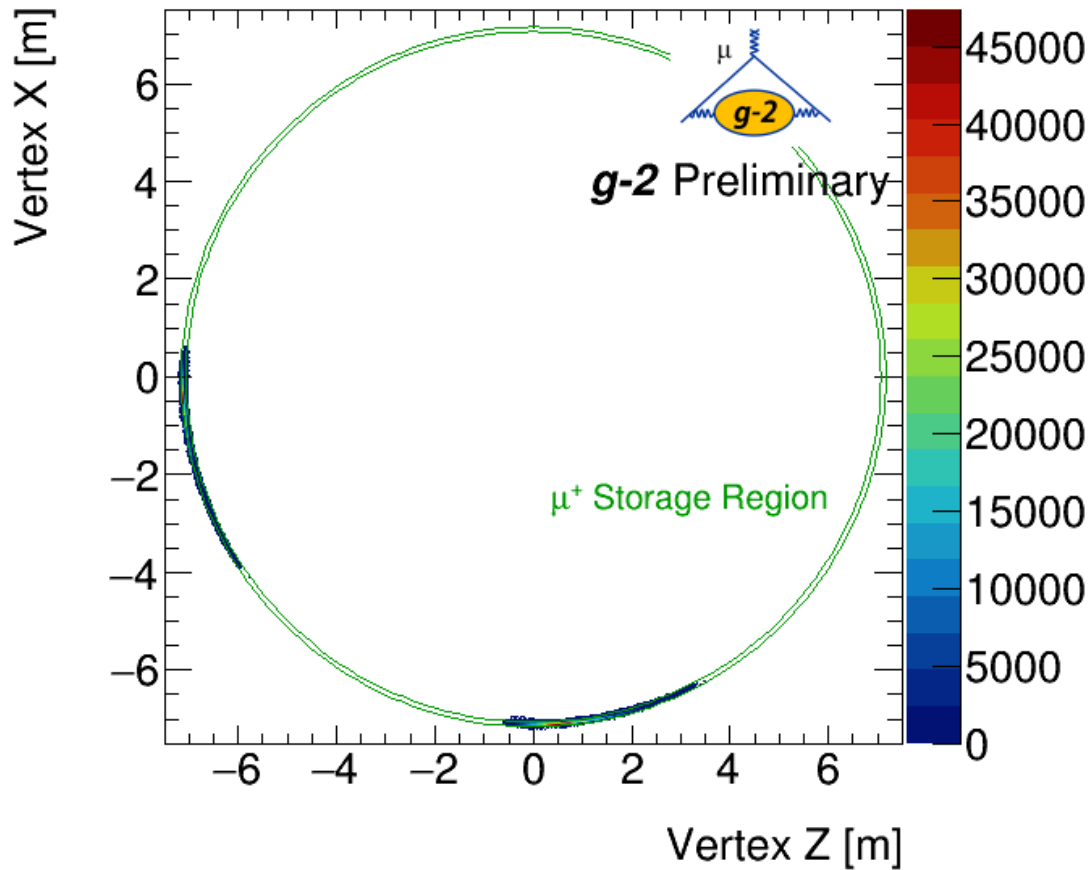


Figure 4.22: A birds eye view of the extrapolation results in the storage ring. The two distributions of extrapolated tracks can be seen at the left and bottom of the figure, where the tracker sits at the heads of the distributions. It can be seen that some tracks are extrapolated multiple meters back through the storage region. Plot courtesy of James Mott.

sion frequency analysis. Here are presented plots for the 60H dataset which describe the muon beam in the storage region, for those muons which decayed to positrons which then passed through the tracking detectors. There is still on-going work in regards to analyzing the acceptance differences between the tracker and calorimeter, in order to make sure that the correct muon beam dynamics are described in regards to those positrons which hit the calorimeters and are responsible for the measurement of  $\omega_a$ . Tracker-calorimeter matching studies will not be detailed here. A preliminary analysis is given in Reference [65].

The following cuts are applied to the track reconstruction [81, 82]:

- Non-failed track or vertex
- No volumes hit
- Number of tracking planes hit  $\geq 12$
- p value  $> 5\%$
- Vertical extrapolation uncertainty:  $0.5 < \sigma_y < 3.5$  mm
- Radial extrapolation uncertainty:  $0.5 < \sigma_r < 5$  mm
- Horizontal entrance into tracker:  $60 < X < 150$  mm
- Vertical entrance into tracker:  $-40 < Y < 40$  mm
- Drift time:  $0 < t_d < 70$  ns
- Track UV residuals  $< 500$   $\mu\text{m}$
- Fraction of missed planes  $< 30\%$
- $|\text{Number of U hits} - \text{number of V hits}| \leq 4$

These cuts remove failed or poorly fitted tracks, and cut out those tracks which end up in the tails of various quality checking distributions. By applying these cuts a clean sample of the extrapolated muon decay positions is extracted without biasing the results.

First, a radial slice of the extrapolated beam distribution is shown in Figure 4·23. As shown the beam is off-center due to kicker effects. The radial and vertical projections of this cross-section are shown in Figure 4·24. The vertical distribution is very similar to that from the track fitting results, while the radial distribution of the stored muons has a non-Gaussian shape due to the storage procedure of the muons. These two distributions in general appear wider than they actually are at a single point in time, because tracks of all times are included in these plots and the beam is moving in time. Figure 4·25 shows the radial and vertical distributions of the muon beam as a function of time in-fill, with the means plotted in Figure 4·26. Table 4.1 gives the measured values of the beam parameters corresponding to the various datasets. Because of the bad quad resistors, the beam was actually seen to start at a greater vertical position than the center of the storage ring, and slowly move downwards over the course of a fill. Similarly, the vertical width of the beam decreases slowly over the course of a fill. **Include plots for this or reference another document?**



Figure 4.23: Shown is a radial slice of the extrapolated muon distribution or beam spot. The beam is localized off center of the storage ring due to the kicker settings used, Section 2.8. Plot courtesy of James Mott.



(a) The radial position of 0 mm corresponds to the magic radius of 7.112 m. The radial distribution is peaked radial outward from the center.

(b) The vertical distribution looks closely centered in the storage region, which as a reminder has a width of 9 cm.

Figure 4.24: Shown are the muon beam radial (left) and vertical (right) distributions for all track times. Plots courtesy of James Mott.



(a) The radial distribution of the muons can be seen to both oscillate radially inward and outward as a function of time, and bunch and spread out as a function of time. This behavior is the CBO of the beam.

(b) The vertical distribution of the muons is relatively stable as a function of time, but there is an oscillation that can just barely be seen.

Figure 4.25: Shown are the muon beam radial (left) and vertical (right) distributions as a function of time in-fill for tracks in Station 12. In general the distributions for Station 18 are very similar. Plots courtesy of James Mott.



(a) The radial distribution mean oscillates at the CBO frequency. It can be seen to rise at early times in Station 12 due to the scraping procedure, and then slowly relax away once the scraping is turned off and the muons decay away.

(b) The vertical distribution mean oscillates at the vertical waist frequency, as described in Table 2.2. As shown for these early track times the beam is actually stored slightly higher than the center of the storage region.

Figure 4.26: Shown are the muon beam radial (left) and vertical (right) distribution means as a function of time in-fill for tracks in Station 12. In general the distributions for Station 18 are very similar. Plots courtesy of James Mott.

Run 1 Dataset Muon Beam Parameters					
Name	Radial Mean	Radial Mode	Radial Width	Vertical Mean	Vertical Width
60H	7.61	19.14	18.43	0.15	12.88
HighKick					
9d					
LowKick					
SuperLowKick					
Endgame					

Table 4.1: Table of muon beam widths and means. Both radial and vertical values are defined with respect to the center of the storage region. All values are in units of mm. **Numbers input from root file, not from E-field/pitch workshop values. Verify this table with James, make sure the parameters are associated with the plots and cuts I've listed and shown.** Might want to reduce the table if most dataset results are the same.



Figure 4.27: The CBO frequency as a function of time in fill for the 9d dataset, tracker station 12. This frequency change is due to the slowly changing quad voltages over each fill. Plotted is the difference between the cosine argument for the changing frequency and the value it asymptotes to at late times. The frequency fit model includes two exponentials, one with a longer time constant and one with a shorter time constant. Courtesy of James Mott.

The observed oscillation is the CBO as described before in Section 2.6.1. It can be seen that over a course of a fill, the CBO decays away, and there is a corresponding beam motion as a consequence. As described in Section 2.8, the CBO characteristics of the beam were found to be changing over the course of a fill. Using the tracking results shown here, the CBO frequency and amplitude can be characterized [83]. The CBO frequency as a function of time in fill is shown in Figure 4.27. The CBO amplitude as a function of time in fill is shown in Figure 4.28. Both of these characteristics will be folded into the precession frequency analysis as will be described later.



Figure 4.28: The CBO amplitude as a function of time in fill. The beginning of the data is not well understood, but after around  $50\text{ }\mu\text{s}$  the CBO amplitude falls away. Different envelopes for the amplitude are fit to the data with various degrees of success. Since most of the muons decay away early in the fill, it's the early fitted times that are most important, for which even the simple exponential in red is sufficient. The value for  $T/2\pi$  in the blue curve is approximately  $114.5\text{ }\mu\text{s}$ . Courtesy of James Mott.

## Chapter 5

# $\omega_a$ Measurement

The measurement of  $\omega_a$  is determined by counting the number of detected positrons in the calorimeters above some energy threshold, as described in Section 2.1. Doing so results in a histogram of counts which is modulated by  $\omega_a$ , Figure 2·4. Fitting for the frequency allows  $\omega_a$  to be extracted. The  $\omega_a$  measurement therefore consists of the steps needed to construct the histogram of counts, the fitting of that histogram, and any systematic studies done in the analysis.

### 5.1 Reconstruction of decay positron hits

The calorimeters measure hit times and energies of impacting particles, where these hit times and energies are determined from the raw SiPM signals and a reconstruction procedure. In E989 there are two overall separate reconstruction algorithms, `ReconWest` and `ReconEast`, both written in the *art* framework similar to the tracking reconstruction. Each of these reconstruction algorithms is modularized, and the steps of the reconstruction process can be switched in and out at will. Using separate reconstruction methods gives confidence in any final results by removing single points of failure. The reconstruction method used in this analysis is `ReconWest`. A summary of its details will be presented here. A more thorough description is detailed by A. Fienberg [84].

The raw data are digitized waveforms, which are voltage versus time traces output from each SiPM for each calorimeter crystal hit. Due to the incredible amount of

data coming in with the high muon fill rate, only those pulses which exceed some threshold are saved to disk. An online processing system checks the traces against this pre-configured threshold by passing all of the data through a GPU farm [85]. If any trace is found above threshold, then the data is saved from every SiPM in every calorimeter, for a time range around the over-threshold trace. This time range is called a time island, similar to that in the tracking reconstruction, and typically has a width of 40 ns [84].

The traces are then fit with templates in order to extract the area and peak times of any present pulses. Each SiPM has its own templates, one for positrons and one for laser pulses. These templates are extracted from data, where each template is determined by collecting many single pulse traces from a SiPM, normalizing by pulse area, aligning in time, and averaging them. These templates were checked against many systematic effects in order to make sure that the constructed templates did not bias the energy or time measurements, such as hit angle, energy (pulse size), position, and rate, as well as aging effects [58, 84]. Each trace is fit using a  $\chi^2$  minimization algorithm with the corresponding SiPM templates in order to determine the time and energy of the hit. In order to fit for multiple pulses in a single time island, the fitting procedure first fits with a single template, and then checks the residuals for any remaining peaks. If peaks exist above some threshold, then the fitting is repeated until all pulses have been fit. The time measurement performance in the pulse finding was found to be unaffected by the number of pulses in a time island, and there is 100% pileup separation at 5 ns [84]. See Figure 5.1 for a typical single template fit to a SiPM trace.

Once a pulse has been fit with a template, the pulse area needs to be converted to real energy units using an energy calibration procedure. A couple of different techniques exist that can be used, including a method that counts photo-statistics



Figure 5.1: A template fit in purple to a SiPM trace delineated by the black points which is in units of ADC counts. Plot courtesy of Aaron Fienberg.

seen in the SiPMs [84]. The default method used is a comparison of lost muon energy signatures in the calorimeters. As described in Reference [**lostmuons**], muons lost from the storage ring can spiral inward and hit consecutive calorimeters with a specific time separation between calorimeter hits. These lost muons are minimum-ionizing particles, and thus leave a very distinct energy signature in the crystals, see Section ???. Selecting on the time signature allows hits corresponding to lost muons to be isolated, and the energy signature can be used to determine the appropriate conversions from area to energy<sup>1</sup>.

The energy calibration for positron hits as compared to lost muon hits then needs to be determined. Again there are a couple of different techniques, including a comparison of endpoint energies for high energy positrons which tail off at the magic momentum of 3.094 GeV, and comparison with simulation. The default technique is to calibrate the energies such that the optimal energy threshold for the  $\omega_a$  analysis is near 1.7 GeV [84]. Ultimately the energy calibration doesn't matter too much because it is not the energy units that really matter. What really matters is the number of positrons above some energy threshold, where that threshold can be optimized em-

---

<sup>1</sup>Different channels can also be equalized based on the energy signatures.

pirically. In fact, the entire  $\omega_a$  analysis could be done without even considering the energy of the incident positrons, and only considering the area of the SiPM pulses<sup>2</sup>.

Each pulse fit now has an associated energy and time. Because the measurement of  $\omega_a$  depends heavily on the time reconstruction since the analysis is a frequency extraction, pulse times need to be corrected for various effects in order to reach the precision goal. The fitted times for each pulse need to be aligned on a fill-by-fill basis relative to the injection time of the beam, corrected for any channel differences due to differing pulse shapes or fiber lengths, and corrected for any calorimeter time misalignments due to the use of different laser system components. The fill-by-fill alignment is corrected for using the T0 detector as described in Section 3.1.1. The channel differences are corrected by aligning calorimeter channels in time using signals from islands with large simultaneous pulses in neighboring crystals. Calorimeters are time aligned using lost muon coincident events as described before. Once the times of the pulse fits or crystal hits have been determined, the energies can be corrected appropriately for gain effects measured by the laser system. As described in Section 3.2.3, the laser calibration system corrects for in-fill, out-of-fill, and SDTP effects [86]. Figure 5.2 shows an in-fill gain function fit to data for a single calorimeter. Systematic effects for corrected gain effects are studied in Section 5.5.2.

The last part of the calorimeter reconstruction is the clustering. Clustering is the stage which takes the individual template fit results from separate crystals, and turns them into the times, energies, and positions of decay positron impacts. For a time island with a single positron impact, the procedure is straightforward. The energy for the positron hit cluster is the sum of the individual hit crystal energies. The time for the cluster is taken as the time of the maximum energy hit in the island. This works because most of the deposited energy from a hit is localized to a single crystal. The

---

<sup>2</sup>This statement ignores the effects of pileup which must be accounted for, and applies for a threshold style analysis, and not for other analysis methods which depend on the energy of the pulses.



Figure 5.2: In-fill gain function fit for a single calorimeter crystal (top) and fit residuals (bottom). Each crystal has its own in-fill and SDTP gain function parameters. Plot courtesy of Matthias Smith.

position of the cluster is determined with a logarithmic weighting function between crystal hits, which for a 2 GeV positron in the E989 calorimeters results in a resolution of 2 mm [84]. See Figure 5.3 for a single calorimeter cluster from a positron hit in the calorimeter. For a time island with multiple positron impacts, the individual crystal hits are separated in time, where the time partitioning separates hits that are 2.5 ns apart, and the clustering proceeds as before. For hits which are within this time window, a pileup event has occurred. If the pileup event happens within the same crystal, then the multiple hits are measured as a single hit, and this needs to be corrected for using a pileup subtraction technique, as described in Section 5.2.1. For hits that occur in separate crystals, the pileup can be resolved using the spatial separation of the calorimeters. This is an ongoing area of work, and one technique is described in Reference [84]. For this analysis the spatial separation was turned off, which simplifies the analysis somewhat. This increases the amount of pileup seen in the data, which then needs to be handled by the pileup subtraction technique. For the precision of the Run 1 analysis result, this was found to be acceptable.

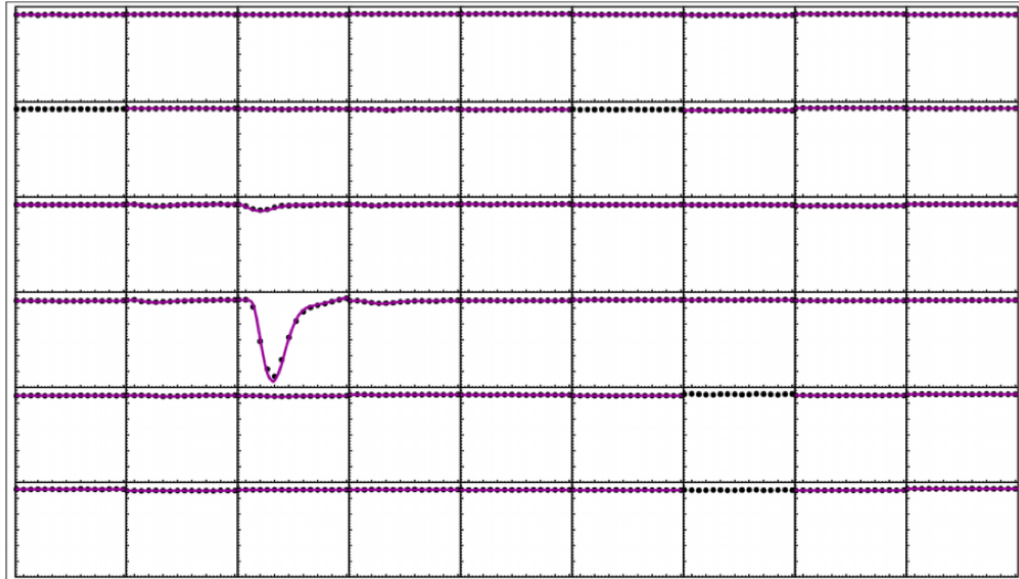


Figure 5.3: A single positron hit in the calorimeter, which resulted in a reconstructed calorimeter cluster. Each box is a crystal in the calorimeter, where the contained trace is the SiPM output fit with a template. The positron hit the crystal three from the left and three from the bottom, where it deposited most of its energy. Some of the energy was deposited in the neighboring crystals. Plot courtesy of Aaron Fienberg.

Time Spectra Parameters	
Parameter	Value
Energy threshold ( $E_{th}$ )	1700 MeV
Bin width ( $T_c$ )	149.2 ns
Artifical dead time (ADT)	5 ns
Shadow dead time (SDT)	5 ns
Shadow gap time (SGT)	10 ns
Pileup energy scaling (C)	1
$g - 2$ period ( $T_a$ ) in Ratio Method	4.365 411 $\mu$ s
Muon lifetime ( $\tau_\mu$ ) in Ratio Method	64.44 $\mu$ s

Table 5.1: Parameters used in the construction of  $\omega_a$  time spectra. **fill this table out more once I've gone through the various parts**

## 5.2 Construction of positron hit energy and time spectra

Once the reconstruction has processed all calorimeter hits into clusters, the energy and time spectra histograms are made. At the very last stage of the reconstruction procedure, an *art* module takes the produced clusters and puts them into `ROOT TTree` formats, where individual data members include the energies, times, calorimeter numbers, etc. of the individual clusters. There is of order 20,000–140,000 cluster data files per dataset, which are combined down to order 200–1,400 `ROOT TTree` files. These `ROOT TTrees` are then passed through a `ROOT` macro to produce `ROOT` files with the histograms defined by the `TH1F` class, one `ROOT` histogram file per tree file.

It should be noted that some of the parameter choices for the constructed histograms were informed by analysis results. All analysis parameters were chosen to be identical between the distinct analyzed datasets, in order to simplify both the comparison and combination of different dataset results. This section describes the justification for the different histogram parameters chosen. A table of the histogram parameters is shown in Table 5.1.

Energy and time histograms are made for each individual calorimeter. These

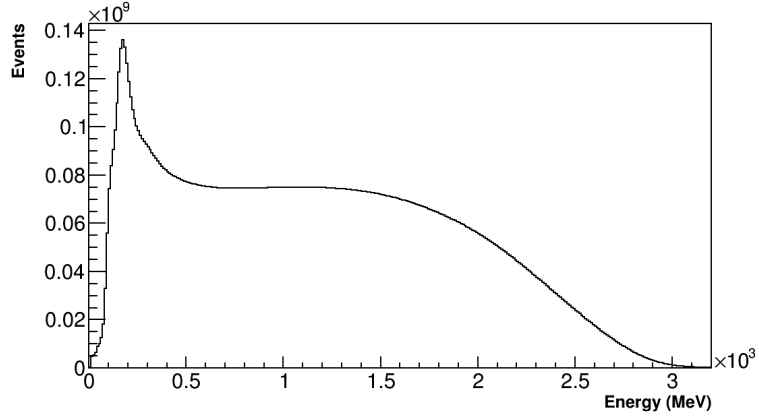


Figure 5.4: Energy spectrum for hits in all calorimeters for the Endgame dataset on a linear scale. The peak at about 170 MeV corresponds to lost muons.

are summed together to form histograms of all hit times and energies. Figure 5.4 shows a sample energy spectrum for the Endgame dataset. An energy threshold is applied to the clusters before filling the time histograms. As described at the end of Section 2.1, the optimal energy threshold is where the quantity  $NA^2$  reaches the maximum, at least in the case of a five parameter fit<sup>3</sup>. By scanning over the choice of energy threshold and fitting the resulting time spectra with Equation 2.13, the optimal energy threshold can be determined as seen in Figure 5.5. The optimal choice of energy threshold was determined to be 1700 MeV, in accordance with the cluster reconstruction energy calibration.

The optimal bin width for the time histograms was determined to be 149.2 ns, the average of the cyclotron periods determined from a fast rotation analysis to the data [fastrotationsomething]. As described in Section 2.6.2, this bin width combined with a time randomization on each cluster over a range of  $\pm T_c/2 = 149.2 \text{ ns}/2$  serves

---

<sup>3</sup>Using the final fit function and looking at the error directly on the fitted  $\omega_a$  frequency, a slightly better estimate can be found.

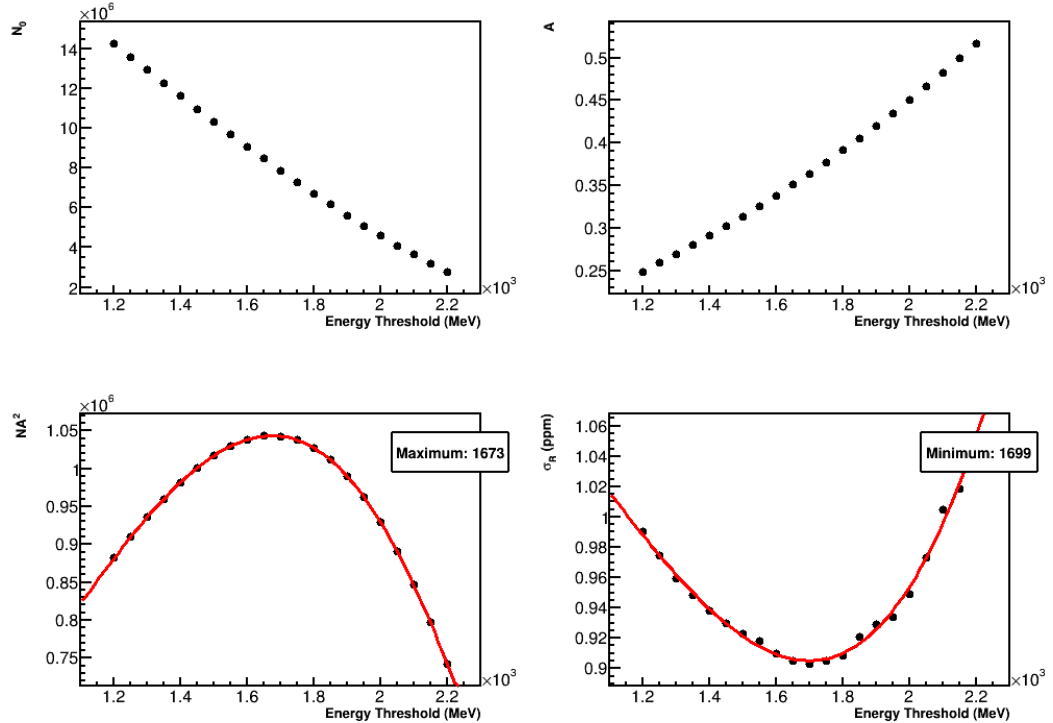


Figure 5.5: The optimal energy threshold can be determined from the  $NA^2$  quantity as described in Section 2.1 from five parameter fits to the data (bottom-left) or from the calculated error with the final fit function (bottom-right). Fitted  $N$  and  $A$  parameters are also shown (top) which satisfy Equations 2.14 and 2.15. The maximum and minimum are determined using seven parameter polynomial fits to the relevant quantities. The optimal threshold varies slightly per calorimeter and per dataset. Since the region of the minimum is relatively flat, a single energy threshold of 1700 MeV was chosen. Data from the 9d dataset.

to eliminate the fast rotation signal in the data<sup>4</sup>. This randomization is done using ROOT’s `TRandom3` class. As will be described in Section 5.3.2, the cluster times are also randomized by  $\pm T_{VW}/2$ , where  $T_{VW}$  is determined per dataset. This is done in order to remove the effects of the VW in the data. **Should I put the actual numbers here? Need to look them up again.** The default random seed for each histogram ROOT file is the hash of the input file name using C++’s standard hash class. Histograms are defined with a time range of 0–699.8972  $\mu\text{s}$  (the closest integer multiple of the bin width to 700  $\mu\text{s}$ ), corresponding to 4691 bins. Clusters with times less than 25  $\mu\text{s}$  or greater than 660  $\mu\text{s}$  are dropped, corresponding to 4256 bins containing data.

### 5.2.1 Pileup subtraction

As described in Section 3.2, there will be a certain amount of pileup in the detectors. Pileup again is the term for when multiple particles hit a calorimeter within the dead time of the detector such that they are registered as a single hit or cluster. The measured energy and time spectra for all observed clusters will include this pileup background. For the energy threshold time histogram, the number of counts will be wrong for cases where two below-threshold particles are registered as a single cluster above threshold, and where two above-energy threshold particles are registered as a single cluster. In the former, an extra count is added into the histogram, and in the latter a count is missed. The case where two lower energy positrons are registered as a single higher energy cluster will have a different  $g - 2$  phase than an actual single cluster at the same energy. This is because the lower energy positrons on average decay from muons which have travelled further around the ring, due to acceptance effects. These muons which have travelled further around the ring have spent more

---

<sup>4</sup>Some analyzers randomize all times in a single fill by half the cyclotron period as opposed to each individual pulse.

time in the magnetic field, and thus their spins have precessed more. See Figure 5.6. Clusters which originate from pileup events therefore have a different  $g - 2$  phase than non-pileup events.

If pileup was a constant effect, then the phase of the time histogram would be shifted by some constant amount, and the extracted  $\omega_a$  frequency would be unaffected. However, the rate of pileup in the detectors changes over the time of a fill, as muons decay away. The rate of double pileup events in the detectors, where the word double indicates cases where two hits are registered as a single cluster, will go approximately as half the rate of single hit events<sup>5</sup>, and similarly for triple and higher orders of the pileup effect. Because the rate of hits in the detectors oscillates at the  $g - 2$  frequency, pileup will increase and decrease accordingly leading to oscillations in the pileup time spectra at  $\omega_a$  and  $2\omega_a$ . The lifetime of the overall pileup effect is approximately half the lifetime at which clusters are registered in the detectors, at  $\tau_\mu$ , since double pileup is the dominant contribution. In order to extract the correct  $\omega_a$  frequency, the pileup effect thus needs to be included in the fit function or subtracted out of the data. The former is challenging due to the non-linear nature of the dead time of the detectors, and would in the end include another phase in the argument of the cosine term in the fit function, thus worsening the statistical precision of the extracted  $\omega_a$  frequency. All analyzers thus construct an approximation of the pileup effect and subtract it from the data before fitting.

There are various methods to construct pileup spectra which are then subtracted off the main time and energy spectra. The method used in this analysis is called the ‘asymmetric shadow method’, originally developed in E821 [87]. This method statistically constructs an approximation for the pileup from the data by assuming that the probability of observing a pileup pulse is the same as the probability that two pulses will be offset by some small amount of time, such as 10 ns. The method works

---

<sup>5</sup>It is not exactly half when including the non-linear dead time of the detectors

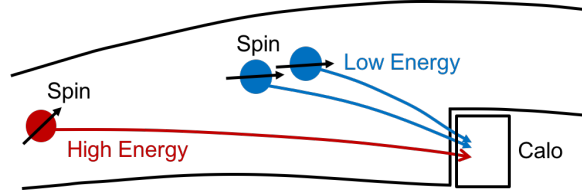


Figure 5.6: Pileup example, where two low energy positrons are registered as a single high energy positron. The black arrows indicate the (exaggerated) direction of the muon spins at the time of decay. Because of acceptance effects the lower energy decay positrons typically come from muons which have traveled further around the ring, and thus the muon spins have precessed more in the magnetic field, leading to a different measured  $g - 2$  phase for pileup events.

by looking in time windows after trigger pulses to see if a ‘shadow’ pulse exists. If such a pulse exists, then a shadow doublet is created, see Figure 5.7. The width of the time window, and the time offset from the trigger pulse to the window, are called the shadow dead time (SDT) and shadow gap time (SGT) respectively. The times and energies of the constructed pileup doublets are taken as

$$E_{\text{doublet}} = C \cdot (E_1 + E_2), \quad (5.1)$$

$$t_{\text{doublet}} = \frac{t_1 \cdot E_1 + (t_2 - SGT) \cdot E_2}{E_1 + E_2}, \quad (5.2)$$

where the energy of the doublet is the sum of the two singlet pulses  $E_{1,2}$  times some calibration constant  $C$ , with a default value of 1, and the time of the doublet is the energy-weighted time of the two singlets  $t_{1,2}$ . The procedure for constructing the pileup spectra is as follows:

- Put each hit into a vector corresponding to a specific fill and a specific calorimeter
- Time order the hits
- Loop through the hits, for each hit look within a window of width SDT a time

SGT later to see if a shadow pulse exists

- If a shadow pulse exists, construct a shadow doublet with energies and times as defined in Equations 5.1 and 5.2
- Randomize  $t_{\text{doublet}}$  over the range  $\pm T_c/2$  (to remove fast rotation as before, Section 2.6.2)
- Per calorimeter, construct pileup energy and time spectra as  $P = D - S$ , where  $D$  is the sum of doublets and  $S$  is the sum of singlets used in the construction of the doublets, with the times of the singlets set as  $t_{\text{doublet}}$ ; when constructing the pileup time spectra, only include those doublets and singlets above the energy threshold

Thus pileup energy and time spectra are constructed for each calorimeter, which can then be subtracted off the calorimeter cluster energy and time histograms. When combining the data, the individual pileup histograms are simply added together before subtraction off the calorimeter sum histograms.

In order to produce an estimate of the pileup spectra which best matches the data, an artificial dead time (ADT) is applied to the data before time randomization. This is done because the true dead time of the detectors depends on the energies and spatial separation of the incoming hits. While this is a small effect, by applying an artificial deadtime and matching the shadow window time, the pileup estimation is improved slightly. The construction of the artificial pileup is handled in the same way as the construction of the shadow pileup, with SGT set to 0 ns. The constructed artificial doublets replace the singlets in the data. The value for the ADT and SDT is set at 5 ns, the time threshold at which pileup is 100% resolved.

The value of the SGT is simply set to twice the SDT, in order to push the shadow window out to times well beyond the dead time of any pileup events, but not so far



Figure 5·7: The shadow pileup method looks for shadow clusters within a time window SDT, a small time away (SGT) from trigger clusters. If a shadow cluster is found, an artificial doublet is formed and included in the pileup spectra if it exceeds the chosen energy threshold.

that an appreciable fraction of muons have decayed. The value of the doublet energy scaling factor  $C$  is set to 1, which is a fine approximation as the spatial separation in the reconstruction is turned off<sup>6</sup>. The values for each pileup parameter is shown in Table 5.1. See Section 5.5.1 for systematic studies on the effect on  $\omega_a$  due to these chosen parameters.

The pileup energy spectra as compared to the cluster energy spectra is shown in Figure 5·8. In general, the two lobes starting at approximately 3 GeV and 6 GeV consist of double and triple pileup events respectively<sup>7</sup>. It can be seen that the shadow method of pileup construction produces a pileup energy spectra which is a decent approximation of the cluster energies above the maximum energy that a single decay positron would have at (3.094 GeV)+detector resolution, for cases of double and even

<sup>6</sup>With the spatial separation turned off, ‘pileup’ events can occur in crystals that are easily separated by eye. While this increases the level of pileup seen in the data, the pileup approximation method also does not consider the spatial separation, and thus handles the level of pileup accordingly.

<sup>7</sup>All orders of pileup fill out the whole energy range, but certain areas consist of mostly one or the other.

triple pileup. The shape difference arises from two factors: First, the shadow method is only written to construct doublets, and does not consider cases of triple or higher orders of pileup. Second, the real pileup in the data contaminates the construction of the shadow pileup spectra, such that a shadow doublet can be constructed from real pileup pulses. While this alleviates the triplet problem slightly, it means that the doublet pileup spectrum is slightly wrong. The corrected energy spectra (cluster energies minus pileup energies), can be seen in Figure 5.9. The shape mismatch is even more apparent as the corrected energy spectrum is high for energies above the expected tail of the true energy distribution, and then goes negative before tailing off to zero.

In order to produce a slightly better estimate of the pileup, a multiplier can be applied to the pileup energy and time spectra. By taking the ratio of cluster energies over pileup energies and fitting the region where the energies are dominated by real pileup doublets, a correction factor of approximately 3% is found, as shown in Figure 5.10. Similarly, the cluster times can be examined for cluster energies over 3500 MeV, where the clusters consist purely of pileup pulses, Figure 5.11. By taking the ratio of the pileup corrected times over all times, the level of residual pileup can be determined. Just as in the ratio of the energies, an approximately 3% factor is found. When applying this multiplier, the cluster times above 3.5 GeV can be seen to be eliminated as in Figure 5.11. As will be shown in Section 5.5.1, the scale of this multiplier is well within  $1\sigma$  of the pileup multiplier error. The final pileup time spectrum for those pileup pulses above energy threshold is shown in Figure 5.12.

It has been determined that regardless of any residual shape mismatch in the cluster times below 3.5 GeV, the systematic error on the extracted  $\omega_a$  frequency due to the pileup is within the target uncertainty for the level of statistics in the Run 1 dataset, Section 5.5.1. For analyses past Run 1 where the error budget is reduced, it

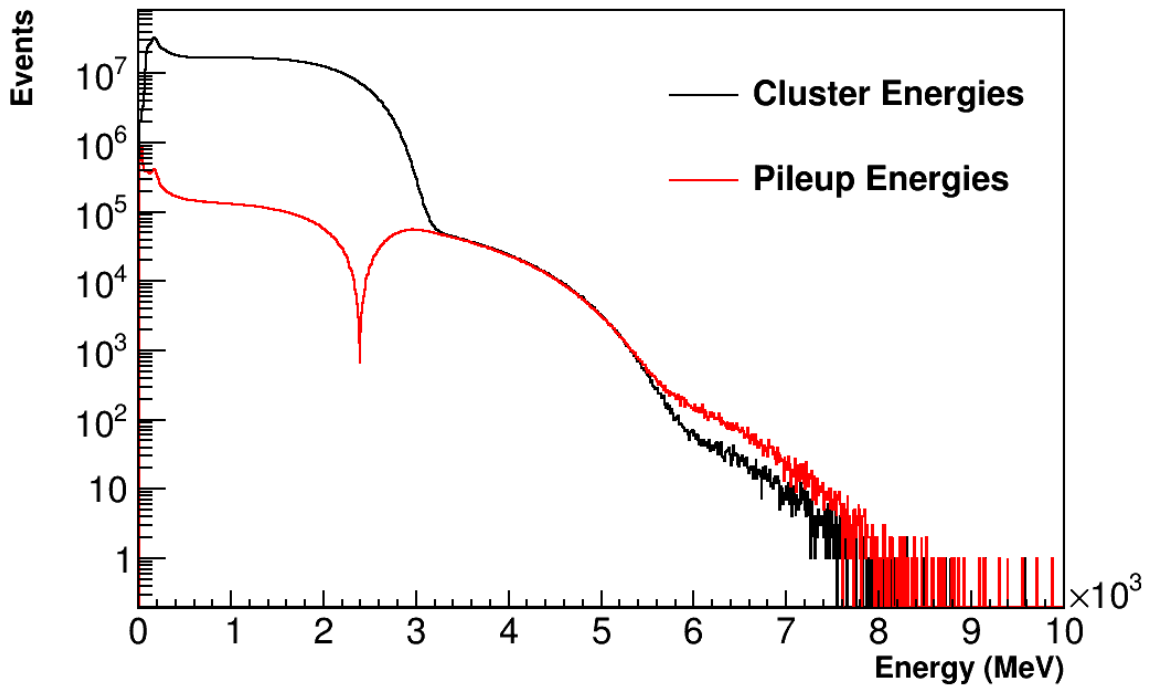
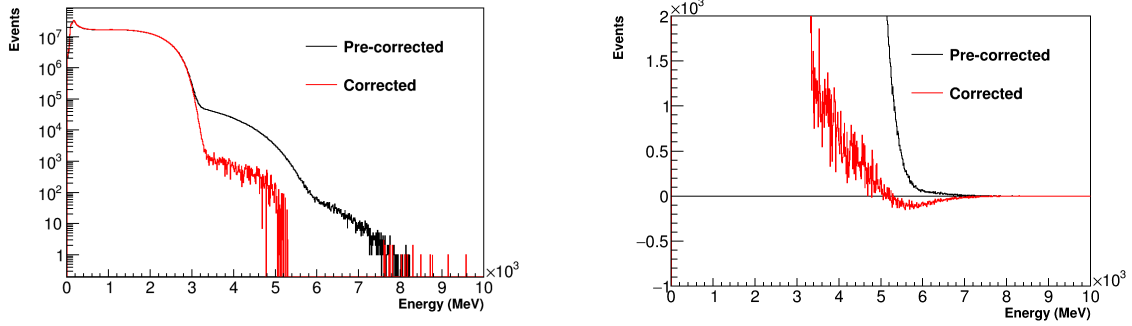


Figure 5.8: Cluster energies in black are plotted vs pileup energies in red, for all calorimeters added together, plotted on a log scale. At energies below about 2.4 GeV the pileup energy spectrum goes negative. In this plot the absolute value of the pileup energies is plotted, and a spike at about 2.4 GeV can be seen as a consequence of this. The shapes do not match perfectly for the constructed pileup spectra, which can be seen at high energies. It should be noted that for energies above 3.094 GeV there is still a shape mis-match even though the red and black curves overlap due to the plotting scale. Data from the 60h dataset.



(a) Log scale - the corrected energy spectrum goes negative around 5 GeV.

(b) Linear scale - zoomed in to show the shape.

Figure 5.9: Plots for the pre-corrected and corrected energy spectra are shown, all calorimeters added together. Because the triplets and contamination are not accounted for, the corrected energy spectrum does not lie exactly along zero above the energy response of the detectors. Data from the 60h dataset.

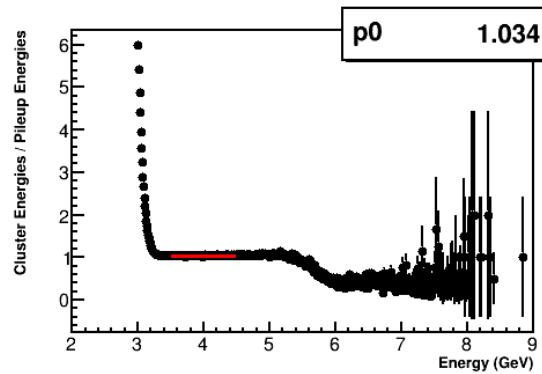


Figure 5.10: Cluster energies over pileup energies. A region from 3500–4500 MeV is fit to a straight line, where the doublets dominate the energy distribution. Data from the 9d dataset.

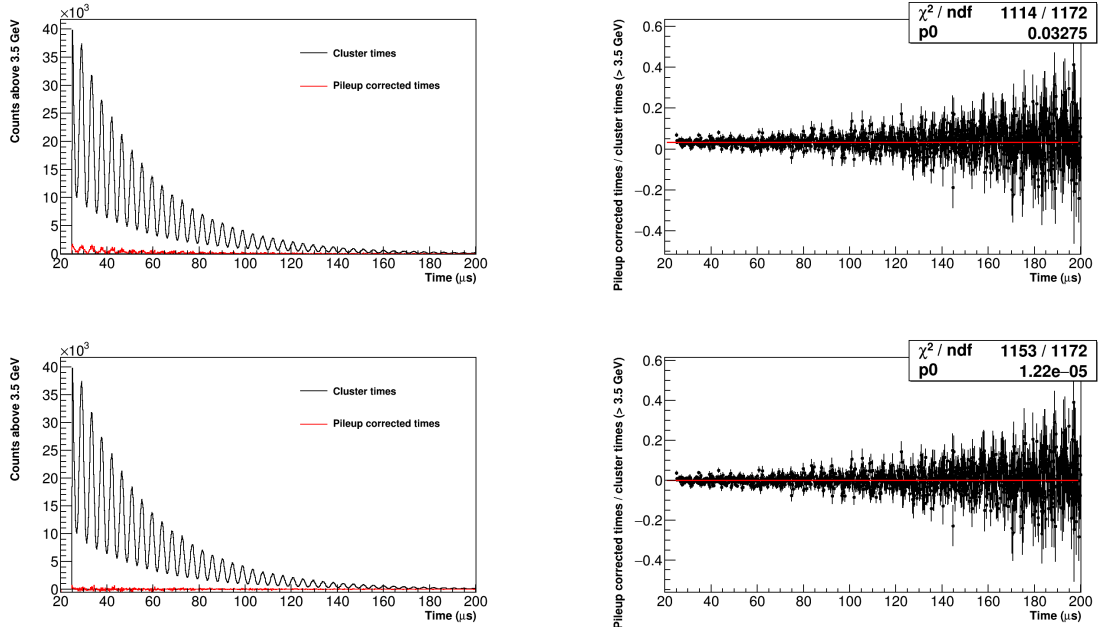


Figure 5.11: Cluster times and pileup corrected times for counts above 3.5 GeV (left) and their ratio (right). The top two plots are used to determine the approximate level of residual pileup left in the data, coming out to about 3%. The bottom two plots show the application of that factor and the resulting removal of the remaining pileup. Data from the 9d dataset.

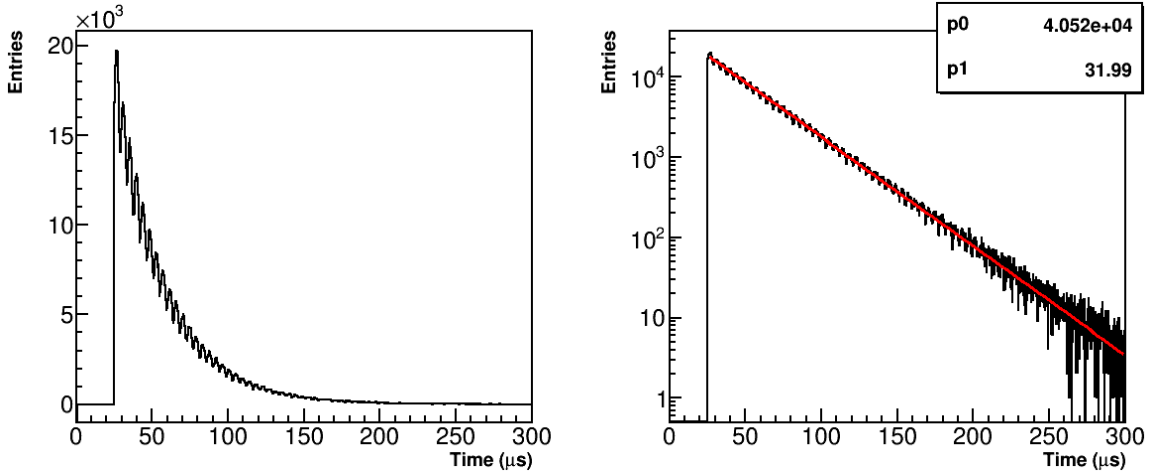


Figure 5.12: Plotted is constructed pileup time spectrum on a linear (left) and log (right) scale. The histogram on the right is fit to a simple two parameter exponential to get an idea of the lifetime of the pileup, calculated here as  $31.99 \mu s$ , which is close to half of the muon lifetime at about  $64.44 \mu s$ . Data from the 60h dataset.

may be necessary to improve the shadow method to account for triplets and the contamination. Finally, since the pileup is statistically constructed and then subtracted from the data, the errors on the final time histogram are no longer Gaussian. The proper calculation of the errors is detailed in Appendix C.

### 5.2.2 Ratio Method

The method used in this analysis to extract  $\omega_a$  is called the “Ratio Method,” or sometimes “R-Method.” It is a technique that modifies the data in such a way that the exponential decay in the time histogram is removed, and slow effects are reduced. It was used successfully in the E821 experiment [88, 89, 90]. A full derivation of the equations in the method is given in Appendix B; here is given a short summary. Figure 5.13 provides a pictorial representation of how the method works.

The method works by dividing the data into four separate datasets, one with the times of all clusters shifted up by half a  $g - 2$  period,  $+T_a/2$ , one with cluster times

shifted down by half a  $g - 2$  period,  $-T_a/2$ , and two unchanged. Assuming the data is described by the five parameter function described in Section 2.1 and shown in Figure 5.13a,

$$N_d(t, E_{th}) = N_0(E_{th}) \cdot e^{-t/\gamma\tau_\mu} \cdot [1 + A(E_{th}) \cos(\omega_a t + \phi(E_{th}))], \quad (5.3)$$

and that the data is equally split into four subsets, then the new four datasets are given as<sup>8</sup>:

$$\begin{aligned} u_+(t) &= \frac{1}{4}N_5(t + T/2) \\ u_-(t) &= \frac{1}{4}N_5(t - T/2) \\ v_1(t) &= \frac{1}{4}N_5(t) \\ v_2(t) &= \frac{1}{4}N_5(t) \end{aligned} \quad (5.4)$$

In order to time shift the data as such,  $T_a$  needs to be known a priori to high precision. The value used is taken from the E821 result, and its value is taken as  $1/f_a$ , where  $f_a$  is 0.229 073 5 MHz:

$$T_a \approx 4.365\,411\,\mu\text{s} \quad (5.5)$$

This value for  $f_a$  was determined by averaging column 2 of Table XV of the E821 Final Report [29], which consists of the  $f_a$  results for the different run periods in that experiment. A systematic error on the choice of this parameter is calculated in Section 5.5.5.

---

<sup>8</sup>When handling the pileup in the ratio method, the pileup time spectra are split into four datasets and time-shifted in the same way as the cluster hit times. Associated doublets and singlets are kept together in the same individual dataset, and the four pileup datasets are subtracted off their respective ratio datasets before forming the ratio.

The datasets are then combined as

$$\begin{aligned} U(t) &= u_+(t) + u_-(t), \\ V(t) &= v_1(t) + v_2(t), \end{aligned} \tag{5.6}$$

both of which are shown in Figure 5.13b. It is immediately apparent that the  $U(t)$  data are shifted 180° out of phase from the  $V(t)$  data. The ratio is then defined as<sup>9</sup>

$$R(t) = \frac{V(t) - U(t)}{V(t) + U(t)} \tag{5.7}$$

where the numerator and denominator are plotted in Figures 5.13c and 5.13d respectively. The numerator is an exponentially decaying cosine, while the denominator is a simple exponential, both of which can be seen as originating from the difference and sum of the  $U(t)$  and  $V(t)$  data respectively. The resulting ratio spectrum can be seen in Figure 5.13e, where the exponential has been eliminated. The fit function is then reduced from five parameters down to three:

$$R(t) \approx A \cos(\omega_a t) - C, \tag{5.8}$$

where

$$C = \frac{1}{16} \left( \frac{T}{\tau} \right)^2 \approx 2.87 * 10^{-4}, \tag{5.9}$$

and these functions have been determined from the time-shifted five parameter function plugged into the  $U(t)$  and  $V(t)$  variables. In addition to the exponential being eliminated, any slow terms in the data get time-shifted and divided as well, such that the amplitude of said slow effects are reduced. For faster effects, the degree of cancellation of the effect is dependent on the frequency. Effects at frequencies which

---

<sup>9</sup>The ratio can also be defined with  $U(t) - V(t)$  in the numerator, however then the phase of the ratio spectrum is shifted 180° from the original  $N_5(t)$  spectrum.

are an odd multiple of  $\omega_a$  are preserved while effects at an even multiple of  $\omega_a$  are completely cancelled out. An example is shown in Figure 5.14. While this makes fitting the data easier in some cases, in others it is a downside that effects which still need to be included in the fit function now have their amplitudes reduced, making them harder to fit.

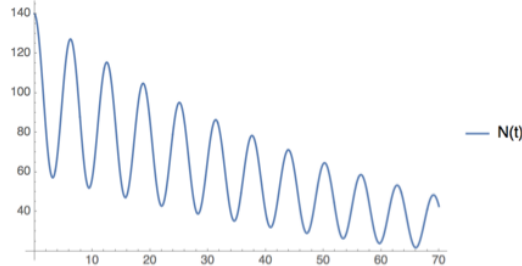
In order to eliminate the constant  $C$  at the end of Equation 5.8, a different weighting scheme can be used as described in Reference [37]:

$$\begin{aligned} u_+(t) &= \frac{e^{T/2\tau}}{2 + e^{T/2\tau} + e^{-T/2\tau}} N_5(t + T/2) \\ u_-(t) &= \frac{e^{-T/2\tau}}{2 + e^{T/2\tau} + e^{-T/2\tau}} N_5(t - T/2) \\ v_1(t) &= \frac{1}{2 + e^{T/2\tau} + e^{-T/2\tau}} N_5(t) \\ v_2(t) &= \frac{1}{2 + e^{T/2\tau} + e^{-T/2\tau}} N_5(t) \end{aligned} \quad (5.10)$$

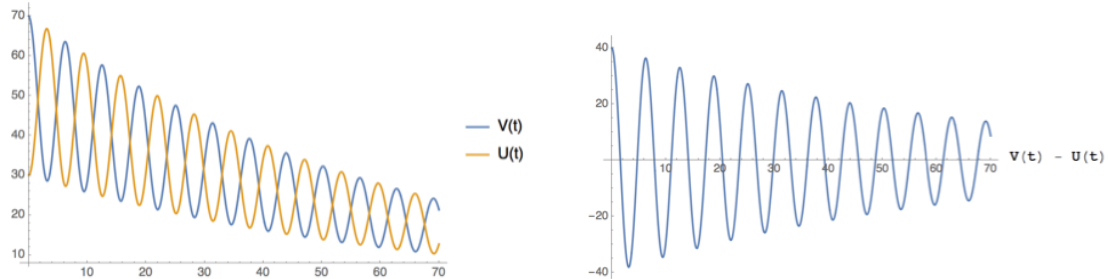
Here  $\tau = \gamma\tau_\mu$ , and the factors out front are each close to 1/4 and account for the degree of muon decay over a time period of  $T_a/2$ . Similar to  $T_a$ , the muon lifetime must be known a priori. Its value is taken as 64.44  $\mu\text{s}$ , determined from fits to the data. A systematic study regarding this parameter is described in Section 5.5.5. The ratio spectrum is then almost exactly described by just the cosine term,

$$R(t) \approx A \cos(\omega_a t), \quad (5.11)$$

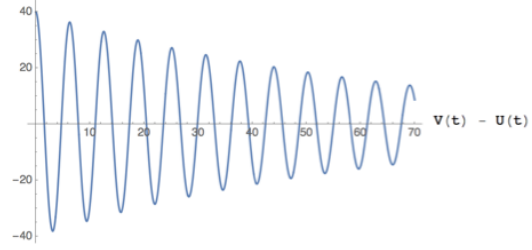
in the absence of other effects in the data.



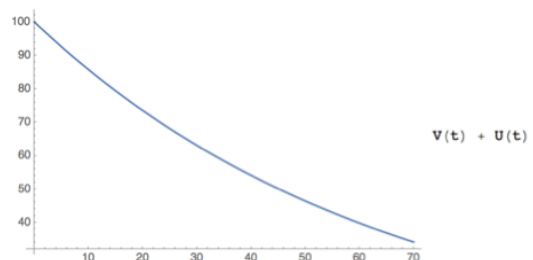
(a) The five parameter function defined in Equation 5.3, which describes the incoming data to first order.



(b)  $U(t)$  and  $V(t)$  functions which describe the time-shifted and unshifted ratio datasets.



(c) The numerator function in the formed ratio,  $V(t) - U(t)$ . It is an exponentially decaying cosine.



(d) The denominator function in the formed ratio,  $V(t) + U(t)$ . It is an exponentially decaying curve.



(e) The formed ratio function, describing the data after it has been handled as described in the text. To first order it is reduced to a simple cosine form.

Figure 5.13: Functions describing the formation of the ratio in the data.

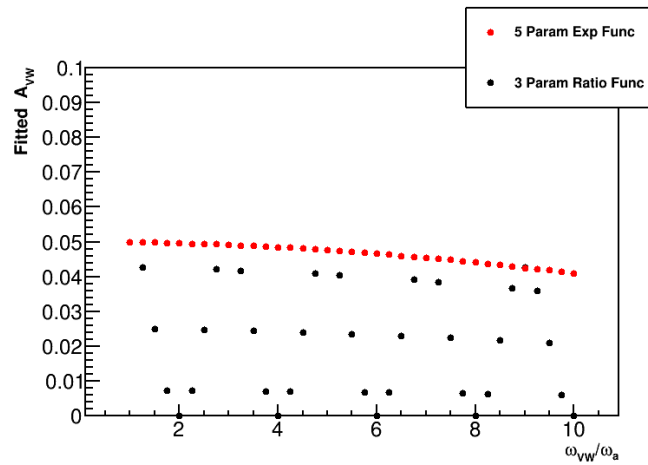


Figure 5.14: Fitted amplitude for a VW effect as a function of frequency in units of  $\omega_a$  in a Toy MC simulation, with a five parameter function in red and a three parameter ratio function in black. The input amplitude was 0.05. The fall off of red points is due to the high frequencies relative to the bin widths leading to an underestimate of the amplitude; performing an integral fit removes this trend. As shown the amplitude of the effect goes to zero for frequencies which are an even multiple of  $\omega_a$ .

### 5.3 Fitting the data

The basic five parameter function used to fit the data as described before is given as<sup>10</sup>

$$f(t) = \mathbf{N}_0 \cdot e^{-t/\tau} \cdot (1 + \mathbf{A} \cdot \cos(\omega_a t + \phi)), \quad (5.12)$$

where the fit parameter for  $\omega_a$  is recast in terms of a ppm level shift  $\mathbf{R}$  on a reference frequency,

$$\omega_a = 2\pi \cdot 0.2291 \text{ MHz} \cdot (1 + \mathbf{R} \times 10^{-6}). \quad (5.13)$$

This reference frequency of 0.2291 MHz was the same reference frequency used in E821, and  $\mathbf{R}$  is blinded at the hardware and software levels [91, 92]. Fitting the data with Equation 5.12 however is insufficient to properly describe the data. Figure 5.15 shows there are peaks in the FFT due to beam dynamics frequencies corresponding to the CBO, VW, and some beat frequencies with  $\omega_a$ . In order to properly account for these effects, additional terms need to be added to the fit function.

Equation 5.12 can be expanded to

$$f(t) = \Lambda(t) \cdot V(t) \cdot N_{cbo}(t) \cdot \mathbf{N}_0 \cdot e^{-t/\tau} \cdot (1 + A_{cbo}(t) \cdot \cos(\omega_a t + \phi_{cbo}(t))), \quad (5.14)$$

where many additional terms have been added in order to account for effects in the data. The various additional terms  $\{N_{cbo}(t), A_{cbo}(t), \phi_{cbo}(t), V(t), \Lambda(t)\}$  are described in the following sections. Fitting the data with this function, referred to as the “Threshold Method” or just “T-Method,” while not the subject of this dissertation, was done in this analysis as a diagnostic and informative tool for the Ratio Method analysis.

---

<sup>10</sup>In all cases here and onwards the actual fit parameters are in bold.



Figure 5.15: FFT of five parameter fit residuals. Peaks corresponding to beam dynamics frequencies of the CBO and VW and some beat frequencies with  $\omega_a$  are readily apparent. A rise at low frequencies corresponds to the effects of the lost muons in the data. The VW peak disappears with the additional level of time randomization at that frequency. From the 60h dataset.

In order to fit the ratio time spectra as constructed in Section 5.2.2, a different function is used. While the immediate inclination is to use an expansion of Equation 5.11 with included additional effects similar to the T-Method fit function, instead the fit function used is a return to the explicit definition of the construction of the ratio time spectra in Equations 5.6 and 5.7. Including the additional effects previously mentioned, the fit function goes as

$$R(t) = \frac{2f(t) - f_+(t) - f_-(t)}{2f(t) + f_+(t) + f_-(t)}, \quad (5.15)$$

$$f_{\pm}(t) = f(t \pm T_a/2), \quad (5.16)$$

$$f(t) = \Lambda(t) \cdot V(t) \cdot N_{cbo}(t) \cdot (1 + A_{cbo}(t) \cdot \cos(\omega_a t + \phi_{cbo}(t))). \quad (5.17)$$

The  $f(t)$  given here differs from that in Equation 5.14 in that the  $N_0 \cdot e^{-t/\tau}$  terms have divided out, thus reducing the number of fit parameters necessary to model the data. Using this function as opposed to an expansion of the three parameter ratio function eliminates any approximations made in that three parameter function derivation, and any fit parameters should be consistent in value between the T-Method and Ratio Method results, barring adjustments due to the application of the Ratio Method.

Because the Ratio Method reduces the sensitivity of the  $\omega_a$  extraction to various effects in the data, peaks that appear in the FFT of the five parameter fit residuals don't appear in the FFT of the three parameter ratio fit residuals, Figure 5.16. Indeed except for bad fits, unless one looks at the FFT over the early part of the fit (first 30  $\mu$ s) or at the shape of the Ratio Method denominator, one might not know the effects even exist in the data at all. However those effects typically still need to be included in the fit function for a proper estimation of  $\omega_a$ , and because of the reduction in sensitivity, there are some parameters which the ratio has trouble fitting by itself. Using the T-Method fit function is then a useful tool for constraining these specific parameters.



(a) FFT of fit residuals over all times within the fit range. There is no immediately apparent structure for residual effects left out of the fit function.



(b) FFT of fit residuals over the first 30  $\mu$ s. The CBO peak can be seen above the noise, though the corresponding beat frequencies do not appear.

Figure 5.16: FFT of three parameter ratio fit residuals. Dashed blue lines indicate various beam dynamics frequencies and their beat frequencies with  $\omega_a$ . Data from the 60h dataset.

### 5.3.1 CBO terms

As described in Section 2.6.1, the CBO modulates the  $\omega_a$  oscillation. This shows up as a modification on the five parameter function parameters  $\{N_0, A, \phi\} \rightarrow \{N_0 \cdot N_{cbo}(t), A_{cbo}(t), \phi_{cbo}(t)\}$  where these terms are given to first order as

$$N_{cbo}(t) = (1 + \mathbf{A}_{cbo-N} \cdot e^{-t/\tau_{cbo}} \cdot \cos(\omega_{cbo}(t) \cdot t + \phi_{cbo-N})) \quad (5.18)$$

$$A_{cbo}(t) = \mathbf{A} \cdot (1 + \mathbf{A}_{cbo-A} \cdot e^{-t/\tau_{cbo}} \cdot \cos(\omega_{cbo}(t) \cdot t + \phi_{cbo-A})) \quad (5.19)$$

$$\phi_{cbo}(t) = \phi_0 + \mathbf{A}_{cbo-\phi} \cdot e^{-t/\tau_{cbo}} \cdot \cos(\omega_{cbo}(t) \cdot t + \phi_{cbo-\phi}) \quad (5.20)$$

In Equation 5.18 the  $N_0$  term is left out since the ratio fit includes the  $N_{cbo}(t)$  term but not  $N_0$ , and in Equation 5.20,  $\phi_{cbo}(t)$  has an additive phase instead of a multiplicative one since  $\phi_0$  is not an amplitude and can be equal to zero. Each of the terms then includes additional fit parameters in an extra amplitude and phase, as well as one shared CBO lifetime and frequency. As described in Section 4.4, the default model for the CBO modulation is assumed as an exponentially decaying envelope. The CBO frequency,  $\omega_{cbo}(t)$ , was time-dependent for Run 1 as found in Section 4.4. The function for the CBO frequency shown in Figure 4.27 is given in the fit function as

$$\omega_{cbo}(t) = \omega_{cbo} \cdot \left(1 + \frac{Ae^{(-t/\tau_A)}}{\omega_0 t} + \frac{Be^{(-t/\tau_B)}}{\omega_0 t}\right), \quad (5.21)$$

where  $\omega_{cbo}$  is the free fit parameter, and the model parameters  $\{\omega_0, A, \tau_A, B, \tau_B\}$  are fixed from the tracking analysis. These parameters for the various datasets and two tracker stations are given in Table 5.2.

It should be noted that Equations 5.19 and 5.20 are not necessarily needed in order to get good fits to the data (whereas Equation 5.18 always is). This is typically dataset or random seed dependent. While some datasets had certain parameters with large errors relative to their amplitudes, for this analysis all terms were successfully

CBO Frequency Model Parameters						
Dataset	Tracker Station	$\omega_0$ (rad/ $\mu$ s)	$A$ (rad)	$\tau_A$ ( $\mu$ s)	$B$ (rad)	$\tau_B$ ( $\mu$ s)
60h	12	2.3389	2.9	81.8	5.12	7.7
	18	2.3387	2.82	81.1	5.08	8.2
HighKick	12	2.6145	3.27	52.8	6.96	6.6
	18	2.6137	3.23	46.2	6.61	6.8
9d	12	2.6106	2.86	72.8	5.50	8.5
	18	2.6110	2.89	79.2	5.44	9.2
Endgame	12	2.3377	7.43	95.1	4.71	9.0
	18	2.3379	7.44	95.2	4.90	9.2

Table 5.2: Fixed parameters in the CBO frequency model [93, 94].

**Here I source personal communication with James, as I don't think there's a source for the HighKick numbers.**

included in all dataset fits with appropriate tuning of the starting parameters with well converging fits.

When considering higher order CBO modifications to the fit function, the only term that was found to be fittable was the second order CBO modulation on the  $N_0$  term,

$$N_{2cbo}(t) = (1 + \mathbf{A}_{2cbo-N} \cdot e^{-2t/\tau_{cbo}} \cdot \cos(\omega_{cbo}(t) \cdot t + \phi_{2cbo-N})). \quad (5.22)$$

This stands to reason as the  $N_{cbo}(t)$  is the largest CBO effect. The form is assumed to be the same as the first order CBO terms, except the lifetime of the effect is half the CBO lifetime,  $\tau_{cbo}/2$ . This is due to the fact that the  $N_{2cbo}(t)$  is reasoned to come from the width of the oscillating beam, as opposed to the oscillating mean. Indeed as will be shown in Section 5.4.1, the inclusion of this term is necessary to get good fits to the per calorimeter data, where the CBO effect is stronger compared to in the sum of the calorimeter data. For this reason, and again because the  $N_{2cbo}(t)$  term is fittable in the calorimeter sum data, this term is included in fits to each of the datasets.



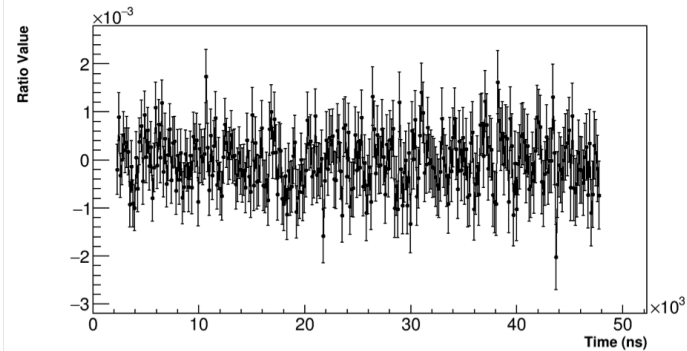
Figure 5.17: Fitted VW amplitude as a function of the choice of offset from  $T_a$  in units of thousands of ppm for the 60h dataset. The default time-shift lies at 0 on this plot, right on the resonance where the VW amplitude blows up. Only by time-shifting by a drastically different amount (which negatively affects R), can the resonance be avoided.

Systematic studies relating to the choice of envelope and choice of fixed parameters in the frequency model are explored in Section 5.5.3. For future runs beyond Run 1, it may be necessary to include the higher order modifications to the  $\mathbf{A}$  and  $\phi$  terms.

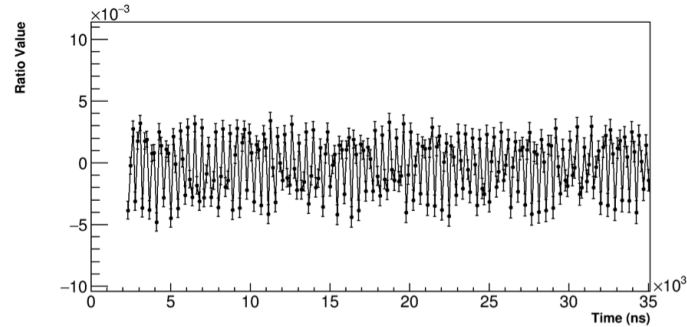
### 5.3.2 VW term

As mentioned briefly at the end of Section 5.2, the VW effect is time-randomized out of the data, such that  $V(t) = 1$ . This is done due to complications with the Ratio Method. In the 60h and Endgame datasets, the VW frequency was found to be nearly  $10 \cdot \omega_a$ , on a potential resonance. While to first order this even multiple frequency implies the VW effect should completely cancel out in the Ratio Method, Figure 5.14, the FR effect in combination with the VW leads to a modified envelope for the VW effect in the Ratio Method fits and inflated VW amplitudes [95]. See Figures 5.17 and 5.18.

For the 9d dataset which has a VW frequency that's nearly  $9 \cdot \omega_a$  and avoids said resonance (and by extension the HighKick), it was found that the Ratio Method flattened out the VW amplitudes as a function of calorimeter number leading to a



(a) Without the FR effect included.



(b) With the FR effect included.

Figure 5.18: Ratio data with and without the FR effect from a Toy MC simulation, with a VW effect with a frequency  $\omega_{VW} = 10 \cdot \omega_a$ . The  $\omega_a$  wiggle itself has been removed, and the lifetime of the VW was set to a large number. The top plot shows ratio data which is consistent with 0 after all effects have been removed and the VW has divided out. The bottom plot shows ratio data inconsistent with 0, with oscillations at the VW frequency, and an interesting beating structure. Note the different scales.

<b>Change in Asymmetry due to VW Randomization</b>				
Dataset	$A$ no randomization	$A$ with randomization	$\Delta A$	$\Delta\sigma_R$ (ppb)
60h	0.3697	0.3637	-0.0060	22.7
9d	0.3714	0.3639	-0.0075	18.1
Endgame	0.3747	0.3686	-0.0061	10.7

Table 5.3: Asymmetry values in three of the Run 1 datasets with and without the VW randomization, and the corresponding change in the statistical error on R. An energy cut of 1700 MeV was applied to the data. The HighKick dataset has the lowest asymmetry and the least statistics, so the increase in the statistical error would be negligible as it is for the other datasets.

systematically smaller VW amplitude in the calorimeter sum fit. The simplest solution to remove both of these problems was to randomize out the VW effect entirely. Table 5.3 gives the change in asymmetry and corresponding change in the statistical error on R due to this added time randomization for three of the Run 1 datasets. It was found that the added randomization increased the statistical error on R by a negligible amount for the Run 1 analysis. It was also found that the added level of time-randomization changed the mean value of R for many random seed fits to the data by a small amount, statistically consistent without the extra randomization [95]. Going forward for the future runs, it may be necessary to include the proper VW envelope in the fits using a functional form of the FR instead of randomizing out the effect.

Barring the envelope changes in the Ratio Method, here is still given the form for the VW as it is used in the T-Method fits. The form for the VW term is taken identically to the CBO terms,

$$V(t) = 1 + \mathbf{A}_{\mathbf{VW}} \cdot e^{-t/\tau_{\mathbf{VW}}} \cos(\omega_{\mathbf{VW}}(t) \cdot t + \phi_{\mathbf{VW}}), \quad (5.23)$$

with an exponentially decaying envelope, and an additional amplitude and phase

parameter. The VW frequency  $\omega_{VW}$  is given in Equation 2.26, where it is seen to be dependent on the cyclotron frequency and vertical betatron frequency. Using Equations 2.20 and 2.25, the dependence on the CBO frequency is seen as

$$\begin{aligned}\omega_{VW}(t) &= 2\pi(f_c - 2f_{yBO}), \\ &= 2\pi\left(f_c - 2f_{cbo}(t)\sqrt{2f_c/f_{cbo}(t) - 1}\right),\end{aligned}\tag{5.24}$$

where  $f_{cbo}(t) = \omega_{cbo}(t)/2\pi$  is determined in the tracking analysis as described in Section 5.3.1 and given by Equation 5.21. While Equation 5.24 is the theoretical frequency for the VW effect, it was found in the tracking analysis that including an adjustment factor on the CBO frequency  $f_{cbo} \rightarrow \kappa f_{cbo}$  on the order of about a percent resulted in better agreement with the directly measured VW frequency [83, 96]. In the fitting function itself, the VW frequency is then taken as

$$\omega_{VW}(t) = 2\pi\left(f_c - 2 \cdot \kappa_{VW} \cdot f_{cbo}(t)\sqrt{2f_c/(\kappa_{VW} \cdot f_{cbo}(t)) - 1}\right),\tag{5.25}$$

where now the VW frequency fit parameter is  $\kappa_{VW}$ . The origin of this extra factor is unclear, whether it is a tracker measurement issue, something to do with the frequency function approximation, or if it has something to do with the electrostatic quadrupoles. The inclusion of the extra factor however provides better fits and so it is kept in.

### 5.3.3 Lost muons

Muons lost from the storage ring during the frequency analysis portion of each fill will distort the observed decay positron spectrum. These hits show up as a rise at low frequencies in the FFT of the fit residuals due to the slow nature of the effect, Figure 5.15. These muon losses typically originate from those muons with large betatron amplitudes which hit material near the edge of the storage ring, or those

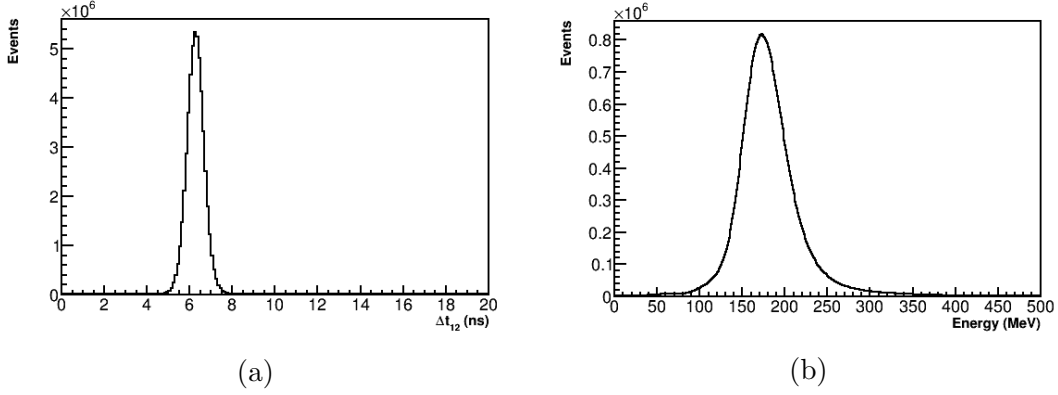


Figure 5.19:  $\Delta t$  and energy deposition distributions for lost muons passing through adjacent calorimeters. A typical flight time is 6.5 ns and energy deposition is 170 MeV. Data from the Endgame dataset.

muons which experience local field perturbations one too many times. In both cases the muons will lose energy and spiral inward out of the ring, a fraction of which will then pass through multiple calorimeters. Because lost muons are minimum-ionizing particles (MIPs), they are relatively easily identified by their small energy deposition signature in hit calorimeters, around 170 MeV as shown in the left peak in Figure 5.4. These lost muons typically have a flight time between adjacent calorimeters of  $\Delta t_{12} = 6.5$  ns [97, 98]. The  $\Delta t$  and energy deposition distributions are shown in Figure 5.19. By looking for coincidences between three adjacent calorimeters, or triples, and then applying cuts and subtracting backgrounds, a pure sample of lost muons can be constructed. This lost muon spectrum  $L(t)$  can then be implemented into the fit function in order to account for the positrons that would have been observed in the absence of losses.

The cuts used for the lost muon selection are given in Table 5.4. Triple coincidences are only included where every cluster consists of three or less crystals hit, with 80% of the energy deposited in one crystal.  $\Delta t$  and energy deposition ranges are taken as  $5 \text{ ns} \leq \Delta t_{12,23} \leq 7.5 \text{ ns}$  and  $100 \text{ MeV} \leq E_{1,2,3} \leq 250 \text{ MeV}$ , where these ranges come from inspection of Figure 5.19. The  $\Delta t_{12}$  distribution as a function of time in-fill is

<b>Lost Muon Cuts</b>	
Parameter	Value or Range
Cluster size	$\leq 3$ crystals
Cluster energy fraction	$\geq 0.8$ in main crystal
Time of flight between adjacent calorimeters	$5 \text{ ns} \leq \Delta t_{12,23} \leq 7.5 \text{ ns}$
Energy deposition	$100 \text{ MeV} \leq E_{1,2,3} \leq 250 \text{ MeV}$
Time of flight between separated calorimeters	$\Delta t_{13} \leq 14.4 \text{ ns}$

Table 5.4: Lost muon selection cuts. In a triple coincidence the subscripts of 1, 2, and 3 correspond to the three calorimeters hit clockwise around the ring.

shown in Figure 5.20. By examining this distribution in the range  $2 \text{ ns} \leq \Delta t_{12} \leq 4 \text{ ns}$ , and averaging the contained counts, an approximation for the accidental background can be determined and subtracted off the triples spectrum. The accidental background typically comes from either double coincidences and a real positron hit, or a particle shower induced by an incident positron which hits an adjacent calorimeter.

Also shown in Figure 5.20 are two bands of stable beam contaminants corresponding to stored deuterons and protons. These particles have different times of flights between calorimeters due to their larger masses. By looking at the  $\Delta t_{13}$  distribution for times greater than  $300 \mu\text{s}$ , the deuteron population is easily isolated, Figure 5.21. While the deuteron population is mostly removed by the  $\Delta t_{12}$  cut, an additional cut of  $\Delta t_{13} \leq 14.4 \text{ ns}$  helps remove any remaining deuteron contamination. The proton population, due to it's nearness to the real lost muon population, is harder to remove. The simplest solution is to simply cut on the negative side of the  $\Delta t_{12}$  or  $\Delta t_{13}$  distributions. See Section 5.5.4 for the results using this additional cut. It was found that the proton contamination makes almost no difference to the fitted value of R. The default choice then is to use the previously specified cut ranges in order to increase the amount of statistics in the lost muons distribution with which to fit. A study into the exact rate of these beam contaminants is included in Reference [99].



Figure 5.20:  $\Delta t_{12}$  distribution as a function of time in-fill before any cuts. Note the log scale. Lost muons have a  $\Delta t_{12}$  distribution centered at 6.5 ns. The accidental background can be seen as counts out at  $\Delta t$ 's far from the center of the distribution. Color striations in the core of the distribution correspond to CBO periods. There are two bands of hits that do not fall off as severely with time as the lost muons do. The band contained mostly between 7 and 8 ns corresponds to deuterons, while the band contained mostly between 6 and 7 ns corresponds to protons. Data from the Endgame dataset.

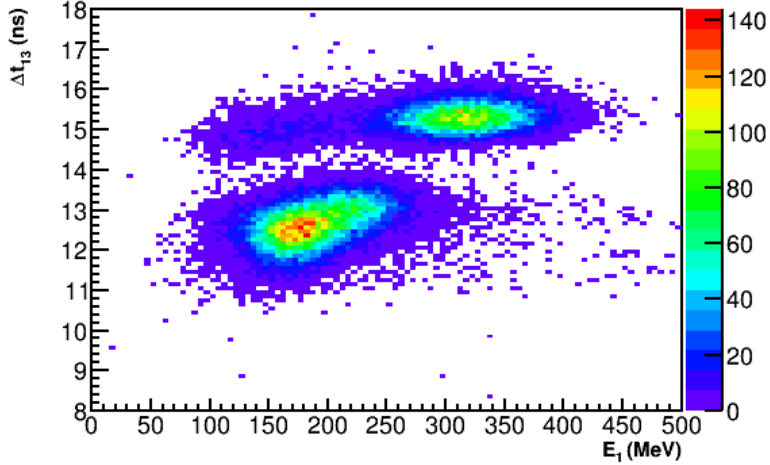


Figure 5.21:  $\Delta t_{13}$  distribution as a function of energy for times greater than 300  $\mu$ s. The lost muons can be seen as a blob centered at 170 MeV and  $\Delta t_{13} \approx 12.5$  ns, while the deuterons can be seen as the oblong blob at  $\Delta t_{13} \geq 14.4$  ns. While the deuterons have a preferentially larger energy deposition, they can be seen to extend to low energies, making cutting on energy unrealistic. Though not easily separated by eye, the stored protons are contained within the upper right portion of the lost muons blob. Data from the Endgame dataset.

The last background is the quadruples spectrum. Due to how the triple coincidences are constructed, real quadruples will be counted as two separate triples. While the quadruples spectrum can be used instead of the triples spectrum for a purer sample of lost muons, the amount of statistics is much reduced, and similarly for higher order coincidences. The quadruples spectrum is constructed in the same was as the triples with the same cut ranges. The quadruple background is removed by subtracting off those triples which originated from quadruple coincidences.

Figure 5.22 shows the final  $\Delta t_{12}$  distribution with cuts as a function of time infill for selected lost muons. The final 1D triple losses spectrum  $L(t)$  is shown in Figure 5.23. Once we have the lost muon distribution we need to include it in the fit function in order to account for the changing number of hits over the course of the fill. The true lost muon rate will be given by  $L(t)/\epsilon$ , where  $\epsilon$  is the loss detection

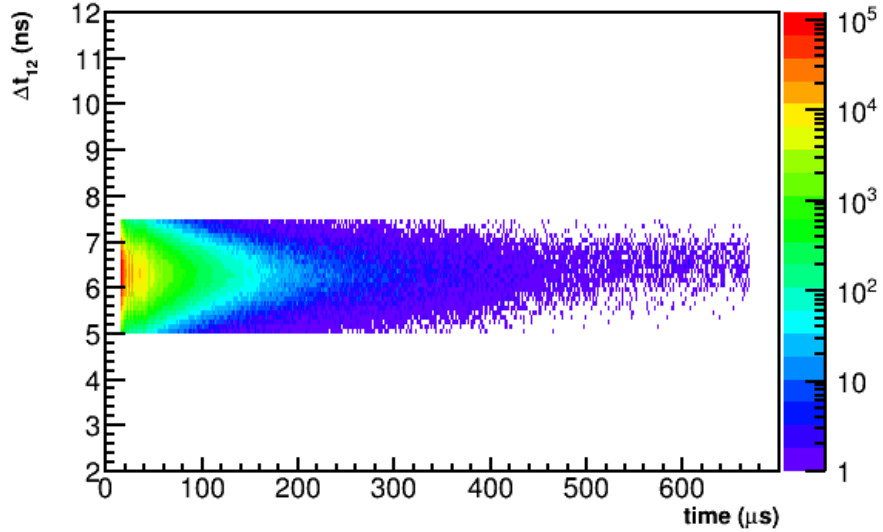


Figure 5.22: Final  $\Delta t_{12}$  distribution for selected lost muons as a function of time in-fill. Data from the Endgame dataset.



Figure 5.23: Lost muon triples spectrum  $L(t)$  as a function of time in-fill, after all cuts and background subtractions. Also shown are the quadruples and accidental background distributions, which can be seen to be much smaller than the triples. The shape of the triple and quadruple spectra can be seen to be nearly the same. The shape of the triples spectrum comes from beam dynamics (CBO) and lost muon acceptance effects. Data from the Endgame dataset.

efficiency [84]. The change in the number of muons within the storage ring can be written as

$$dN = -\frac{N}{\tau}dt - \frac{L(t)}{\epsilon}dt, \quad (5.26)$$

where the solution can be determined by inspection as

$$N(t) = N_0 \cdot e^{-t/\tau} \cdot \left(1 - \frac{1}{\epsilon N_0} \int_{t_0}^t L(t')e^{(t'/\tau)}dt'\right). \quad (5.27)$$

The parameter  $\tau$  is the same muon lifetime as in the T-Method fit function, except here it is set as the default value of  $64.44\text{ }\mu\text{s}$ <sup>11</sup>. The value for  $t_0$  can be taken as any time at or before the start of the fitting range, as it simply changes the scale of  $N_0$  which is largely unimportant. The modification  $\Lambda(t)$  as listed in Equation 5.14 is then taken as

$$\Lambda(t) = 1 - \kappa_{loss} \int_{t_0}^t L(t')e^{(t'/\tau)}dt' \quad (5.28)$$

where  $\kappa_{loss} = 1/\epsilon N_0$  is taken as the fit parameter<sup>12</sup>.

It should be noted that the Ratio Method is largely insensitive to the slow lost muons effect which divides out. No rise appears in the FFT of the ratio fit residuals, Figure 5.16, and letting  $\kappa_{loss}$  float in the fit does not produce fit nice convergence. It was found however that  $R$  changes on the order of tens of ppb when the lost muon term is included with  $\kappa_{loss}$  fixed to the value determined from a T-Method fit, so by default it is included. See Section 5.5.4 for more discussion on this.

---

<sup>11</sup>The fitted  $\omega_a$  frequency is largely insensitive to this parameter, and especially so in the Ratio Method fits, so this is acceptable.

<sup>12</sup>By construction  $\kappa_{loss}$  is a very small parameter,  $\mathcal{O}(10^{-10})$ . This factor is absorbed into the parameter in such that the fit parameter is  $\mathcal{O}(1)$ .

### 5.3.4 Fit procedures and parameters

$\chi^2$  fits are done to the pileup corrected positron time spectra and ratio data in `ROOT` using the standard `TH1F` and `TGraph` fit methods with a strategy level of two. Fits are performed in stages where groups of associated parameters are freed, fit, and then fixed before fitting the next set of parameters. In the final fit all parameters are freed and fit at once. Each of the four Run 1 precession frequency analysis datasets are fit with 14 parameters. 13 parameters are free in fits to the 60h, 9d, and Endgame datasets, with the  $\kappa_{loss}$  parameter determined and fixed from a T-Method fit. In the HighKick dataset  $\tau_{cbo}$  is also fixed from a T-Method fit as the lifetime is relatively small and the Ratio Method can't successfully fit it, resulting in 12 free fit parameters. In the T-Method fits there are two extra free fit parameters, those being the  $N_0$  and  $\tau$  terms which are left out of the Ratio Method fits.

Fits to calorimeter sum spectra are done from 30.2–650  $\mu\text{s}$ , corresponding to 4155 bins. The choice of fit start time was made to lie directly on a  $g - 2$  zero crossing, which from E821 was shown to reduce some systematic errors [cite this?](#). It was also made at a late enough time to allow for storage of the muon beam after the scraping procedure. The choice of fit end time was made to be just before the quad storage field turned off, in order for the fill time to fit within the timing structure of the experimental beam. Individual calorimeter fits were performed out to 400  $\mu\text{s}$ , in order to stay within the region of Poisson statistics such that  $\chi^2$  fits are satisfied. Table 5.5 gives the various fit procedure parameters.

As a reminder  $R$  is blinded at the hardware and software levels [91, 92]. The software blinding string used for the 60h dataset was different than that used when fitting the HighKick, 9d, and Endgame datasets, each of which used the same blinding string. This was done in order to perform a software-level relative unblinding exercise between different analyzers with the 60h dataset in order to determine if there were any

Fit Procedure Parameters	
Parameter	Value
Fit strategy level	2
Fit start time	30.2 $\mu$ s
Fit end time (calorimeter sum)	650 $\mu$ s
Fit end time (calorimeters)	400 $\mu$ s
Bins in fit (calorimeter sum)	4155
Number of fit parameters	14
Number of free fit parameters (60h, 9d, Endgame)	13
Number of free fit parameters (HighKick)	12

Table 5.5: Various parameters used in the fit procedure.

obvious problems in the analyses [100]. **Cite a summary talk somewhere? Can't find any.** Therefore in the following results,  $R$  values between different datasets are comparable between the datasets except for the 60h, barring any differences due to field conditions which are not discussed in this dissertation.

## 5.4 Fit results

Figure 5.24 shows fits to the four Run 1 precession frequency analysis datasets. Table 5.6 gives all fit parameters and their errors. In each dataset case the  $\chi^2/\text{NDF}$  is acceptable as evidenced by the p value included in the table results. Fit pulls and the FFT of the fit residuals for the 60h dataset are provided in Figure 5.25. As shown all structure has been eliminated within the fit residuals implying that all effects in the data have properly been accounted for in the fit function. The same checks were made for the HighKick, 9d, and Endgame datasets and in each case no residual structure remained. Figure 5.26 shows the correlation matrix for the fit to the 60h dataset. The only fit parameter that is significantly correlated with  $R$  is the  $g - 2$  phase. This increases the confidence in the  $\omega_a$  extraction, as effects in the data which might potentially be mis-modelled will only weakly correlate with the final fitted  $R$ .

value. The various different CBO parameters are self-correlated to different degrees depending on the parameter and the dataset that is being fit. Typically either the phases and frequencies are correlated, or the lifetimes and amplitudes. Appendix D provides the correlation matrices for the HighKick, 9d, and Endgame datasets.

The  $g - 2$  phases for the different datasets showed small differences, due primarily to upstream beam adjustments before injection into the storage ring. Similarly, slightly different asymmetries can be attributed to very small acceptance differences in the stored beams. As described in Section 5.3.3, the value for  $\kappa_{loss}$  was determined and fixed from a T-Method fit to the data. The values themselves don't directly correspond to the level of losses, as each dataset has it's own loss function  $L(t)$  which is left out of the picture here.

The CBO frequencies for the 60h and Endgame datasets with  $n$  values of 0.108 were found to be 2.338 and 2.339 rad/ $\mu$ s respectively, corresponding to approximately 0.37 MHz. For the HighKick and 9d datasets with  $n$  values of 0.120, the CBO frequencies were found to be 2.559 and 2.615 rad/ $\mu$ s respectively, corresponding to approximately 0.415 MHz. These frequencies correspond to the expected frequencies as described in Section 2.6, with some slight deviations due to statistics and the reduced sensitivity in the Ratio Method<sup>13</sup>. The CBO lifetimes between the different datasets are relatively consistent, barring the HighKick dataset for which a smaller CBO lifetime was measured. Ratio Method fits typically converge with lifetimes with large errors compared to T-Method fits, due to the reduction in sensitivity in the Ratio Method. In the HighKick dataset, the CBO lifetime did not like to converge nicely in the ratio fits, and was therefore fixed to that from a T-Method fit. The main CBO amplitudes  $A_{cbo-N}$  for the different datasets were on the order of 0.3–0.4%, while the higher order CBO amplitudes were in general an order of magnitude less. The

---

<sup>13</sup>The VW frequencies, though time-randomized out in the analysis presented here, were found to be approximately 2.30 and 2.04 MHz for the datasets with  $n = 0.108$  and  $n = 0.120$  respectively.

strength of the various higher order CBO amplitudes fluctuated for different datasets, with one parameter being large compared to another in one dataset and vice versa in a different dataset. In some cases, the errors on the higher order CBO term amplitudes were of the order the amplitude itself. While this implies these terms can be dropped from the fit function, all terms were included for analysis uniformity among the different datasets. These relatively large errors, while making some of the fits slightly more challenging to achieve fit convergence for, were nonetheless handled appropriately.

The final statistical errors on  $R$  for the 60h, HighKick, 9d, and Endgame datasets are 1.358, 1.411, 0.903, and 0.639 ppm respectively. The single seed  $R$  results for the HighKick, 9d, and Endgame datasets, all of which used the same blinding string, are all well within  $1\sigma$  of each other. The average  $R$  value for fits to 50 different random seeds are provided in Section 5.4.5.

Beyond looking at single fit residuals to evaluate the integrity of the fits, other checks were made to verify consistency. In general this consisted of slicing up the data in different ways and fitting the subsets. These tests and scans included fitting individual calorimeters, modifying the fit start and end times, adjusting the applied energy thresholds, and fitting individual beam bunches.

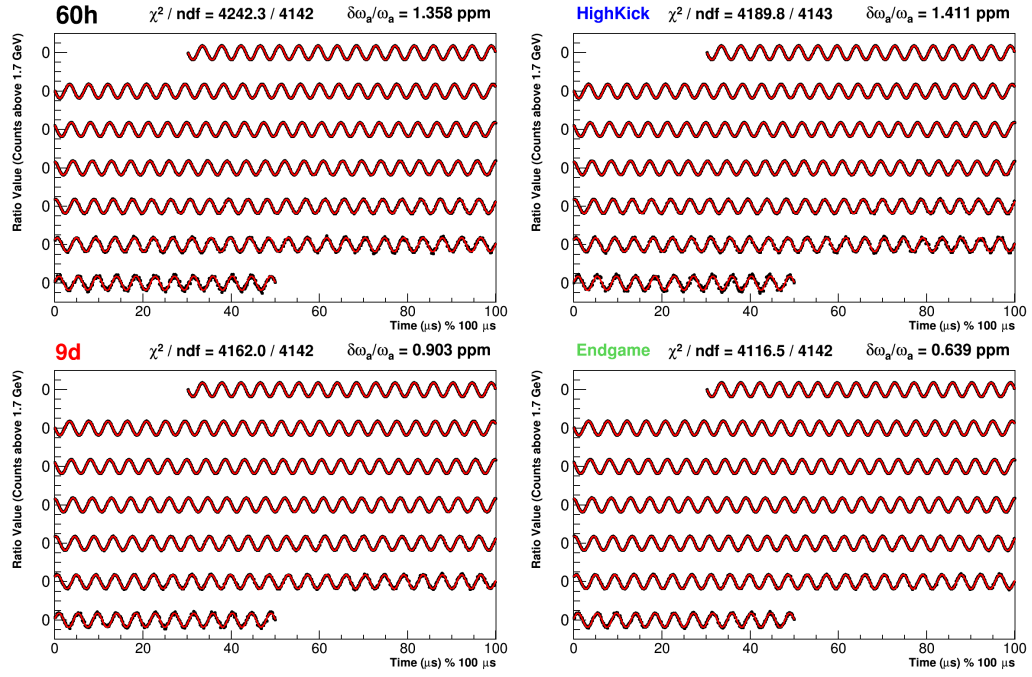


Figure 5-24: Single random seed fits to calorimeter summed data of Run 1 precession frequency analysis datasets. Data is in black and the fits are in red. The x axis is in units of  $\mu\text{s}$  modulo  $100 \mu\text{s}$ , with successive portions of the data points and fit shifted downwards on the plot. The fit ranges from  $30.2\text{--}650 \mu\text{s}$ . Dataset names are given in the upper left corners of the figures, alongside the  $\chi^2$  per degree of freedom and relative error on  $\omega_a$  or  $R$ .

Ratio Method Fit Results								
	60h		HighKick		9d		Endgame	
$\chi^2/\text{NDF}$	4242/4142		4190/4143		4162/4142		4116/4142	
p value	0.1356		0.3018		0.4104		0.6079	
Parameter	Value	Error	Value	Error	Value	Error	Value	Error
$A$	0.3637	$4.4 \times 10^{-5}$	0.3632	$4.6 \times 10^{-5}$	0.3639	$2.9 \times 10^{-5}$	0.3686	$2.1 \times 10^{-5}$
<b><math>R</math> (ppm, blinded)</b>	<b>-20.848</b>	<b>1.358</b>	<b>-17.543</b>	<b>1.411</b>	<b>-17.821</b>	<b>0.903</b>	<b>-17.567</b>	<b>0.639</b>
$\phi$	2.091	$2.2 \times 10^{-4}$	2.081	$2.3 \times 10^{-4}$	2.080	$1.5 \times 10^{-4}$	2.076	$1.1 \times 10^{-4}$
$\omega_{cbo}$ (rad/ $\mu$ s)	2.338	$1.4 \times 10^{-3}$	2.599	$6.6 \times 10^{-3}$	2.615	$5.6 \times 10^{-3}$	2.339	$0.8 \times 10^{-3}$
$\tau_{cbo}$ ( $\mu$ s)	175.2	46.8	99.4	0	137.4	62.0	200.3	33.5
$A_{cbo-N}$ ( $\times 10^{-4}$ )	43.1	5.0	42.8	9.9	39.3	9.7	32.3	2.0
$\phi_{cbo-N}$	-2.343	0.107	3.817	0.446	3.302	0.374	-0.710	0.062
$A_{2cbo-N}$ ( $\times 10^{-4}$ )	1.9	1.3	4.9	4.5	2.2	2.7	1.2	0.5
$\phi_{2cbo-N}$	3.331	0.638	5.665	1.274	-4.936	1.127	0.322	0.448
$A_{cbo-A}$ ( $\times 10^{-4}$ )	5.5	3.9	9.5	4.1	6.4	2.5	2.7	1.9
$\phi_{cbo-A}$	-0.271	0.737	-2.073	0.600	1.750	0.561	-2.825	0.686
$A_{cbo-\phi}$ ( $\times 10^{-4}$ )	8.0	4.2	5.7	4.4	8.8	3.1	1.9	1.9
$\phi_{cbo-\phi}$	-1.183	0.533	1.227	0.920	4.313	0.415	-1.576	0.995
$\kappa_{loss}$	8.974	0	5.651	0	2.510	0	2.345	0

Table 5.6: Fit parameters for the four Run 1 precession frequency analysis datasets. The bold row highlights the final fitted  $R$  values and their respective errors. As a reminder the 60h dataset has a different blinding to the rest. The  $\kappa_{loss}$  parameter is fixed in each dataset fit corresponding to the 0 value in the error column, and similarly for  $\tau_{cbo}$  in the fit to the HighKick dataset.

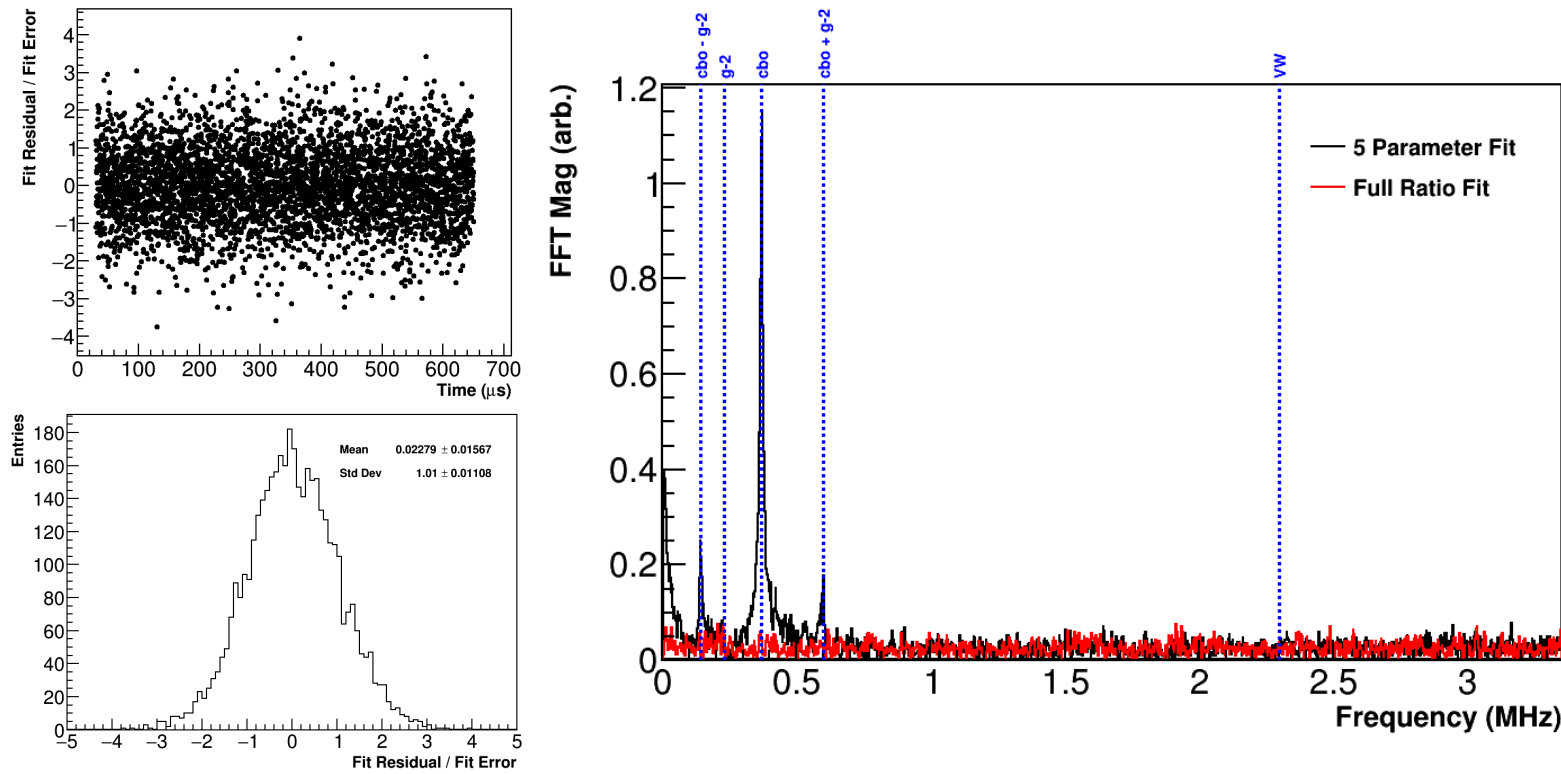


Figure 5.25: Fit pulls (top-left), their projection on to the y axis (bottom-left), and the FFT of the fit residuals (right) for the ratio fit to the 60h dataset. Note the pull projection has a Gaussian shape centered around zero with unit width. In the FFT the results from a five parameter fit to the data are overlayed, along with blue dashed lines for the main beam dynamics peaks which appear in the data. There is no obvious structure in the pulls and no remaining peaks above the noise in the ratio fit FFT.

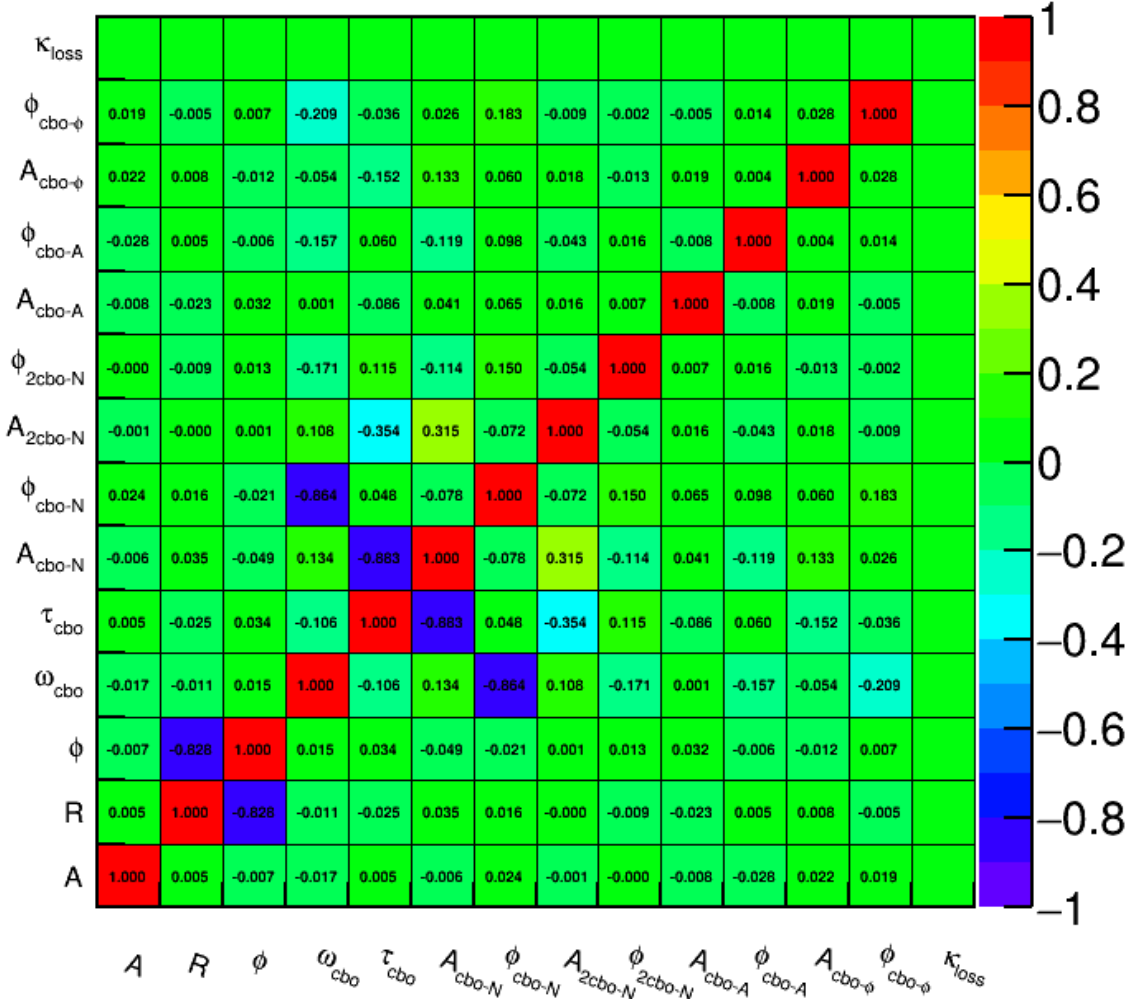


Figure 5.26: Correlation matrix for the single seed ratio fit to the 60h dataset. The only significant correlation with  $R$  is the  $g-2$  phase.  $\kappa_{loss}$  is fixed, hence the corresponding empty row and column.

### 5.4.1 Individual calorimeter fits

Fits to all 24 individual calorimeters for each of the datasets were performed with the same number of free fit parameters as used in the calorimeter summed fits. Figure 5.27 shows the  $\chi^2/\text{NDF}$ 's for the calorimeter fits which are nicely spread around 1. Figure 5.28 shows the fitted  $R$  values as a function of calorimeter number. Straight line fits were performed to the  $R$  values, and the fitted constant returned a value in each case that was consistent with the calorimeter sum fit  $R$  values. Examining the  $R$  values as a function of calorimeter between datasets, particular calorimeter numbers do not tend to lie above or below the fitted line uniformly. The spread in  $R$  values for each calorimeter then can be said to be driven statistically, though it should be noted that with the larger error bars on the individual calorimeter fits it's hard to tell if there are any preferences one way or another.

Figures 5.29 and 5.30 show calorimeter fit results for the other free parameters in the fit for the Endgame dataset. The  $g - 2$  phases are relatively consistent among the different calorimeters, barring calorimeters 13 and 19 which lie lower on the plot. These two calorimeters sit behind the tracker stations, implying a different acceptance and therefore a slightly different  $g - 2$  phase. Any correlated effects on  $R$  are not immediately observed, and might potentially be hidden behind the large errors of the fit. Similarly, the different calorimeters have different fit asymmetries, once again due to their different acceptances. The CBO parameters are in general consistent with some spread due to acceptance, with the phases running from  $0$ – $2\pi$  around the ring as expected. As one might notice, the amplitudes of the CBO parameters are an order of magnitude higher than in the calorimeter summed fits. Because the phases vary around the ring, when adding up all the calorimeters the CBO effect becomes reduced. In fact, while it is not always necessary to include the higher order CBO terms for good fits to the calorimeter summed data, there are many calorimeters

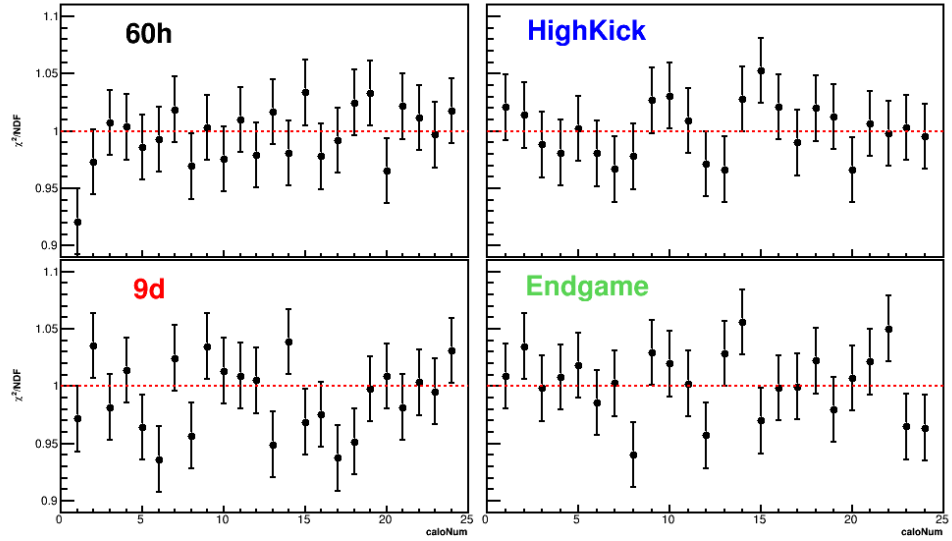


Figure 5.27:  $\chi^2/\text{NDF}$  versus calorimeter for the Run 1 precession frequency analysis datasets. Red dashed lines are placed at  $\chi^2/\text{NDF} = 1$  to aid the eye. No individual calorimeter fits are preferentially low or high when comparing across datasets.

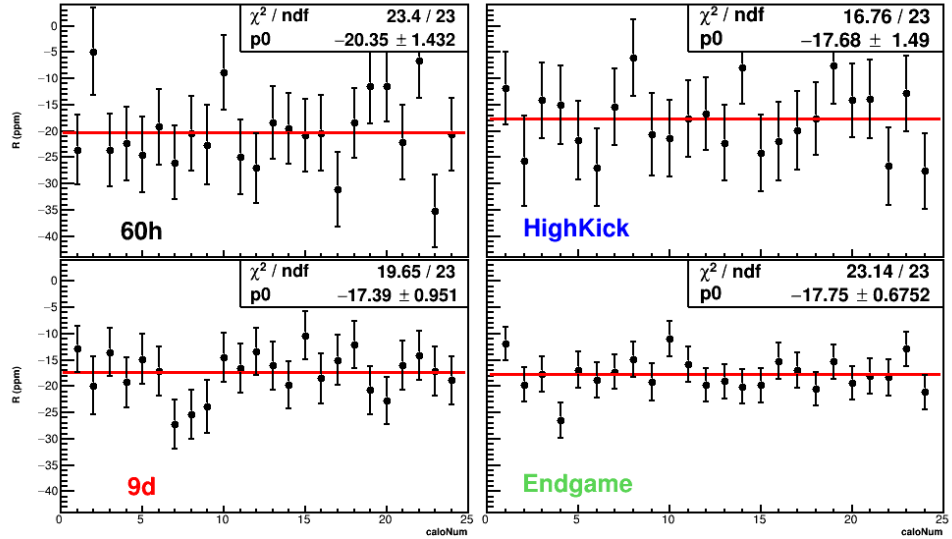


Figure 5.28:  $R$  versus calorimeter for the Run 1 precession frequency analysis datasets. The scale is the same on each of the plots. A straight line fit was performed on the fitted values, with the fit result shown in the upper right box as parameter  $p_1$  in units of ppm. The different blinding in the 60h dataset is readily observed, along with the higher precision fits in the 9d and Endgame datasets with their correspondingly smaller error bars.

which need the higher order terms for good fits.

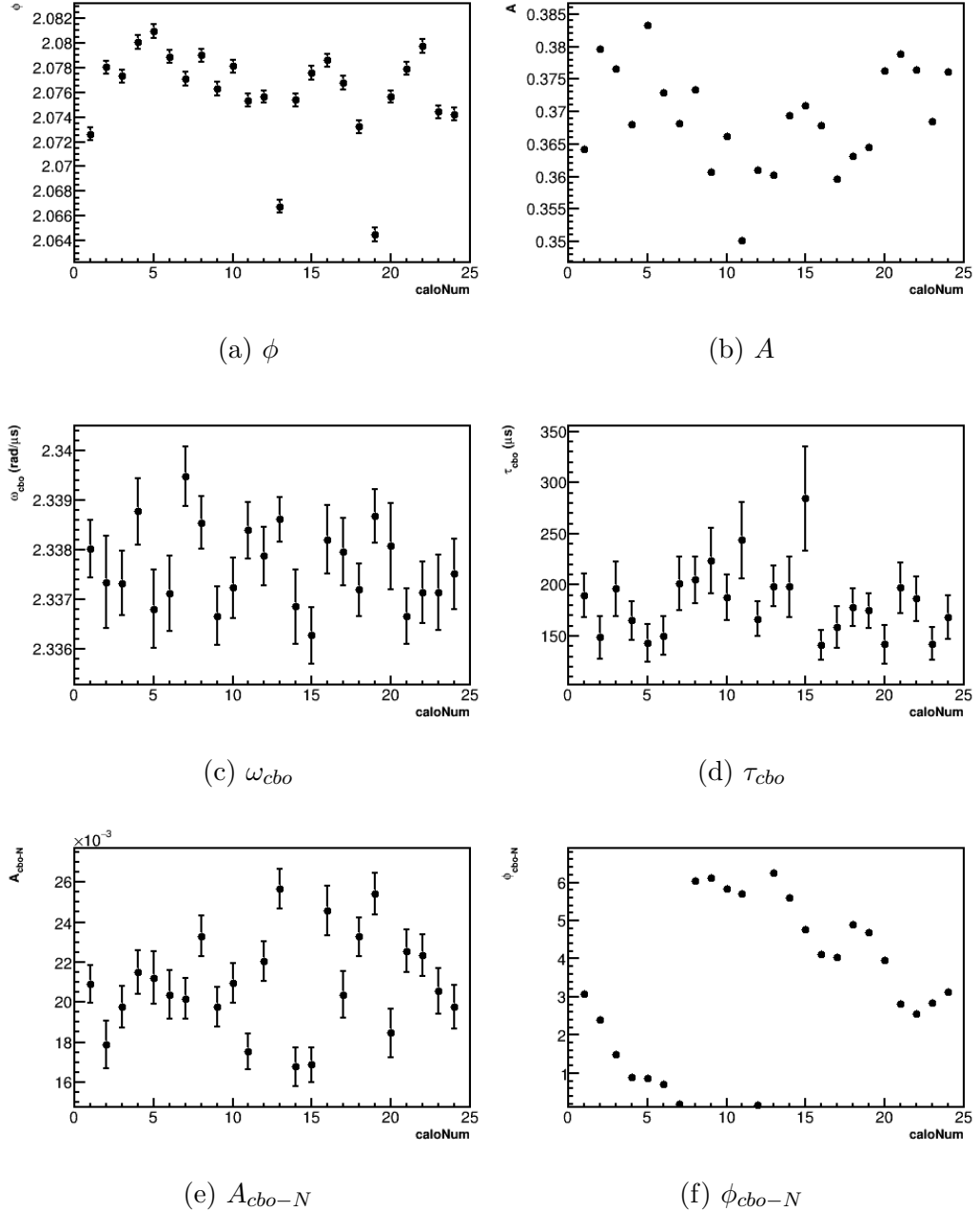


Figure 5.29: Endgame fit parameters versus calorimeter number. In the  $g - 2$  phase  $\phi$  (top-left) two points lie below the others, corresponding to those calorimeters which sit behind tracker stations. The CBO phase  $\phi_{.cbo-N}$  (bottom-right) runs from  $0-2\pi$  around the ring. These plots are typical of all datasets, with small variations in the final fitted parameters.

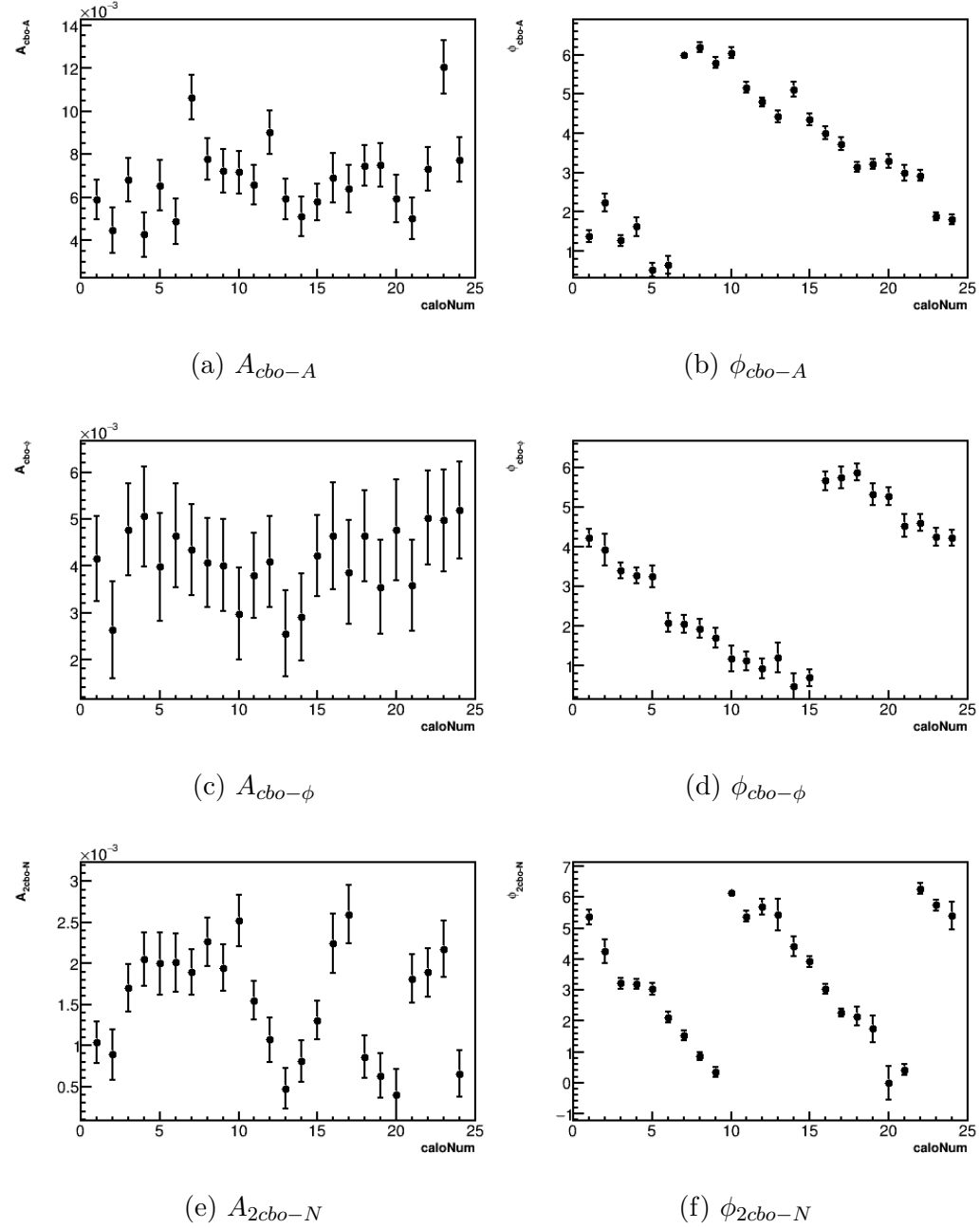
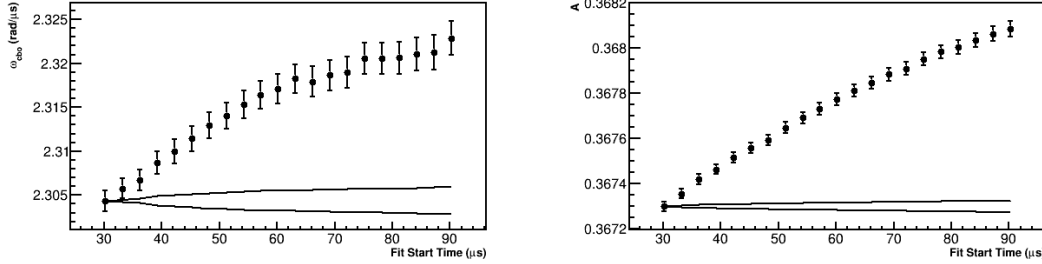


Figure 5.30: Endgame fit parameters versus calorimeter number. The CBO phases  $\phi_{cbo-A}$  and  $\phi_{cbo-\phi}$  run from  $0-2\pi$  around the ring, while  $\phi_{2cbo-N}$  runs around twice. These plots are typical of all datasets, with small variations in the final fitted parameters.



(a) The fit start scan for the fitted CBO frequency when a constant frequency model is included. The p value of the first ratio fit in this case is 0.191, indicating a good fit. Only by performing a fit start scan or examining the fit residuals closely is the deficiency in the fit observed.

(b) The fit start scan for the fitted asymmetry when the pileup is not subtracted out. If the pileup is not properly accounted for, then decay positrons with lower asymmetries contaminate the observed decay time spectrum leading to a lower fitted asymmetry value. As the pileup diminishes the fitted asymmetry tends to its true value.

Figure 5.31: Examples of fit start scans when effects are improperly accounted for in fitting. Data from the Endgame dataset.

#### 5.4.2 Fit start and end scans

In order to determine if there are any deficiencies as a function of time, for instance if the CBO was modelled incorrectly, fits are performed with varying fit start and end times. If a parameter is incorrectly modelled, it will wander away from the statistically allowed deviation as the mismodelled effect grows stronger or weaker. Two examples of this are given in Figure 5.31. In general, doing a fit start scan is a very useful tool in the precession frequency analysis beyond just verifying consistency of a fit parameter as a function of time, as it also provides hints as to what might be wrong with how the data is being handled.

The statistically allowed deviation between two sets of data, where one is a subset of the other, is given by [29]

$$\sigma_{diff} = \sqrt{\sigma_2 - \sigma_1 \left( 2 \frac{A_1}{A_2} \cos(\phi_1 - \phi_2) - 1 \right)}, \quad (5.29)$$

where the subscript 2 stands for the larger dataset while the subscript 1 stands for the smaller sub-dataset. This statistically allowed deviation depends both on the size of the datasets as well as their “analyzing powers,” which come from the asymmetries and phases of the datasets. For fit start scans the analyzing powers are in general the same, such that the approximation

$$\sigma_{diff} \approx \sqrt{\sigma_2 - \sigma_1} \quad (5.30)$$

can be made.

It should be noted that for fit start scans where much of the data is dropped at late fit start times, certain CBO parameters start to become unstable as the CBO effect becomes diminished in the data<sup>14</sup>. Fits with start times at 100  $\mu\text{s}$  are half a lifetime or more along the CBO effect, meaning that amplitudes either start to go to 0 or become unfittable. In particular, the CBO lifetime itself become very hard to fit and tends to converge to whatever the upper bound of the fit limit is while sending the amplitude to zero. For those parameters which were found to be unreliable, they were fixed to their starting fit values. These typically included most of the higher order CBO amplitudes and phases, though in some cases they can still be fit out to late times depending on the dataset.

Fit start time scans were performed from the default value of 30.2  $\mu\text{s}$  up to 100.2  $\mu\text{s}$  in steps of 1  $\mu\text{s}$  corresponding to 71 separate fits. In order to assist fit convergence, the final fit parameters from one fit were passed on as the starting parameters of the next. The  $\chi^2/\text{NDF}$ 's and fitted  $R$  values as a function of fit start time for the four Run 1 precession frequency analysis datasets are shown in Figure 5.32. The error on

---

<sup>14</sup>The same applies to the VW effect when not time-randomized out.

the individual points in the  $\chi^2$  plots are given as

$$\sigma_{\chi^2} = \sqrt{2/NDF}, \quad (5.31)$$

where NDF changes as the fit start time is pushed later in time and bins are left out of the fit. The black parabolic bands indicate the  $1\sigma$  statistically allowed deviation as given by Equation 5.30<sup>15</sup>. As shown the goodness of fit for the four datasets are all consistent with fit start time, only wandering in and near the bands without diverging.

$R$  is similarly consistent as a function of fit start time. The only dataset for which  $R$  goes noticeably outside the bands more than the others is that for the HighKick. Since the deviation is less than  $2\sigma$  and it appears to have a trend back towards the bands however, it does not appear particularly indicative of unaccounted effects in the data. In general  $R$  is very insensitive to changing fit start time, most likely simply due to the small correlations with other fit parameters.

Figure 5.33 shows the fit start scan results for the other free parameters for the Endgame dataset. In all cases the fit parameters only wander in and near the bands, showing that all effects in the ratio data are properly accounted for.

---

<sup>15</sup>These statistical deviation bands are sometimes referred to as Kawall bands.



Figure 5.32:  $\chi^2/\text{NDF}$  (top) and  $R$  (bottom) versus fit start time for the Run 1 precession frequency analysis datasets. Plots in the top and bottom rows are on the same scale respectively. The black parabolic bands represent the  $1\sigma$  statistically allowed deviation. The  $\chi^2$ 's are all consistent with 1, for which a dashed red line has been overlayed. In all cases the fit points lie in and around the  $1\sigma$  statistical bands.

For fit end scans, all of the same methods and conclusions apply. In general fit end scans are both less dangerous and more stable than fit start scans, as the amount of data being removed from the fit is relatively small. While these fit end scans in a T-Method fit might be able to be completely ignored in favor of the fit start scans, it's nice to check that they satisfy the statistical deviations in the Ratio Method as the ratio data errors grow larger with less data [100]. Fit end time scans were performed from  $650\text{ }\mu\text{s}$  to  $400\text{ }\mu\text{s}$  in steps of  $10\text{ }\mu\text{s}$ , corresponding to 26 separate fits. As in the fit start time scan, fit results from the end of one fit were passed on as the starting parameters to the next.  $R$  values for fit end scans for the Run 1 precession frequency analysis datasets are shown in Figure 5.34. As shown the  $R$  values are comfortably within and near the bands. The only dataset where  $R$  wanders a little more than the others is in the 60h dataset, however it veers back towards the bands at the end of the scan and is thus deemed acceptable.

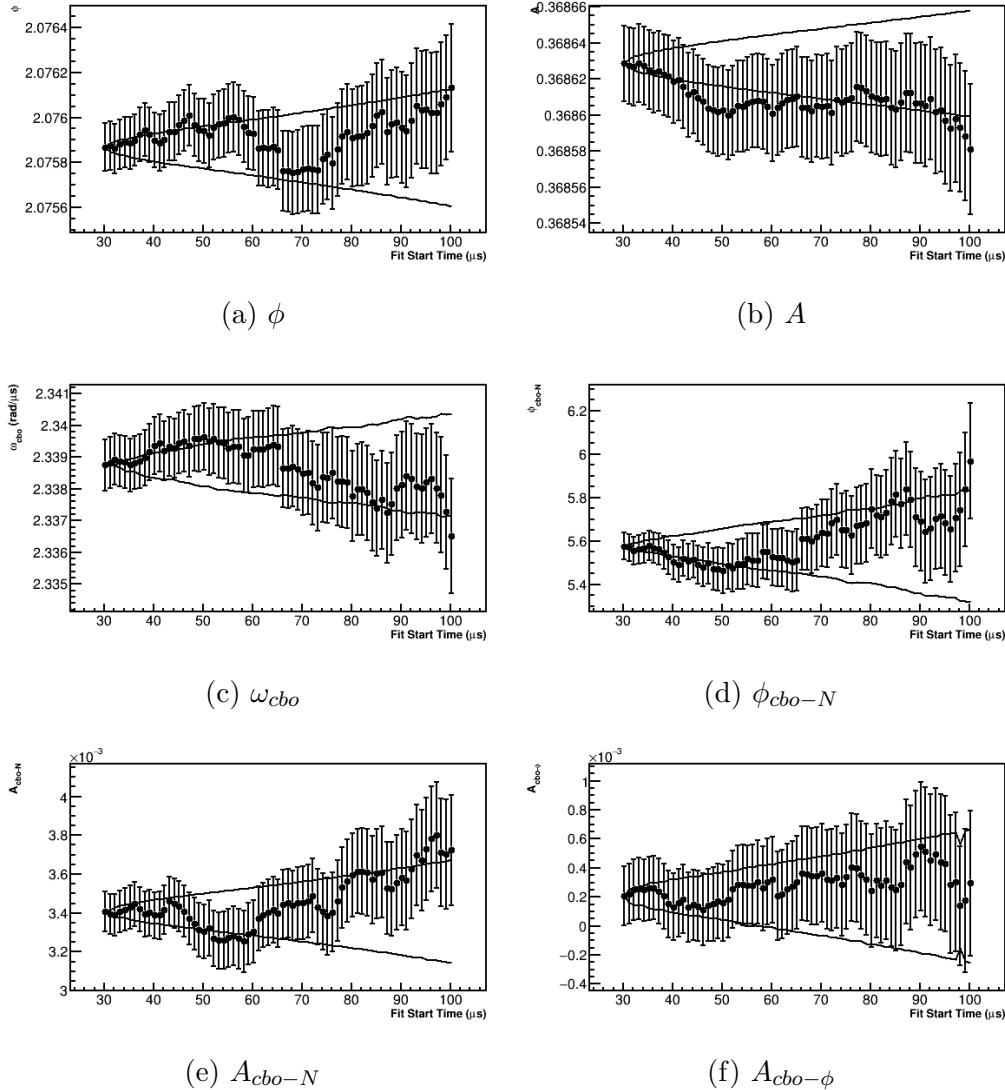


Figure 5.33: Fit start scans for free parameters in the Endgame dataset. Those parameters not shown here are fixed to their starting values over the course of the scan, as at late times they can be unstable as the CBO effects die away.

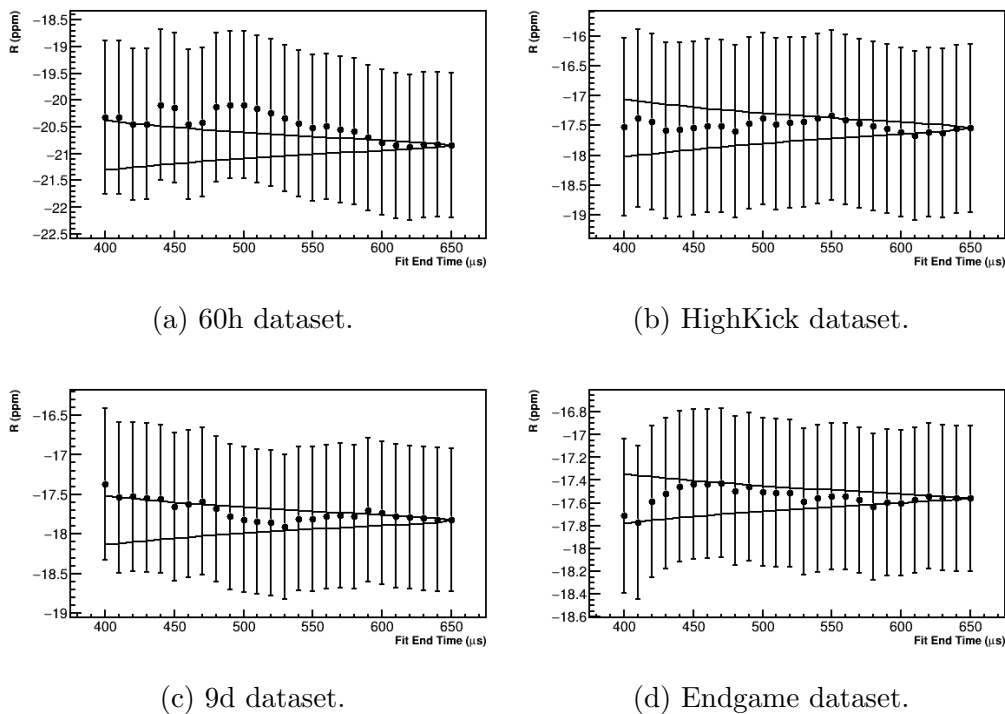


Figure 5.34:  $R$  versus fit end time for the Run 1 precession frequency analysis datasets. The fit points lie in and around the  $1\sigma$  statistical bands.

### 5.4.3 Energy threshold scans

Similarly to fit start and end time scans, it is worthwhile to verify that  $R$  is consistent regardless of the energy threshold applied to the decay positron time spectrum. The energy threshold was varied from 1.2 GeV to 2.2 GeV in steps of 50 MeV corresponding to 21 separate fits. The fitted  $R$  values for the four Run 1 precession frequency analysis datasets are shown in Figure 5.35. The statistical bands are the same as those defined in Equation 5.29, where now the analyzing power part of the equation plays a larger role as the asymmetries and phases of the different fit points are significantly different. As shown there are no major deviations in the fitted  $R$  values.



Figure 5.35:  $R$  versus energy threshold for the Run 1 precession frequency analysis datasets. The fit points lie in and around the  $1\sigma$  statistical bands.

#### 5.4.4 Fits to bunch number

As described in Section 2.3, eight distinct and separate bunches of muons are sent to the E989 experiment within the accelerator timing structure. If different bunches have different momentum spreads due to how the particles are transported down the various beamlines and injected into the storage ring, then muons might live for different times and therefore their spins might precess more or less within the magnetic field. This difference in  $g - 2$  phase between the different bunches would then affect the final fitted  $R$  value, and might be a systematic error in the precession frequency measurement if certain bunches have significantly more statistics than the others. In order to check if there were any differences in the final fitted  $R$  values per bunch, the bunches were fit individually. Figure 5.36 shows the fitted  $R$  values for the eight individual bunches alongside the bunch-sum result, for the Run 1 precession frequency analysis datasets. In all cases there appear no systematically different  $R$  values per bunch. When the eight individual bunches were fit to a straight line, they were found to be very consistent with the bunch-sum result.



Figure 5·36:  $R$  versus bunch number for the Run 1 precession frequency analysis datasets. Bunch number 0 corresponds to the data from all bunches added together. The blue dashed line intersects the bunch number 0 point, and its value is displayed in the top left of each plot. The red line corresponds to a fit to bunches 1–8, with  $p_0$  being the fit parameter. In all cases the fitted  $R$  value to bunches 1–8 is well within  $1\sigma$  of the all-bunches result.

Random Seed Fit Results				
Dataset	$\chi^2$ Mean	$R$ Mean (ppm)	$R$ RMS (ppb)	$R$ Error on Mean (ppb)
60h	0.999	-20.556	344.3	48.7
HighKick	1.001	-17.475	422.6	59.8
9d	0.999	-17.718	211.8	30.0
Endgame	1.002	-17.341	124.9	17.7

Table 5.7: Random seed fit results to the four Run 1 precession frequency analysis datasets. The  $\chi^2$  means are consistent with 1. As a reminder the 60h dataset used a different blinding than the other three, hence the significantly different  $R$  mean. **I have ppm and ppb here in this table, should I make them all ppm?**

#### 5.4.5 Fits to many random seeds

While the single seed fit results presented earlier indicate good fits and well understood parameters, it is always a good idea to fit other random seeds in case the single seed results ended up on an outlier. Doing so not only improves the confidence of the result, but also gives a more central  $R$  value to quote as being closer to the ‘true’  $R$  of the dataset. Figures 5.37 and 5.38 give the  $\chi^2$  and  $R$  distributions for fits to 50 different random seeds for the four datasets. As shown the  $\chi^2$  distributions are nicely centered around 1 as they should be for fits to the properly distributed data. Table 5.7 compares the random seed fit results between the different datasets.

The means for the  $R$  distributions of the datasets which shared the same blinding string {HighKick, 9d, Endgame} are close but not quite consistent when accounting for the error on the mean, calculated as

$$\sigma_\mu = \text{RMS}/\sqrt{N}, \quad (5.32)$$

where  $N$  is the number of random seeds. This inconsistency is on the order of couple hundreds of ppb or up to  $10 - 20\sigma$  in the mean error. This is very likely attributable to different field conditions over the course of Run 1.



Figure 5.37:  $\chi^2$ 's for fits to 50 different random seeds for the Run 1 precession frequency analysis datasets. The distributions are nicely centered around 1 which is to be expected if the randomized data is properly distributed and fit correctly.



Figure 5.38:  $R$  values for fits to 50 different random seeds for the Run 1 precession frequency analysis datasets. The statistics box has units of ppm for the mean and RMS of the distributions.

$\omega_a$ Measurement Uncertainties	
Source of uncertainty	E989 Goal (ppb)
Gain changes	20
Pileup	40
Lost muons	20
CBO	30
E field and pitch corrections	30
Quadrature sum	70

Table 5.8: Systematic errors in the precession frequency measurement.  
**fill this table out more once I've gone through the various parts - mention that this is the final expected table**

## 5.5 Systematic errors

### 5.5.1 Pileup systematic errors

As described in Section 5.2.1, the pileup background oscillates at  $\omega_a$  which by extension means a strong effect on the final fitted  $R$  value. If the subtracted pileup spectrum is misconstrued in any way, there will be a systematic error on  $R$ . In general the pileup systematic error can be separated into two parts, the error on the amplitude and the error on the phase. In order to estimate the two parts, the uncertainties on the pileup amplitude and phase need to be estimated along with the sensitivities of  $R$  to them. Table 5.1 gives the default values used for the pileup construction parameters {ADT, SDT, SGT, C}. How these parameters feed into the amplitude and phase systematic errors will be discussed in turn, and the overall errors calculated for the different Run 1 datasets.

As a reminder the default values used for the ADT and SDT were 5 ns each, and a default automatic pileup amplitude multiplier of  $\sim 1.03$  was applied to the pileup spectra. In order to calculate the systematic dependence on the choice of ADT or SDT, the SDT parameter was scanned over from 5 ns to 10 ns in steps of 1 ns. This was done with and without the same automatic pileup amplitude scaling procedure

as described in Section 5.2.1. The results of the study for the 9d dataset are shown in Figures 5·39 and 5·40. In the case where there was no automatic scaling applied there is a clear minimum in the  $\chi^2$  results and a steep slope in  $R$  corresponding to a large sensitivity of  $R$  to the choice of SDT. In the case where the automatic scaling was applied however, the minimum in the  $\chi^2$  results has disappeared, while the sensitivity of  $R$  has become much reduced to the point of no longer being a clear trend<sup>16</sup>. The fact that applying the automatic pileup amplitude scaling produces nearly identical pileup spectra with no clear trend in  $R$  regardless of the choice of SDT (and by extension ADT), any systematic error due to the choice of these two parameters can be subsumed into the direct pileup amplitude error itself, discussed down below. It should be noted in fact that the choices of ADT and SDT are largely irrelevant barring statistics, as the automatic amplitude scaling procedure can always account for any differences between the two.

In order to calculate the systematic dependence on the choice of SGT (default value of 10 ns), the SGT parameter was scanned over from 10 ns to 20 ns in steps of 1 ns. The results of the study with the automatic pileup amplitude scaling applied is shown in Figure 5·41. Just as in the SDT scan with the automatic pileup amplitude scaling, there is no minimum in the  $\chi^2$  results, the sensitivity of  $R$  to the value of SGT not so clear, and the pileup spectra for the various choices of SGT are nearly identical. Therefore again any systematic error due to the choice of SGT is subsumed into the pileup amplitude error.

The pileup amplitude systematic error is the error on  $R$  assuming the scale of the pileup was incorrectly constructed. In order to evaluate this error, multipliers were applied to the pileup spectra from 0.9 to 1.1 in steps of 0.01 (dropping the default automatic pileup scaling of  $\sim 1.03$  mentioned before). The data was then re-fit to find

---

<sup>16</sup>This slope in  $R$  varies between positive and negative values based on dataset, so there is no real clear trend in  $R$ .

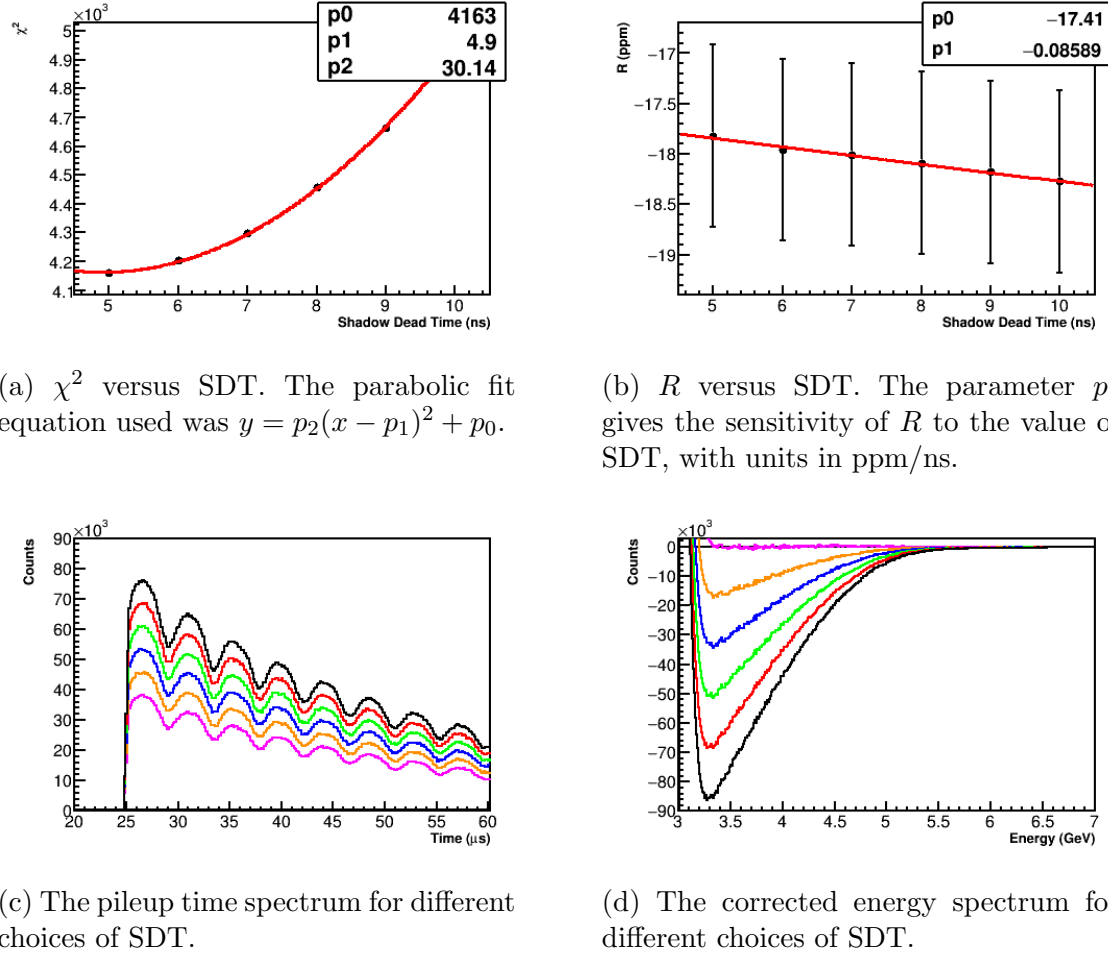


Figure 5.39: Shadow dead time scan results without automatic pileup amplitude scaling. A clear minimum in the  $\chi^2$  plot is seen near 5 ns corresponding to the choice of ADT, and a large sensitivity for  $R$  is observed. In the bottom two spectra plots the magenta curve corresponds to a choice SDT = 5 ns while the black curve corresponds to SDT = 10 ns. The larger choice of SDT leads to a greater estimation of the pileup, which as shown in the energy spectra plot leads to a corresponding over-subtraction at energies where hits consist mostly or purely of pileup pulses. Data from 9d dataset.

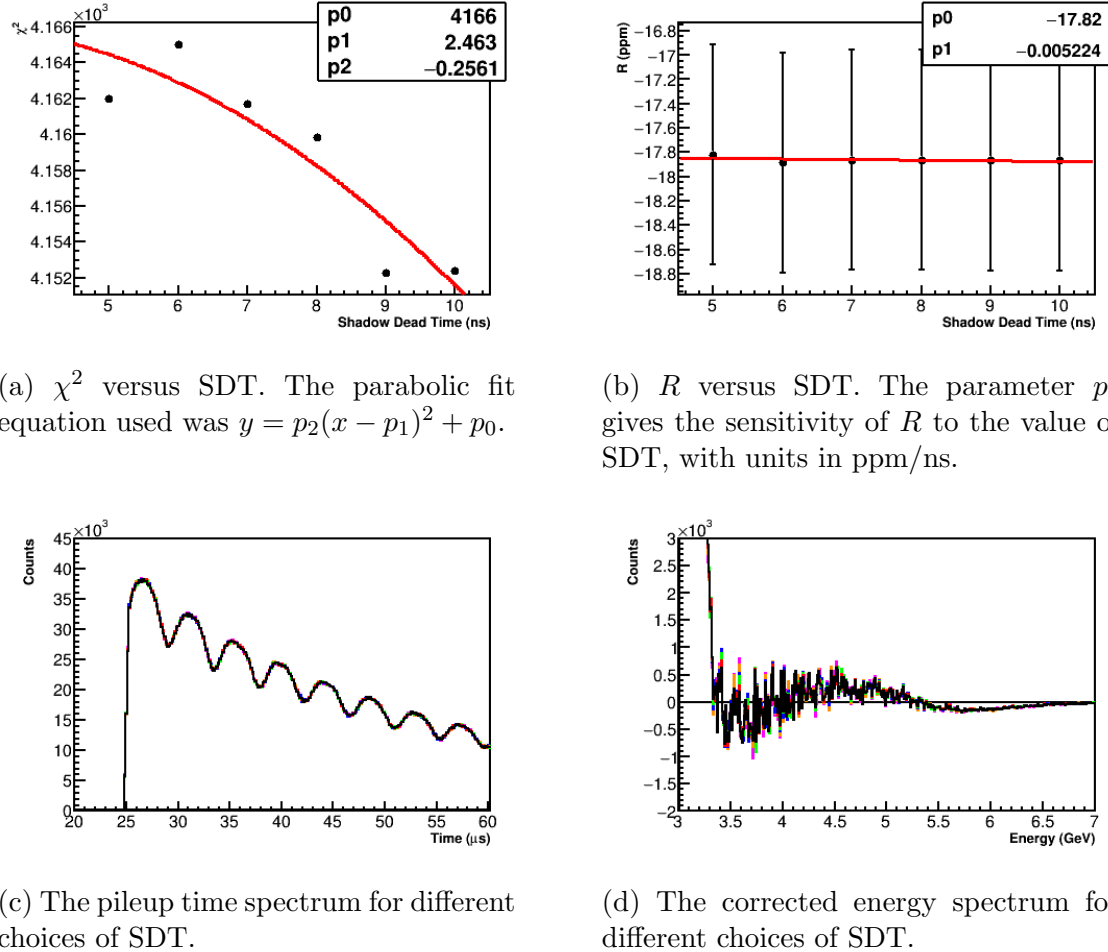
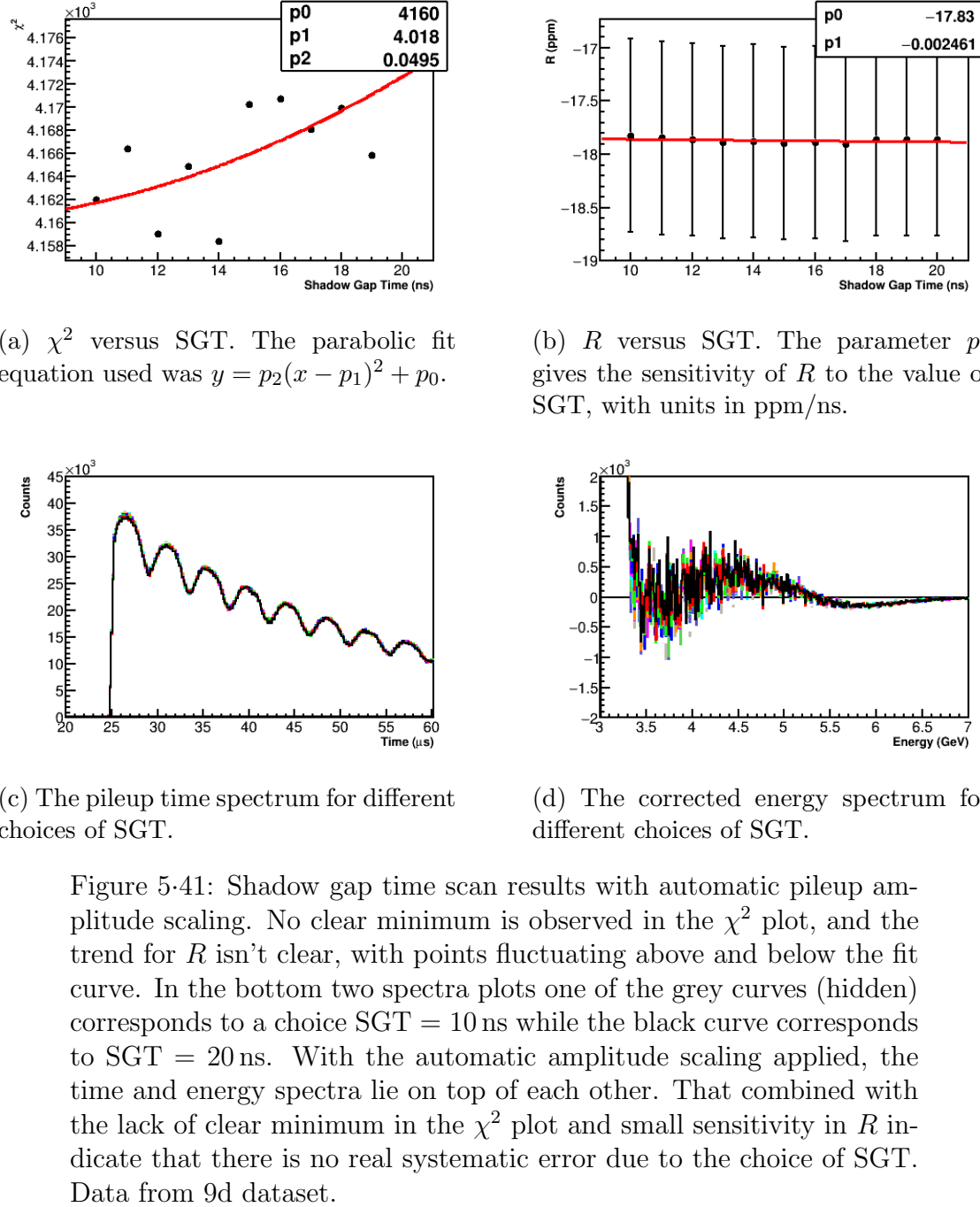


Figure 5.40: Shadow dead time scan results with automatic pileup amplitude scaling. No clear minimum is observed in the  $\chi^2$  plot, and the sensitivity for  $R$  is small. In the bottom two spectra plots the magenta curve corresponds to a choice  $SDT = 5\text{ ns}$  while the black curve corresponds to  $SDT = 10\text{ ns}$ . With the automatic amplitude scaling applied, the time and energy spectra are nearly identical and lie on top of each other. That combined with the lack of clear minimum in the  $\chi^2$  plot and no clear sensitivity in  $R$  indicate that there is no real systematic error due to the choice of SDT. Data from 9d dataset.



the change in  $R$ . The results of the study for the 9d dataset are shown in Figure 5.42. As shown there is a clear minimum near 1 in the  $\chi^2$  results and a large sensitivity of  $R$  to the multiplier. The systematic error on  $R$  is calculated as

$$\delta R = \sigma_{P_m} \times \frac{dR}{dP_m}, \quad (5.33)$$

where  $P_m$  is the value of the pileup multiplier. The error  $\sigma_{P_m}$  is calculated as the width of the fitted parabola in the  $\chi^2$  plot, defined as the change in  $P_m$  from the minimum for the  $\chi^2$  to increase by 1. This is calculated as

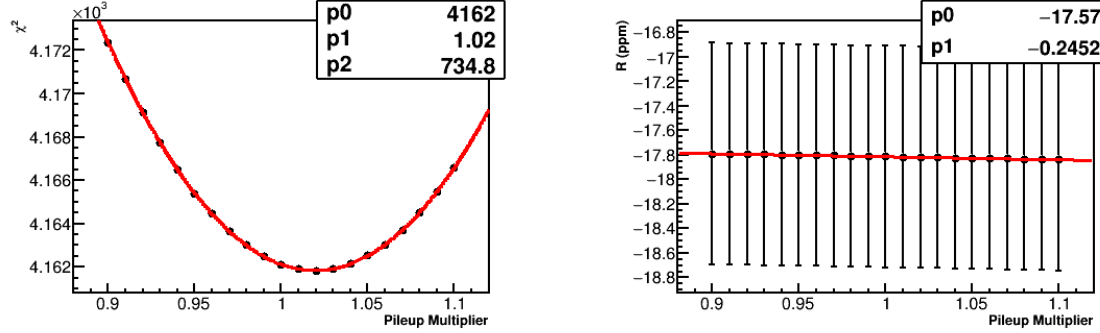
$$\sigma_{P_m} = \sqrt{\frac{2}{f''(\chi^2)}} = \frac{1}{\sqrt{p_2}}, \quad (5.34)$$

where  $p_2$  is the fit parameter as given in the top right of the  $\chi^2$  plot. The sensitivities of  $R$  to the pileup multiplier, uncertainties in the pileup amplitude, and final corresponding systematic errors for the Run 1 precession frequency analysis datasets are given in Table 5.9. As shown in the table, the uncertainties on the pileup amplitude are of order 2 to 5%, while the systematic errors on  $R$  are on the order of 10 to 20 ppb depending on dataset. It should be noted that the default automatic pileup multiplier of  $\sim 1.03$  does not necessarily correspond to the minimum in the  $\chi^2$  plot, but is within  $1\sigma$  of 1 or the minimum (except the Endgame which is closer to  $2\sigma$ )<sup>17</sup>.

The pileup phase error is the error on  $R$  assuming the phase of the pileup was incorrectly constructed. This is separated into two parts. The first part is calculated by applying time-shifts to  $t_{\text{doublet}}$  as given in Equation 5.2. Doing this artificially applies a phase shift to the pileup time spectrum. The data is then re-fit with the different pileup spectra and the change in  $R$  is calculated. Figure 5.43 shows the study results for the 9d dataset with time-shifts applied between  $-10$  ns and  $10$  ns in

---

<sup>17</sup>Monte-Carlo tests with various random seeds showed this minimum fluctuating above and below 1. The distance from 1 therefore is not a good measure for the uncertainty in the pileup amplitude compared to the width of the  $\chi^2$  parabola fit.



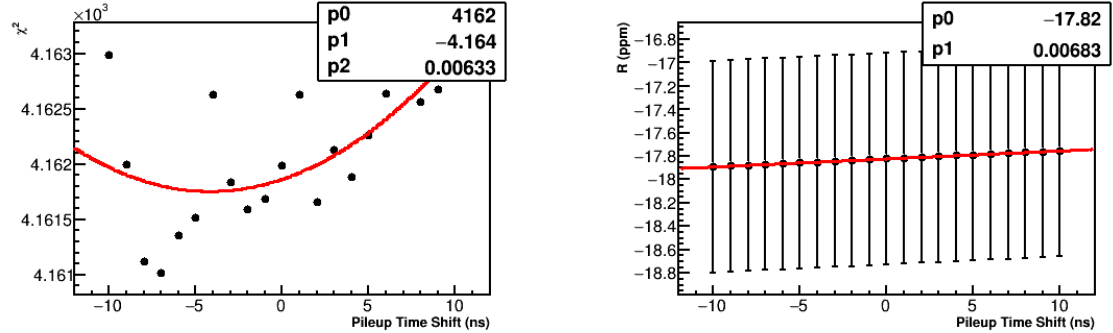
(a)  $\chi^2$  versus pileup multiplier. The parabolic fit equation used was  $y = p_2(x - p_1)^2 + p_0$ .

(b)  $R$  versus pileup multiplier. The parameter  $p_1$  gives the sensitivity of  $R$  to the value of the pileup multiplier, with units in ppm.

Figure 5.42: Pileup multiplier scan. Data from 9d dataset.

Systematic Error due to Pileup Amplitude				
Dataset	$dR/dP_m$	$\sigma_{P_m}$	$P_{m_{\min}}$	$\delta R$
60h	-419.3	0.053	0.993	<b>22.2</b>
HighKick	-372.8	0.051	0.997	<b>19.0</b>
9d	-245.2	0.037	1.020	<b>9.0</b>
Endgame	-335.3	0.028	0.985	<b>9.4</b>

Table 5.9: Systematic error due to the pileup amplitude in the Ratio Method fits for the Run 1 precession frequency analysis datasets. The bold column gives the systematic error on  $R$ . Units for  $dR/dP_m$  and  $\delta R$  are in ppb.



(a)  $\chi^2$  versus pileup time-shift. There is no clear minimum in the plot.

(b)  $R$  versus pileup time-shift. The parameter  $p_1$  gives the sensitivity of  $R$  to the value of the pile time-shift, with units in ppm/ns.

Figure 5.43: Scan over pileup time-shift. Data from 9d dataset.

steps of 1 ns. A clear sensitivity of  $R$  to the value of time-shift is observed, however there is no clear minimum in the  $\chi^2$  results. Because the width of the  $\chi^2$  parabolic fit cannot be taken as the uncertainty in the pileup time-shift parameter , instead the uncertainty is taken conservatively at half the ADT at 2.5 ns. The systematic error is calculated in the same way as for the pileup amplitude uncertainty,

$$\delta R = \sigma_{P_t} \times \frac{dR}{dP_t}, \quad (5.35)$$

where  $P_t$  is the value of the pileup time-shift. The sensitivities of  $R$  to the pileup time-shift and corresponding systematic errors for the Run 1 precession frequency analysis datasets are given in Table 5.10.

The second part of the pileup phase error comes from the choice of constant  $C$  in the calculation of  $E_{\text{doublet}}$  as given in Equation 5.1. If the energy of the pileup pulses are systematically misconstrued, then pileup shadow doublets will be added or lost near the applied energy threshold when constructing the pileup spectrum. This leads to an error on the pileup phase since it is energy-dependent. In order to calculate

<b>Systematic Error due to Pileup Time Shift</b>		
Dataset	$dR/dP_t$	$\delta R$
60h	7.0	<b>17.6</b>
HighKick	7.6	<b>19.0</b>
9d	6.8	<b>17.1</b>
Endgame	5.7	<b>14.3</b>

Table 5.10: Systematic error due to the pileup time-shift parameter  $P_t$  in the Ratio Method fits for the Run 1 precession frequency analysis datasets. The bold column gives the systematic error on  $R$ . Units for  $dR/dP_t$  and  $\delta R$  are in ppb/ns and ppb respectively. The error on the  $P_t$  is by default taken to be 2.5 ns as described in the text. **fix spacing of table**

the systematic error from the energy construction, the parameter  $C$  was scanned over from 0.9 to 1.1, in steps of 0.01. The results of the study for the 9d dataset are shown in Figure 5.44. The systematic error on  $R$  is calculated as

$$\delta R = \sigma_C \times \frac{dR}{dC}. \quad (5.36)$$

Similarly to the pileup amplitude error, there is a clear minimum in the  $\chi^2$  results which can be used to estimate the uncertainty in the pileup energy scale<sup>18</sup>. Table 5.11 gives the sensitivities of  $R$  to the pileup energy scale, uncertainties in the pileup energy scale, and the corresponding final systematic errors for the Run 1 precession frequency analysis datasets. As shown the uncertainties on the pileup energy scale are of order 1 to 2%, and the value for  $C$  which produces the minimum in the  $\chi^2$  results is consistent with 1<sup>19</sup>. Interestingly, the sensitivity of  $R$  to  $C$  in the 60h dataset is noticeably larger than in the rest of the datasets, though the origin of this is currently unknown. **what to do about this?**

Table 5.12 gives the quadrature sum for the total pileup systematic errors for the

---

<sup>18</sup>The trend isn't as clean as in the scan over the pileup amplitude multiplier, but that is acceptable.

<sup>19</sup>Because the spatial separation is turned off in the clustering portion of the reconstruction, a value of  $C = 1$  is to be expected.



(a)  $\chi^2$  versus pileup energy scale. The parabolic fit equation used was  $y = p_2(x - p_1)^2 + p_0$ .

(b)  $R$  versus  $C$ . The parameter  $p_1$  gives the sensitivity of  $R$  to the value of  $C$ , with units in ppm.

Figure 5.44: Scan over pileup energy scale. Data from 9d dataset.

Systematic Error due to Pileup Energy Scale				
Dataset	$dR/dC$	$\sigma_C$	$C_{\min}$	$\delta R$
60h	-835.1	0.023	0.997	<b>19.4</b>
HighKick	-167.7	0.022	0.995	<b>3.7</b>
9d	-332.0	0.016	1.000	<b>5.5</b>
Endgame	-431.4	0.012	0.982	<b>5.3</b>

Table 5.11: Systematic error due to the fixed pileup energy scale parameter  $C$  in the Ratio Method fits for the Run 1 precession frequency analysis. The bold column gives the systematic error on  $R$ . Units for  $dR/dC$  and  $\delta R$  are in ppb.

<b>Total Pileup Systematic Errors</b>					
Type of Error	Parameter	60h	HighKick	9d	Endgame
Amplitude	$P_m$	22.2	19.0	9.0	9.4
Phase	$P_t$	17.6	19.0	17.1	14.3
Phase	$C$	19.4	3.7	5.5	5.3
Quadrature sum		34.3	27.1	20.1	17.9

Table 5.12: Total pileup systematic errors for the Run 1 precession frequency analysis datasets.

Run 1 precession frequency analysis datasets. As shown for each dataset the total error is below the target final error of 40 ppb in spite of the contamination in the pileup shadow method. For future runs of the experiment with increased rate and therefore increased pileup, these errors may grow. In that case either the pileup shadow method might need to be improved to account for the contamination and pileup triplets, or discarded in favor of a different method.

### 5.5.2 Gain systematic errors

-talk about the equations here - slight reference to either detector section or reconstruction section in this chapter - might want to put this after pileup if I introduce various equations and the like in that section

### 5.5.3 CBO systematic errors

### 5.5.4 Lost muon systematic errors

As mentioned in Section 5.3.3, the triples spectrum is made with cuts as defined in Table 5.4. Various backgrounds are subtracted off the triples spectrum in order to generate a clean sample of lost muons. Table 5.13 gives the change in  $R$  for various sets of cuts and background subtractions for the 9d and Endgame datasets. As shown the various different backgrounds and cuts ultimately make very little difference in the final fitted  $R$  value. Similarly, stable beam contaminants in the form of deuterons

<b><math>\Delta R</math> with Various Lost Muon Cuts</b>				
Type of fit or cut	9d Dataset		Endgame Dataset	
	$\Delta R$ (ppb)	$\kappa_{loss}$	$\Delta R$ (ppb)	$\kappa_{loss}$
No quadruple subtraction	0.2	1.811	-0.1	1.717
No accidental subtraction	0.1	2.503	< 0.1	2.339
$\Delta t_{13} \leq 12.5$ ns	0.1	4.469	-0.3	4.248
$5$ ns $\leq \Delta t_{12,23} \leq 8.5$ ns	N/A	N/A	< 0.1	1.709
$100$ MeV $\leq E_{1,2,3} \leq 500$ MeV	N/A	N/A	< 0.1	2.09

Table 5.13: Effect on the fitted  $R$  value in the 9d and Endgame datasets with various different cuts used or backgrounds subtracted. Ultimately how the muon loss spectrum  $L(t)$  is created has little bearing on the final fitted  $R$  value. Also included are the various corresponding  $\kappa_{loss}$  values which compensate for the level of statistics contained within  $L(t)$  due to the various cuts. **decide whether to fill out the N/A 9d fits or not**

and protons contaminate the lost muon spectrum. The former are largely removed by straightforward  $\Delta t_{12}$  and  $\Delta t_{13}$  cuts. The latter can be mostly removed by cutting on the negative side of the  $\Delta t_{13}$  distribution which separates the populations more readily, Figure 5.45, with  $\Delta t_{13} \leq 12.5$  ns. While this does largely remove the protons at the cost of statistics, the fitted  $\kappa_{loss}$  parameter simply grows larger to compensate. Ultimately the effect on  $R$  is negligible, with  $\Delta R = -0.3$  ppb. The sum of these separate types of errors is conservatively taken at 1 ppb for all datasets<sup>20</sup>.

Of more interest is the choice of fixed value for the  $\kappa_{loss}$  parameter in the ratio fits, fixed from the corresponding T-Method fits. The systematic error can be determined by simply scanning over the value of  $\kappa_{loss}$  as in Figure 5.46, where the error on the parameter is that taken from a T-Method fit to the same data<sup>21</sup>. Table 5.14 gives the systematic errors on  $R$  for the Run 1 precession frequency analysis datasets. Interestingly enough, though the Endgame dataset has the most lost muons, it is seen

<sup>20</sup>For the T-Method fits, though the changes in  $R$  are noticeably larger with the various cuts, they are still the same order of magnitude and the error is conservatively below 1 ppb.

<sup>21</sup>The size of the error on  $\kappa_{loss}$  is entirely due to statistics.

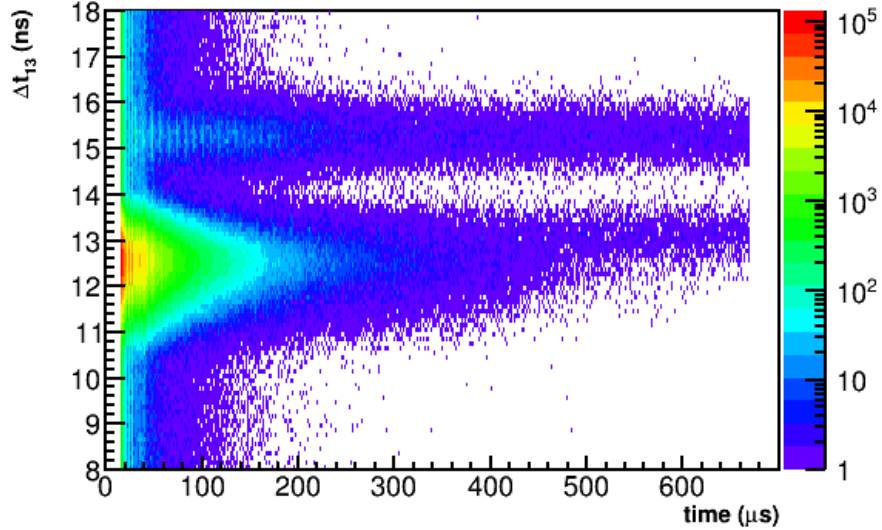


Figure 5.45: Lost muon  $\Delta t_{13}$  distribution as a function of time in-fill.

that the change in  $R$  versus  $\kappa_{loss}$  is larger in the other datasets. This is potentially due to the fact that **try to come up with something for this unless I can explain it away as an oddity.**

- a systematic error comes from the fact that muons are lost preferentially at earlier times (changing over the course of a fill) -if lost muons originate from different points in the beam line, then they will have precessed a different amount leading to a different phase

- this error dominates the uncertainty...

- probably move losses fraction figure to here somewhere

The fractional losses (the integral in Equation 5.28 times the final fitted  $\kappa_{loss}$  parameter) for the Run 1 precession frequency analysis datasets are shown in Figure 5.47.

- also Sudeshna's talk in the Elba collaboration meeting - this probably just for the systematic error

- put in a chart at the end summarizing the total lost muons systematic error - unless I want to keep the pieces separate, and have one giant chart at the end which

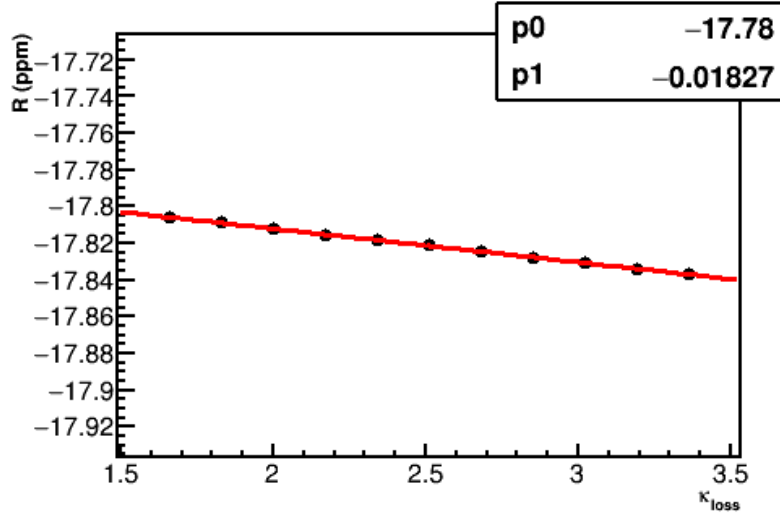


Figure 5.46: The sensitivity of  $R$  to the fixed  $\kappa_{loss}$  parameter. Error bars have been removed from the plot. Units are in ppm, data from the 9d dataset.

Systematic Error due to Fixed $\kappa_{loss}$				
Dataset	$dR/d\kappa_{loss}$	$\sigma_{\kappa_{loss}}$	$\delta R$	$\Delta R$ (with - without)
60h	-3.5	0.338	<b>1.2</b>	-31.4
HighKick	-7.1	0.697	<b>4.9</b>	-40.1
9d	-18.3	0.170	<b>3.1</b>	-45.7
Endgame	-2.6	0.038	<b>0.1</b>	-6.1

Table 5.14: Systematic error due to the fixed  $\kappa_{loss}$  parameter in the Ratio Method fits for the Run 1 precession frequency analysis datasets. The bold column gives the systematic error on  $R$ . The last column on the right gives the change in  $R$  with the lost muons term included versus without, providing an absolute upper bound on systematic error. All units are in ppb except for the  $\sigma_{\kappa_{loss}}$  parameter which is unit-less and comes from the T-Method fits.

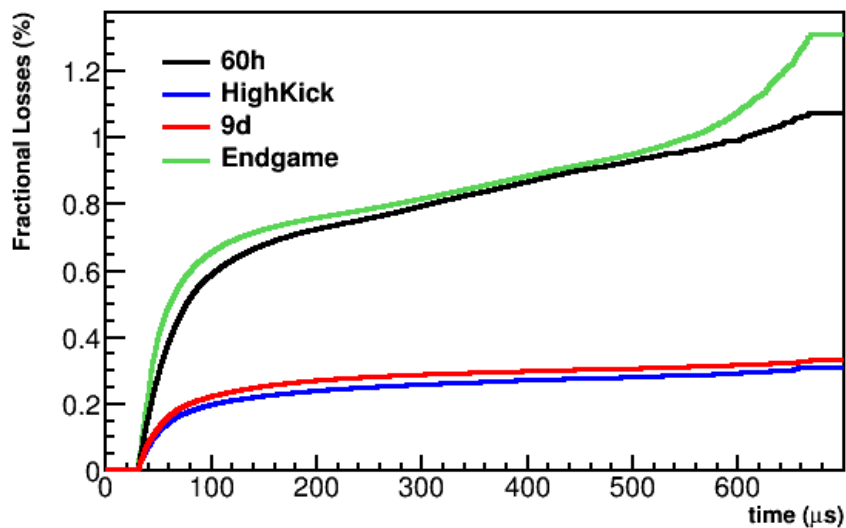


Figure 5.47: Fractional losses for the Run 1 precession frequency analysis datasets. The curves begin at  $30.2\text{ }\mu\text{s}$  which is where the fit begins. A value of 1% at a specific time  $t$  indicates that there are 1% fewer stored muons at that time than there would be if there were no losses at all. The Endgame and 60h datasets can be seen to have the most losses, while the 9d and HighKick have less. This is due to the higher kicks in the latter datasets which put the muon beam on a more central orbit. The upward tail at the end of the Endgame dataset corresponds to the remnant proton contamination.

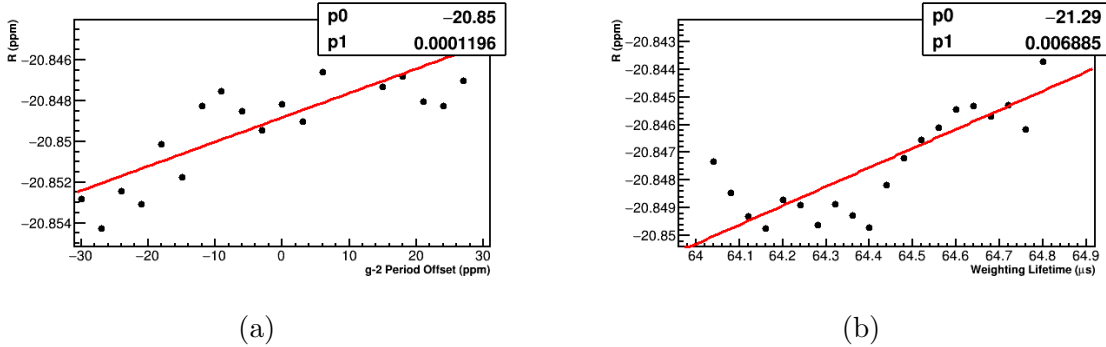


Figure 5.48

Sensitivity to Ratio Construction Parameters		
Dataset	$dR/dT_a$	$dR/d\tau_\mu$
60h	0.1	6.9
HighKick	-0.1	-4.1
9d	< 0.1	-1.1
Endgame	< 0.1	0.6

Table 5.15: units in ppb per... fix spacing of table

might be too much

### 5.5.5 Ratio construction systematic errors

-point out how slopes vary positively and negatively and then claim no real systematic error

### 5.5.6 Binning systematic errors

-for bin edge it was verified that a shift of one bin width returned the same fit results as a shift of 0, that with the negligible slope implies no systematic effect on  $R$

-for the bin width not only do the slopes vary widely when scanning over the different datasets, but upon inspection of the points in the plot there is no clear trend, that combined with the results from blah analysis showing that the optimal bin width is 149.2 ns implies there is no systematic effect on  $R$  - if one wanted to be

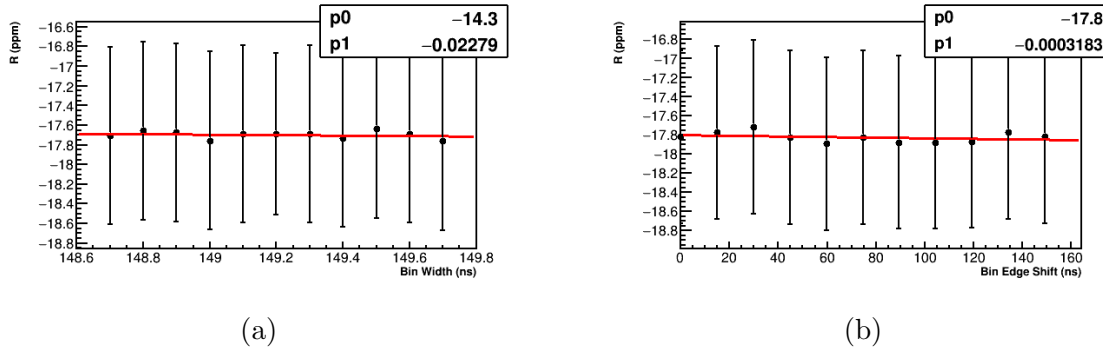


Figure 5.49

Sensitivity to Binning Parameters		
Dataset	$dR/d_{\text{bin width}}$	$dR/d_{\text{bin edge}}$
60h	24.5	-0.1
HighKick	6.0	-0.7
9d	-22.8	-0.3
Endgame	-41.7	-0.6

Table 5.16: units in ppb/ns fix spacing of table

very conservative they could take the uncertainty in the bin width as X ns (probably something like 0.1), and the systematic errors would be absolutely negligible

### 5.5.7 Random seed systematic errors

-not a systematic error per se but ...

### 5.5.8 Systematic error summary

-include here a big table (with each of the individual errors making up say pileup and the like) of all systematic errors

## **Chapter 6**

### **Conclusion**

-calculate what the final weighted statistical error will be approximately

-potentially mention further ongoing dqc work to clean up the datasets before publication

#### **6.1 Run 1 value of $a_\mu$**

## Appendix A

# Straw measurement angular correction

The tracker straws don't measure U and V coordinates directly, but instead measure the DCA radii deriving from measured hit times. In order to utilize the minimization procedure described in Section 4.2.2 on measured track parameters these radii must first be converted to U and V parameters, and similarly for the U and V errors. To first order the measured DCAs can be used identically as the U and V positions, but it was found that there were slight biases in the truth pulls due to this.

In order to improve the results, angular corrections were made to the DCAs to give more accurate estimates of the “measured” positions. It was found that for the error correction, assuming a straight particle path was sufficient for ideal results. For the position correction, it was found that assuming a circular particle path (constant field) correction for the curved tracks was sufficient. These corrections are dependent on the angle of the track, so it's important to note that during each successive iteration of the track fitting, the “measured” parameters are adjusted by the latest “predicted” momenta which change the angle of the track. The correction depends on whether the track went to the left or right side of the wire. Note that the momentum perpendicular to the straw measurement axis can be ignored since it doesn't affect the U or V value. A summary of the calculation of the right side correction follows, with the left side correction being calculated in a similar manner. See Figure A·1.

To solve for the measured U (or V) value, first use the following trigonometric

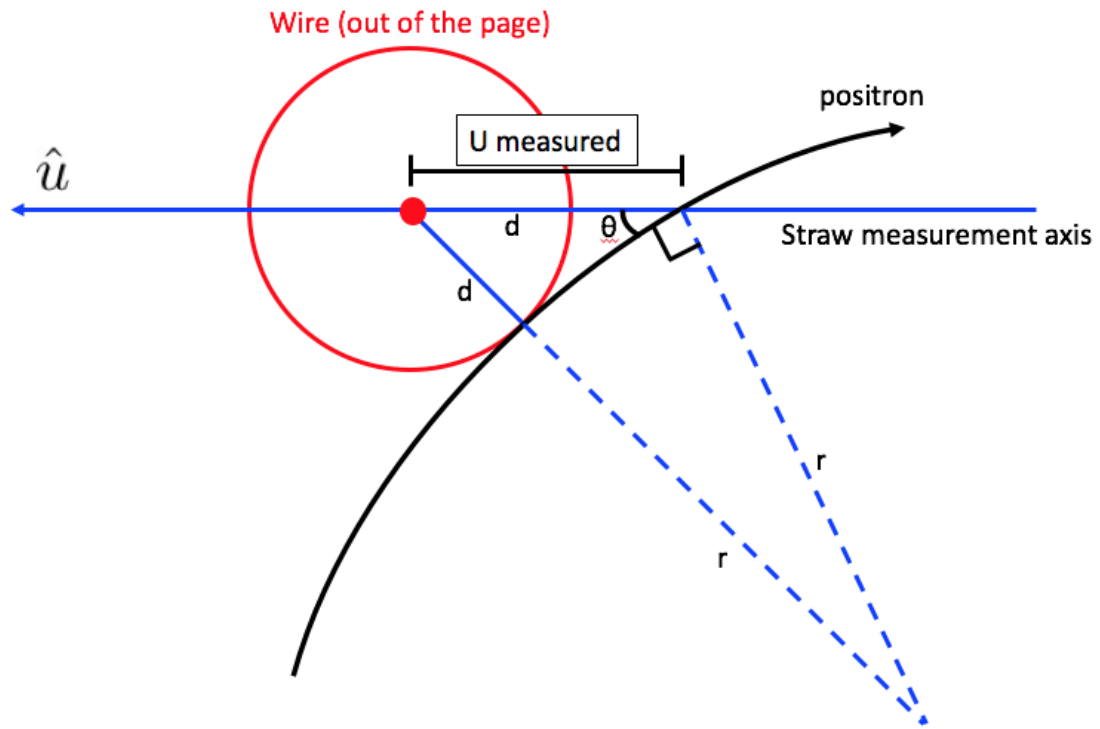


Figure A·1: A positron passing through a straw will produce a hit of radius  $d$ . The desired value is the U or V position along the straw measurement axis. The positron trajectory can be approximated as a circle in a constant magnetic field over the length of the path across the straw. The curvature for the high energy positrons is small such that  $r \gg d$  and the angle between the trajectory and the center of the circle can be approximated as  $90^\circ$ . Sizes and angles are exaggerated. A similar diagram can be drawn for positrons passing to the left of the wire. **Might want to clean up this picture at some point.**

identity:

$$(r + d)^2 = r^2 + u^2 - 2ru \cos(90 + \theta), \quad (\text{A.1})$$

where  $u$  is the parameter of interest. The angle  $\theta$  can be determined from

$$\hat{z}_\parallel \cdot \hat{p}_\parallel = \cos \theta, \quad \theta = \cos^{-1} \frac{p_\parallel}{p}, \quad (\text{A.2})$$

where  $p_\parallel$  is the positron momentum anti-parallel to the U measurement axis at the wire plane. Using some further trigonometric identities and solving for  $u$  gives

$$u = -r \sqrt{1 - \left(\frac{p_\parallel}{p}\right)^2} + \sqrt{d^2 + 2dr + r^2 \left(1 - \left(\frac{p_\parallel}{p}\right)^2\right)}, \quad (\text{A.3})$$

for the right side correction. Similarly,

$$u = +r \sqrt{1 - \left(\frac{p_\parallel}{p}\right)^2} - \sqrt{d^2 + 2dr + r^2 \left(1 - \left(\frac{p_\parallel}{p}\right)^2\right)}, \quad (\text{A.4})$$

for the left side correction. The radius  $r$  can be calculated from the momentum and magnetic field at the predicted hit position, and the momentum components can be determined within the Geant4 simulation. The straightline correction to the errors is done simpler manner using the Pythagorean theorem,

$$\sigma'_{uv} = \frac{\sigma_{uv}}{\sqrt{1 - \left(\frac{p_\parallel}{p}\right)^2}}, \quad (\text{A.5})$$

where  $\sigma'_{uv}$  is the improved error from original U or V error  $\sigma_{uv}$  on the DCA.

# Appendix B

## Ratio Method Derivation

### B.1 Ratio form and function

Consider the 5 parameter function:

$$N_5(t) = N_0 e^{-t/\tau} (1 + A \cos(\omega_a t + \phi)), \quad (\text{B.1})$$

which describes some ideal dataset in histogram format. Here  $\phi$  will be set to zero for simplicity. Now define the variables  $u_+(t)$ ,  $u_-(t)$ ,  $v_1(t)$ , and  $v_2(t)$  as

$$\begin{aligned} u_+(t) &= \frac{1}{4} N_5(t + T/2) \\ u_-(t) &= \frac{1}{4} N_5(t - T/2) \\ v_1(t) &= \frac{1}{4} N_5(t) \\ v_2(t) &= \frac{1}{4} N_5(t), \end{aligned} \quad (\text{B.2})$$

where the  $1/4$  out front reflects randomly splitting the whole dataset into 4 equally weighted sub-datasets, and  $T$  is the g-2 period known to high precision,  $\mathcal{O}(10^{-6})$ . This corresponds to a weighting of 1:1:1:1 between the datasets. To be explicit here regarding the signs, the counts that are filled into the histogram described by  $u_+$  have their times shifted as  $t \rightarrow t - T/2$ , which is what the function  $N_5(t + T/2)$  describes,

and vice versa for  $u_-$ . To form the ratio define the variables:

$$\begin{aligned} U(t) &= u_+(t) + u_-(t) \\ V(t) &= v_1(t) + v_2(t) \\ R(t) &= \frac{V(t) - U(t)}{V(t) + U(t)}. \end{aligned} \tag{B.3}$$

Plugging in and dividing the common terms ( $N_0 e^{-t/\tau}/4$ ),

$$R(t) = \frac{2(1 + A \cos(\omega_a t)) - e^{-T/2\tau}(1 + A \cos(\omega_a t + \omega_a T/2)) - e^{T/2\tau}(1 + A \cos(\omega_a t - \omega_a T/2))}{2(1 + A \cos(\omega_a t)) + e^{-T/2\tau}(1 + A \cos(\omega_a t + \omega_a T/2)) + e^{T/2\tau}(1 + A \cos(\omega_a t + \omega_a T/2))}. \tag{B.4}$$

Now set  $\omega_a T/2 = \delta$ , and note that  $T$  is really

$$\begin{aligned} T &= T_{guess} = \frac{2\pi}{\omega_a} + \Delta T, \\ \Delta T &= T_{guess} - T_{true}. \end{aligned} \tag{B.5}$$

Being explicit,

$$\delta = \frac{\omega_a}{2} T_{guess} = \frac{\omega_a}{2} \left( \frac{2\pi}{\omega_a} + \Delta T \right) = \pi + \pi \frac{\Delta T}{T_{true}} = \pi + \pi(\delta T), \tag{B.6}$$

and  $\delta$  can be redefined as

$$\delta = \pi(\delta T), \tag{B.7}$$

by flipping the sign of any cosine terms that contain  $\delta$ .

Then, using the trig identity

$$\cos(a \pm b) = \cos(a) \cos(b) \mp \sin(a) \sin(b) \tag{B.8}$$

so that

$$\begin{aligned}
\cos(\omega_a t \pm \delta) &= \cos(\omega_a t) \cos \delta \mp \sin(\omega_a t) \sin \delta \\
&\approx \cos(\omega_a t)(1 - \delta^2) \mp \sin(\omega_a t)\delta \\
&\approx \cos(\omega_a t),
\end{aligned} \tag{B.9}$$

since  $\delta \sim O(10^{-5})$ , the ratio becomes

$$R(t) \approx \frac{2(1 + A \cos(\omega_a t)) - (1 - A \cos(\omega_a t))(e^{-T/2\tau} + e^{T/2\tau})}{2(1 + A \cos(\omega_a t)) + (1 - A \cos(\omega_a t))(e^{-T/2\tau} + e^{T/2\tau})}. \tag{B.10}$$

Expanding

$$e^{\pm T/2\tau} = 1 \pm \frac{T}{2\tau} + \frac{1}{2} \left( \frac{T}{2\tau} \right)^2 \pm \dots, \tag{B.11}$$

replacing and simplifying,

$$R(t) \approx \frac{A \cos(\omega_a t) - C(1 - A \cos(\omega_a t))}{1 + C(1 - A \cos(\omega_a t))}, \tag{B.12}$$

where

$$C = \frac{1}{16} \left( \frac{T}{\tau} \right)^2 \approx 2.87 * 10^{-4}. \tag{B.13}$$

Using the expansion

$$f(x) = \frac{1}{1+x} = 1 - x + x^2 - \dots, \quad |x| < 1, \tag{B.14}$$

and since  $C$  is small, the denominator can be manipulated such that

$$\begin{aligned}
R(t) &\approx (A \cos(\omega_a t)) - C(1 - A \cos(\omega_a t))(1 - C(1 - A \cos(\omega_a t))) \\
&\approx A \cos(\omega_a t) - C + CA^2 \cos^2(\omega_a t),
\end{aligned} \tag{B.15}$$

after dropping terms of  $\mathcal{O}(C^2)$  and higher. In practice the last term is omitted since

it has a minimal effect on the fitted value of  $\omega_a$  [89], and one arrives at

$$R(t) \approx A \cos(\omega_a t) - C, \quad (\text{B.16})$$

the conventional 3 parameter ratio function.

In order to avoid approximations one can instead weight the counts in the histograms as

$$u_+(t) : u_-(t) : v_1(t) : v_2(t) = e^{T/2\tau} : e^{-T/2\tau} : 1 : 1, \quad (\text{B.17})$$

so that

$$\begin{aligned} u_+(t) &= \frac{e^{T/2\tau}}{2 + e^{T/2\tau} + e^{-T/2\tau}} N_5(t + T/2) \\ u_-(t) &= \frac{e^{-T/2\tau}}{2 + e^{T/2\tau} + e^{-T/2\tau}} N_5(t - T/2) \\ v_1(t) &= \frac{1}{2 + e^{T/2\tau} + e^{-T/2\tau}} N_5(t) \\ v_2(t) &= \frac{1}{2 + e^{T/2\tau} + e^{-T/2\tau}} N_5(t). \end{aligned} \quad (\text{B.18})$$

(These factors out front aren't so far off from 1/4 since  $e^{\pm T/2\tau} \approx e^{\pm 4.35/2*64.4} \approx 1.034, .967$ .) Then instead  $R(t)$  becomes

$$R(t) = \frac{2(1 + A \cos(\omega_a t)) - (1 - A \cos(\omega_a t + \delta)) - (1 - A \cos(\omega_a t - \delta))}{2(1 + A \cos(\omega_a t)) + (1 - A \cos(\omega_a t + \delta)) + (1 - A \cos(\omega_a t - \delta))}, \quad (\text{B.19})$$

where the  $e^{\pm T/2\tau}$  terms out front now cancel. Using Equation B.9 again and this time avoiding approximations in  $\delta$ ,

$$R(t) = \frac{2A \cos(\omega_a t)(1 + \cos \delta)}{4 + 2A \cos(\omega_a t)(1 - \cos \delta)}, \quad (\text{B.20})$$

after simplifying. In the limit that

$$\delta = \pi(\delta T) \rightarrow 0 \quad (\text{B.21})$$

since  $\delta T$  is small,

$$R(t) \approx A \cos(\omega_a t), \quad (\text{B.22})$$

with the only approximation being made at  $\mathcal{O}(\delta^2) \sim \mathcal{O}(10^{-10})$ .

Finally, while the 3 parameter ratio function suffices for fits to data containing slow modulations, it does not suffice for faster oscillation features. In that case it is more useful to fit with the non-approximated or simplified version of the ratio,

$$\begin{aligned} R(t) &= \frac{v_1(t) + v_2(t) - u_+(t) - u_-(t)}{v_1(t) + v_2(t) + u_+(t) + u_-(t)}, \\ &= \frac{2f(t) - f_+(t) - f_-(t)}{2f(t) + f_+(t) + f_-(t)}, \end{aligned} \quad (\text{B.23})$$

where

$$\begin{aligned} f(t) &= C(t)(1 + A \cos(\omega_a t + \phi)) \\ f_{\pm}(t) &= f(t \pm T_a/2), \end{aligned} \quad (\text{B.24})$$

and  $C(t)$  can encode any other effects in the data that need to be fitted for, such as the CBO,

$$C(t) = 1 + A_{cbo} \cdot e^{-t/\tau_{cbo}} \cdot \cos(\omega_{cbo}t + \phi_{cbo}). \quad (\text{B.25})$$

Additionally, any other fit parameters such as  $A$  or  $\phi$  can be made a function of  $t$ . Using the non-approximated form for the final fit function gives greater confidence in the fit results for the high precision  $\omega_a$  extraction necessary for the experimental measurement.

## B.2 Ratio errors

In order to determine the errors on the points in the formed ratio, Equation B.3, we use standard error propagation:

$$\sigma_R(t)^2 = \left( \frac{\partial R(t)}{\partial V(t)} \right)^2 \delta V(t)^2 + \left( \frac{\partial R(t)}{\partial U(t)} \right)^2 \delta U(t)^2 \quad (\text{B.26})$$

This works because  $V(t)$  and  $U(t)$  are statistically independent datasets. Using standard error propagation again,

$$\begin{aligned} \delta V(t)^2 &= \delta v_1(t)^2 + \delta v_2(t)^2 = v_1(t) + v_2(t) = V(t), \\ \delta U(t)^2 &= \delta u_+(t)^2 + \delta u_-(t)^2 = u_+(t) + u_-(t) = U(t). \end{aligned} \quad (\text{B.27})$$

Calculating out and simplifying the partial derivatives, (and this time dropping the  $t$ 's),

$$\begin{aligned} \frac{\partial R}{\partial V} &= \frac{2U}{(V+U)^2}, \\ \frac{\partial R}{\partial U} &= \frac{-2V}{(V+U)^2}. \end{aligned} \quad (\text{B.28})$$

Combining and simplifying, we arrive at the error formula:

$$\sigma_R^2 = \frac{4UV}{(V+U)^3} = \frac{1-R^2}{(V+U)} \quad (\text{B.29})$$

## Appendix C

# Pileup Modified Errors

In the pileup subtraction method detailed in Section 5.2.1, pileup events are statistically constructed and then subtracted from the data. Because of this, the errors on the bins need to be adjusted appropriately. Reference [101] describes the modified errors, but is not quite correct. Here is provided an improved calculation that is easier to understand. While we are mainly interested in the errors on the histogram bins after pileup subtraction, it first helps to examine the errors of the pileup histogram itself. Here we only consider doublets.

In the asymmetric shadow window pileup method, shadow doublets are constructed from two singlets. The pileup histogram is then filled as the sum of the doublets minus the singlets,

$$P = D - S, \tag{C.1}$$

where  $D$  or  $S$  are only added or subtracted when they are above some energy threshold. If the threshold is set to zero, then for every doublet one entry will be added and two will be subtracted. Since these entries are exactly correlated, the error in each time bin will be

$$\sigma_P = \sqrt{N_D}, \tag{C.2}$$

where  $N_D$  is the number of doublets in that time bin. If the energy threshold is above zero, then we can determine whether the counts in the pileup histogram increase or

	$E_1 < E_{th}$	$E_1 > E_{th}$
$E_2 < E_{th}$	$N_1(+1)$	$N_2(0)$
$E_2 > E_{th}$	$N_3(0)$	$N_4(-1)$

Table C.1: Table of doublets above threshold. Here  $E_1$  and  $E_2$  are the energies of the two singlets,  $E_{th}$  is the energy threshold, and  $N_i$  are the number of doublets above threshold for the different combinations of  $E_1$  and  $E_2$ . ( $N_1$  is assumed above threshold here.) The numbers in the parentheses indicate the number of counts gained or lost in the pileup histogram.

decrease based on whether the singlets and doublets are above threshold or not. Table C.1 shows the different combinations of counts put into the pileup histogram. The counts that go into  $P$  will be

$$\begin{aligned}
 P &= \sum_i N_i - \text{singlets above threshold} \\
 &= (N_1 + N_2 + N_3 + N_4) - (N_2 + N_4) - (N_3 + N_4) \\
 &= N_1 - N_4
 \end{aligned} \tag{C.3}$$

and the errors are

$$\sigma_P = \sqrt{N_1 + N_4}. \tag{C.4}$$

Consider the individual cases: In the cases for  $N_1$ , you will gain a count from the doublet above threshold, and lose no counts since both singlets are below threshold. In the cases for  $N_2$  and  $N_3$ , you will gain a count from the doublet, and lose a count from one of the singlets which is above threshold. In the cases for  $N_4$ , you will gain a count from the doublet and lose two counts from the singlets which are both above threshold. Since the doublet and singlets are exactly correlated, the  $N_1$  and  $N_4$  cases naturally result in a single weight being added into the error, while the  $N_2$  and  $N_3$  cases result in no additions to the error.

Consider now the pileup subtracted time spectrum? The corrected spectrum can be written as

$$N_{\text{corrected}} = N_{\text{measured}} - P. \quad (\text{C.5})$$

The content in  $N_{\text{measured}}$  doesn't matter exactly. What matters is what is in  $N_{\text{measured}}$  that is also within  $P$ , for that is where the correlations come from. Since  $N_{\text{measured}}$  is the sum of all singlets above threshold, we can write it as

$$N_{\text{measured}} = N_{\text{other}} + N_2 + N_3 + 2N_4 \quad (\text{C.6})$$

since we know that those cases  $N_i$  listed come from singlets above threshold, and  $N_{\text{other}}$  is anything in the measured hits that was not included in the pileup shadow construction. We can then replace  $P$  and simplify to get

$$N_{\text{corrected}} = N_{\text{other}} - N_1 + N_2 + N_3 + 3N_4. \quad (\text{C.7})$$

The error on the corrected histogram is then

$$\sigma_{N_{\text{corrected}}} = \sqrt{N_{\text{other}} + N_1 + N_2 + N_3 + 9N_4}. \quad (\text{C.8})$$

Replacing  $N_{\text{other}}$  as

$$N_{\text{other}} = N_{\text{corrected}} + N_1 - N_2 - N_3 - 3N_4, \quad (\text{C.9})$$

we can remove the dependence of the corrected histogram errors on the unknown quantity and arrive at

$$\begin{aligned} \sigma_{N_{\text{corrected}}} &= \sqrt{N_{\text{corrected}} + 2N_1 + 6N_4}, \\ &= \sqrt{N_{\text{corrected}}} \cdot \sqrt{1 + (2N_1 + 6N_4)/N_{\text{corrected}}}. \end{aligned} \quad (\text{C.10})$$

(This argument might seem circular at the end, but it works because of the squaring that occurs when calculating the error.) In the end we have a form for the bin errors of the pileup corrected histogram which only depend on  $N_1$  and  $N_4$  in addition to the number of counts in the corrected histogram. As shown it can be refactored into a form equal to the naive errors (just the bin content) times some correction factor. Since  $N_1$  and  $N_4$  are much smaller than  $N_{\text{corrected}}$  at all times, and because they decay away at about twice the rate as the pileup diminishes, the change to the errors is small, of the order 1 or 2% at 30  $\mu\text{s}$ .

## C.1 Pileup errors for the ratio function

Equation C.10 applies to the corrected errors for a pileup subtracted histogram, but what about the modifications to the ratio errors? If we parameterize that equation as

$$\sigma_{N_{\text{corrected}}} = \sqrt{N_{\text{corrected}}} \cdot \sqrt{\gamma(t)}, \quad (\text{C.11})$$

where the correction factor  $\gamma(t) \approx \gamma e^{-t/\tau_\mu}$  is small and decays at approximately the muon lifetime, we can recast the errors on the individual ratio sub-datasets as

$$\begin{aligned} \delta V(t)^2 &= \delta v_1(t)^2 \cdot \gamma(t) + \delta v_2(t)^2 \cdot \gamma(t) = (v_1(t) + v_2(t)) \cdot \gamma(t) = V(t) \cdot \gamma(t), \\ \delta U(t)^2 &= \delta u_+(t)^2 \cdot \gamma(t + T/2) + \delta u_-(t)^2 \cdot \gamma(t - T/2) \\ &\approx u_+(t) \cdot \gamma(t) e^{-T/2\tau} + u_-(t) \cdot \gamma(t) e^{+T/2\tau} \\ &\approx (u_+(t) + u_-(t)) \cdot \gamma(t) \cdot \left(1 + \frac{1}{2} \left(\frac{T}{2\tau}\right)^2\right) \\ &\approx U(t) \cdot \gamma(t), \end{aligned} \quad (\text{C.12})$$

where in the last step the  $\frac{1}{2} \left(\frac{T}{2\tau}\right)^2$  term has been neglected because it's small. With these approximations having been made, the modified errors on the ratio points simply

become

$$\sigma_R^2 \rightarrow \sigma_R^2 \cdot \gamma(t), \quad (\text{C.13})$$

with the correction being the same as that on the pileup subtracted histogram. Credit to Reference [90] for this derivation.

## **Appendix D**

### **Fit Result Correlation Matrices**

Correlation matrices for the HighKick, 9d, and Endgame datasets. It was found that there were stronger correlations between higher order CBO parameters in HighKick and 9d datasets than in the 60h and Endgame datasets..

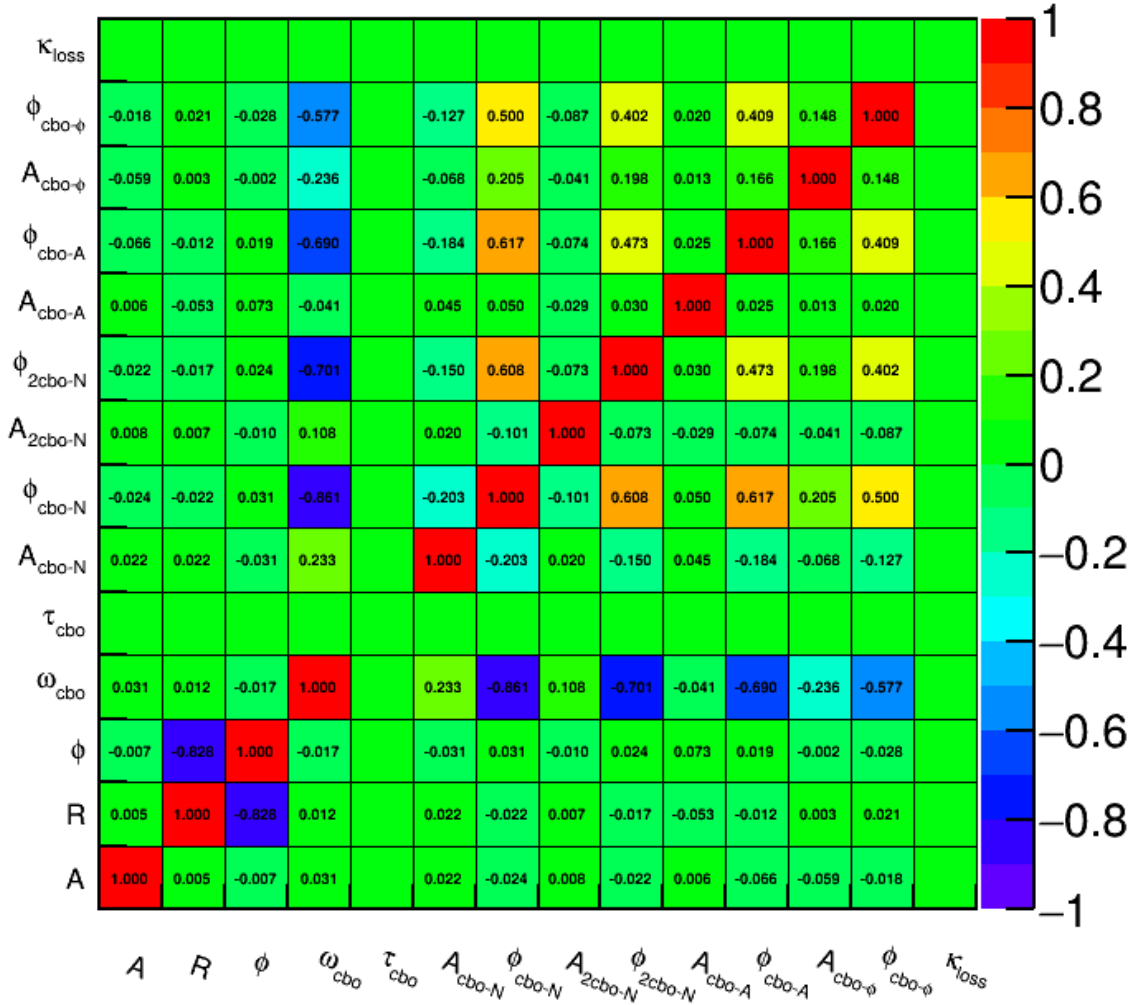


Figure D.1: Correlation matrix for the single seed ratio fit to the High-Kick dataset. The only significant correlation with  $R$  is the  $g - 2$  phase.  $\tau_{cbo}$  and  $\kappa_{loss}$  are fixed, hence the corresponding empty rows and columns.

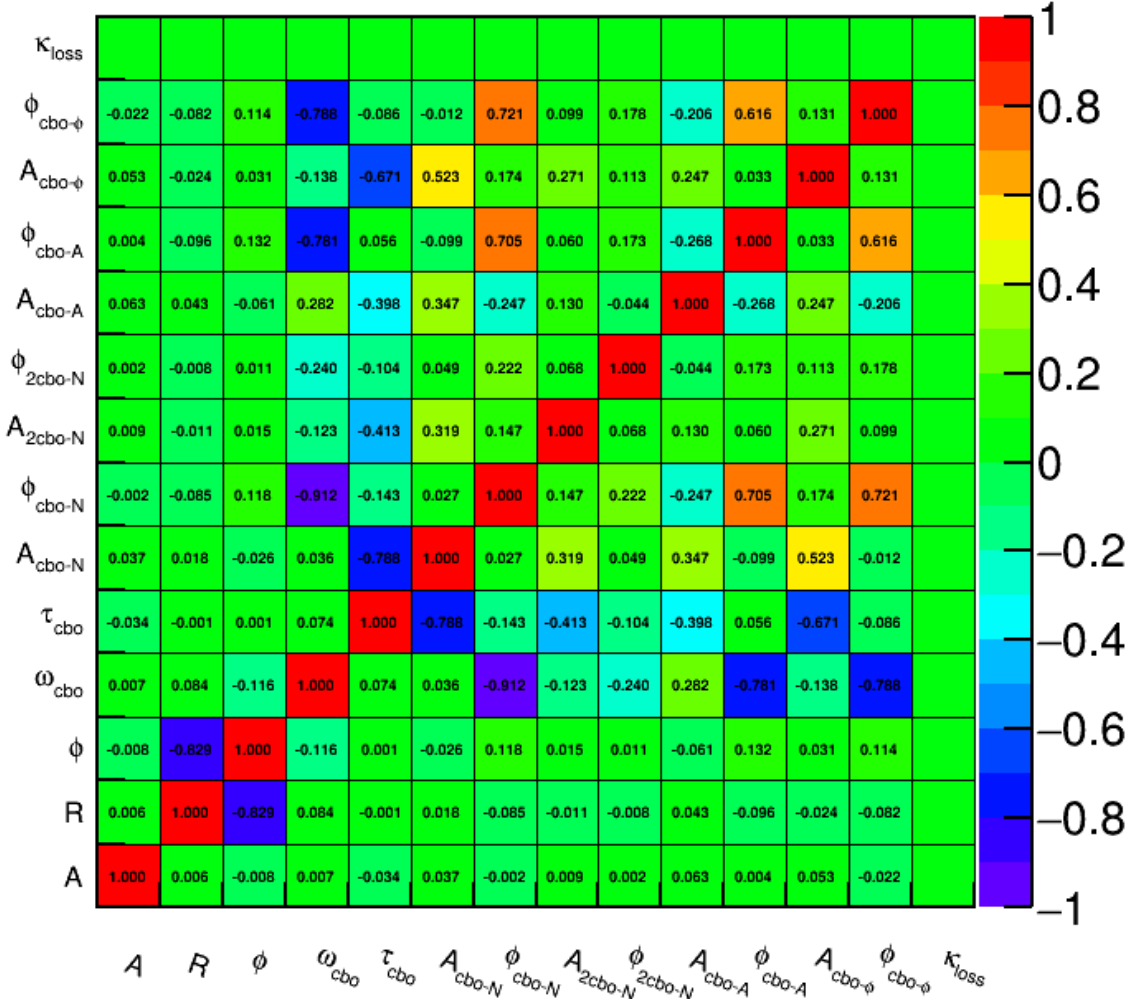


Figure D·2: Correlation matrix for the single seed ratio fit to the 9d dataset. The only significant correlation with  $R$  is the  $g-2$  phase.  $\kappa_{loss}$  is fixed, hence the corresponding empty row and column.

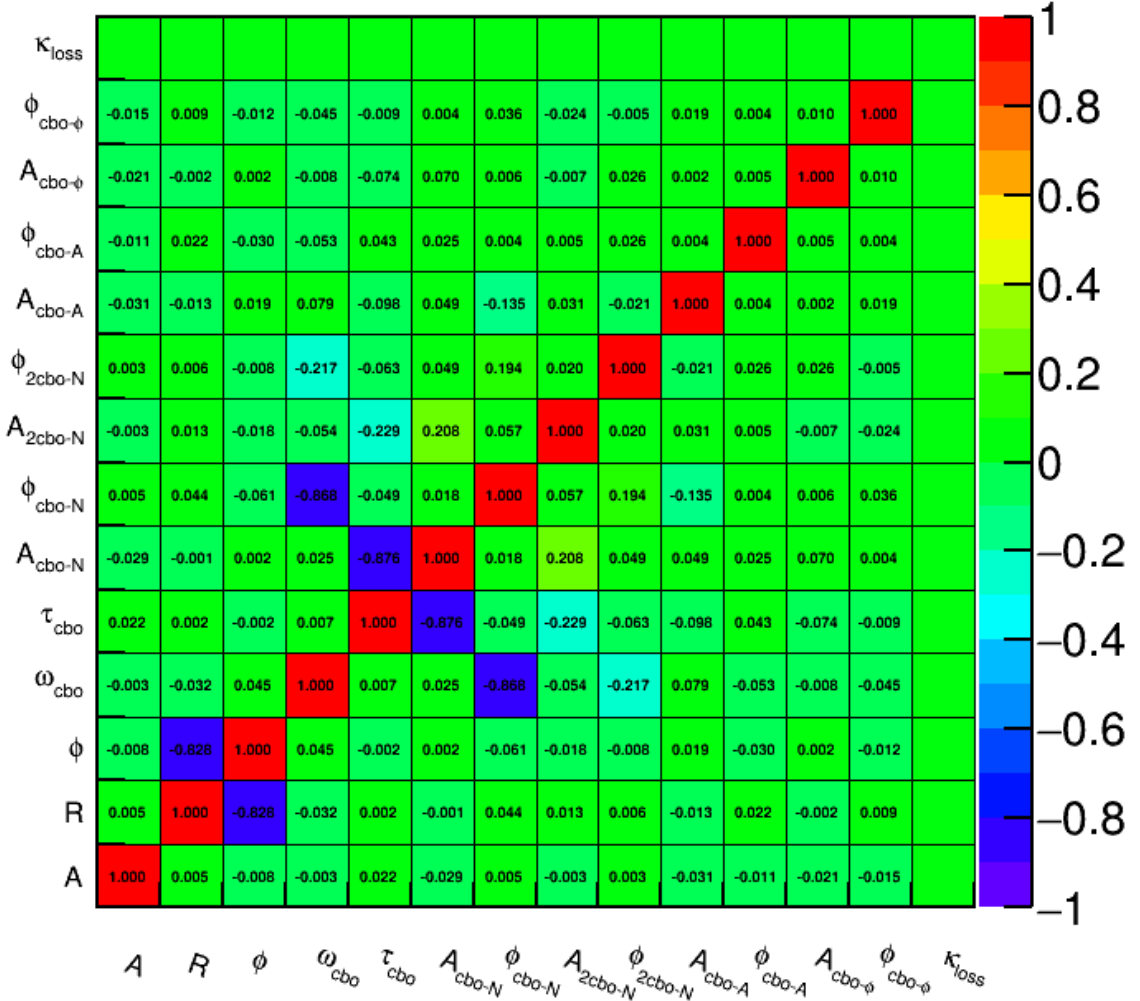


Figure D·3: Correlation matrix for the single seedratio fit to the Endgame dataset. The only significant correlation with  $R$  is the  $g - 2$  phase.  $\kappa_{loss}$  is fixed, hence the corresponding empty row and column.

# Bibliography

- [1] P. Dirac. “The quantum theory of the electron”. In: *Proceedings of the Royal Society of London Series A, Containing Papers of a Mathematical and Physical Character* (1928).
- [2] M. Schwartz. *Quantum Field Theory and the Standard Model*. Cambridge University Press, 2014.
- [3] J. E. Nafe, E. B. Nelson, and I. I. Rabi. “The Hyperfine Structure of Atomic Hydrogen and Deuterium”. In: *Phys. Rev.* 71 (12 June 1947), pp. 914–915. DOI: 10.1103/PhysRev.71.914. URL: <https://link.aps.org/doi/10.1103/PhysRev.71.914>.
- [4] Julian Schwinger. “On Quantum-Electrodynamics and the Magnetic Moment of the Electron”. In: *Phys. Rev.* 73 (4 Feb. 1948), pp. 416–417. DOI: 10.1103/PhysRev.73.416. URL: <https://link.aps.org/doi/10.1103/PhysRev.73.416>.
- [5] Joshua Ellis. “TikZ-Feynman: Feynman diagrams with TikZ”. In: *Comput. Phys. Commun.* 210 (2017), pp. 103–123. DOI: 10.1016/j.cpc.2016.08.019. arXiv: 1601.05437 [hep-ph].
- [6] Max Dohse. “TikZ-FeynHand: Basic User Guide”. In: (2018). arXiv: 1802.00689 [cs.0H].
- [7] Tatsumi Aoyama et al. “Complete Tenth-Order QED Contribution to the Muon  $g - 2$ ”. In: *Phys. Rev. Lett.* 109 (2012), p. 111808. DOI: 10.1103/PhysRevLett.109.111808. arXiv: 1205.5370 [hep-ph].
- [8] Tatsumi Aoyama, Toichiro Kinoshita, and Makiko Nio. “Revised and Improved Value of the QED Tenth-Order Electron Anomalous Magnetic Moment”. In: *Phys. Rev.* D97.3 (2018), p. 036001. DOI: 10.1103/PhysRevD.97.036001. arXiv: 1712.06060 [hep-ph].
- [9] C. Gnendiger, D. Stöckinger, and H. Stöckinger-Kim. “The electroweak contributions to  $(g - 2)_\mu$  after the Higgs boson mass measurement”. In: *Phys. Rev.* D88 (2013), p. 053005. DOI: 10.1103/PhysRevD.88.053005. arXiv: 1306.5546 [hep-ph].
- [10] Tadashi Ishikawa, Nobuya Nakazawa, and Yoshiaki Yasui. “Numerical calculation of the full two-loop electroweak corrections to muon  $(g - 2)$ ”. In: (2018). arXiv: 1810.13445 [hep-ph].

- [11] Bernd A. Kniehl. “Dispersion relations in loop calculations”. In: *Acta Phys. Polon.* B27 (1996), pp. 3631–3644. arXiv: hep-ph/9607255 [hep-ph].
- [12] F. Jegerlehner. *The Anomalous Magnetic Moment of the Muon*. Springer Tracts in Modern Physics. Springer Berlin Heidelberg, 2007. ISBN: 9783540726340. URL: <https://books.google.com/books?id=uxQj004Py6AC>.
- [13] D. Babusci et al. “Precision measurement of  $\sigma(e^+e^- \rightarrow \pi^+\pi^-\gamma)/\sigma(e^+e^- \rightarrow \mu^+\mu^-\gamma)$  and determination of the  $\pi^+\pi^-$  contribution to the muon anomaly with the KLOE detector”. In: *Phys. Lett.* B720 (2013), pp. 336–343. DOI: 10.1016/j.physletb.2013.02.029. arXiv: 1212.4524 [hep-ex].
- [14] T. Xiao et al. “Precision Measurement of the Hadronic Contribution to the Muon Anomalous Magnetic Moment”. In: *Phys. Rev.* D97.3 (2018), p. 032012. DOI: 10.1103/PhysRevD.97.032012. arXiv: 1712.04530 [hep-ex].
- [15] Bogdan Malaescu. “Measurement of hadronic cross sections at BABAR with ISR and implications for the muon  $(g-2)$ ”. In: *Proceedings, International Conference on the Structure and the Interactions of the Photon including the 20th International Workshop on Photon-Photon Collisions and the International Workshop on High Energy Photon Linear Colliders, PHOTON 2013: Paris, France, May 20-24, 2013*. 2014. arXiv: 1404.6887 [hep-ex]. URL: <http://www-public.slac.stanford.edu/sciDoc/docMeta.aspx?slacPubNumber=SLAC-PUB-16106>.
- [16] M. Ablikim et al. “Measurement of the  $e^+e^- \rightarrow \pi^+\pi^-$  cross section between 600 and 900 MeV using initial state radiation”. In: *Phys. Lett.* B753 (2016), pp. 629–638. DOI: 10.1016/j.physletb.2015.11.043. arXiv: 1507.08188 [hep-ex].
- [17] Alexander Keshavarzi, Daisuke Nomura, and Thomas Teubner. “Muon  $g - 2$  and  $\alpha(M_Z^2)$ : a new data-based analysis”. In: *Phys. Rev.* D97.11 (2018), p. 114025. DOI: 10.1103/PhysRevD.97.114025. arXiv: 1802.02995 [hep-ph].
- [18] Michel Davier et al. “Reevaluation of the hadronic vacuum polarisation contributions to the Standard Model predictions of the muon  $g - 2$  and  $\alpha(m_Z^2)$  using newest hadronic cross-section data”. In: *Eur. Phys. J.* C77.12 (2017), p. 827. DOI: 10.1140/epjc/s10052-017-5161-6. arXiv: 1706.09436 [hep-ph].
- [19] T. Blum et al. “Calculation of the Hadronic Vacuum Polarization Contribution to the Muon Anomalous Magnetic Moment”. In: *Phys. Rev. Lett.* 121 (2 July 2018), p. 022003. DOI: 10.1103/PhysRevLett.121.022003. URL: <https://link.aps.org/doi/10.1103/PhysRevLett.121.022003>.
- [20] Gilberto Colangelo et al. “Dispersive approach to hadronic light-by-light scattering”. In: *JHEP* 09 (2014), p. 091. DOI: 10.1007/JHEP09(2014)091. arXiv: 1402.7081 [hep-ph].

- [21] Gilberto Colangelo et al. “Dispersion relation for hadronic light-by-light scattering: theoretical foundations”. In: *JHEP* 09 (2015), p. 074. DOI: 10.1007/JHEP09(2015)074. arXiv: 1506.01386 [hep-ph].
- [22] Gilberto Colangelo et al. “Rescattering effects in the hadronic-light-by-light contribution to the anomalous magnetic moment of the muon”. In: *Phys. Rev. Lett.* 118.23 (2017), p. 232001. DOI: 10.1103/PhysRevLett.118.232001. arXiv: 1701.06554 [hep-ph].
- [23] Thomas Blum et al. “Lattice Calculation of Hadronic Light-by-Light Contribution to the Muon Anomalous Magnetic Moment”. In: *Phys. Rev.* D93.1 (2016), p. 014503. DOI: 10.1103/PhysRevD.93.014503. arXiv: 1510.07100 [hep-lat].
- [24] Thomas Blum et al. “Connected and Leading Disconnected Hadronic Light-by-Light Contribution to the Muon Anomalous Magnetic Moment with a Physical Pion Mass”. In: *Phys. Rev. Lett.* 118.2 (2017), p. 022005. DOI: 10.1103/PhysRevLett.118.022005. arXiv: 1610.04603 [hep-lat].
- [25] Thomas Blum et al. “Using infinite volume, continuum QED and lattice QCD for the hadronic light-by-light contribution to the muon anomalous magnetic moment”. In: *Phys. Rev.* D96.3 (2017), p. 034515. DOI: 10.1103/PhysRevD.96.034515. arXiv: 1705.01067 [hep-lat].
- [26] Nils Asmussen et al. “Hadronic light-by-light scattering in the anomalous magnetic moment of the muon”. In: *15th International Workshop on Tau Lepton Physics (TAU2018) Amsterdam, Netherlands, September 24-28, 2018*. 2018. arXiv: 1811.08320 [hep-lat].
- [27] Andreas Nyffeler. “Precision of a data-driven estimate of hadronic light-by-light scattering in the muon  $g - 2$ : Pseudoscalar-pole contribution”. In: *Phys. Rev.* D94.5 (2016), p. 053006. DOI: 10.1103/PhysRevD.94.053006. arXiv: 1602.03398 [hep-ph].
- [28] B. Lee Roberts. “The History of the Muon ( $g - 2$ ) Experiments”. In: *15th International Workshop on Tau Lepton Physics (TAU2018) Amsterdam, Netherlands, September 24-28, 2018*. 2018. arXiv: 1811.06974 [hep-ex].
- [29] G. W. Bennett et al. “Final Report of the Muon E821 Anomalous Magnetic Moment Measurement at BNL”. In: *Phys. Rev.* D73 (2006), p. 072003. DOI: 10.1103/PhysRevD.73.072003. arXiv: hep-ex/0602035 [hep-ex].
- [30] Peter J. Mohr, David B. Newell, and Barry N. Taylor. “CODATA recommended values of the fundamental physical constants: 2014”. In: *Rev. Mod. Phys.* 88 (3 Sept. 2016), p. 035009. DOI: 10.1103/RevModPhys.88.035009. URL: <https://link.aps.org/doi/10.1103/RevModPhys.88.035009>.

- [31] D. Hanneke, S. Fogwell, and G. Gabrielse. “New Measurement of the Electron Magnetic Moment and the Fine Structure Constant”. In: *Phys. Rev. Lett.* 100 (2008), p. 120801. DOI: 10.1103/PhysRevLett.100.120801. arXiv: 0801.1134 [physics.atom-ph].
- [32] Richard H. Parker et al. “Measurement of the fine-structure constant as a test of the Standard Model”. In: *Science* 360.6385 (2018), pp. 191–195. ISSN: 0036-8075. DOI: 10.1126/science.aap7706. eprint: <https://science.sciencemag.org/content/360/6385/191.full.pdf>. URL: <https://science.sciencemag.org/content/360/6385/191>.
- [33] L. Roberts. Personal communication. 2019.
- [34] J. Jackson. *Classical Electrodynamics*. Wiley Indiana, 2011.
- [35] W. Liu et al. “High Precision Measurements of the Ground State Hyperfine Structure Interval of Muonium and of the Muon Magnetic Moment”. In: *Phys. Rev. Lett.* 82 (4 Jan. 1999), pp. 711–714. DOI: 10.1103/PhysRevLett.82.711. URL: <https://link.aps.org/doi/10.1103/PhysRevLett.82.711>.
- [36] E. D. Commins and P. H. Bucksbaum. *Weak interactions of leptons and quarks*. Cambridge University Press, 1983.
- [37] G. W. Bennett et al. “Statistical equations and methods applied to the precision muon ( $g - 2$ ) experiment at BNL”. In: *Nucl. Instrum. Meth.* A579 (2007), pp. 1096–1116. DOI: 10.1016/j.nima.2007.06.023.
- [38] J. Grange et al. “Muon ( $g - 2$ ) Technical Design Report”. In: (2015). arXiv: 1501.06858 [physics.ins-det].
- [39] R. Osofsky. *Improving Magnetic Field Uniformity in the Muon  $g - 2$  Storage Ring*. Muon  $g - 2$  DocDB 12497. 2018.
- [40] M. Tanabashi et al. “Review of Particle Physics”. In: *Phys. Rev. D* 98 (3 Aug. 2018), p. 030001. DOI: 10.1103/PhysRevD.98.030001. URL: <https://link.aps.org/doi/10.1103/PhysRevD.98.030001>.
- [41] Dikty Stratakis et al. “Accelerator performance analysis of the Fermilab Muon Campus”. In: *Phys. Rev. Accel. Beams* 20.11 (2017), p. 111003. DOI: 10.1103/PhysRevAccelBeams.20.111003. arXiv: 1803.00597 [physics.acc-ph].
- [42] Cary Yoshikawa et al. “Optimization of the Target Subsystem for the New  $g - 2$  Experiment”. In: (Jan. 2013).
- [43] A. Yamamoto et al. “The superconducting inflector for the BNL  $g - 2$  experiment”. In: *Nucl. Instrum. Meth.* A491 (2002), pp. 23–40. DOI: 10.1016/S0168-9002(02)01232-9.
- [44] Y. K. Semertzidis et al. “The Brookhaven muon ( $g - 2$ ) storage ring high voltage quadrupoles”. In: *Nucl. Instrum. Meth.* A503 (2003), pp. 458–484. DOI: 10.1016/S0168-9002(03)00999-9.

- [45] H. Wiedermann. *Particle Accelerator Physics*. Springer-Verlag New York, 1993.
- [46] D. Seleznev, A. Chapelain, and D. Rubin. *Extraction of the Muon Beam Frequency Distribution via the Fourier Analysis of the Fast Rotation Signal*. Muon  $g - 2$  Note 130 DocDB 9701. 2018.
- [47] A. Keshavarzi. *Fast rotation summary*. Muon  $g - 2$  DocDB 15304. 2018.
- [48] M. J. Syphers. *Storage Ring Linear Tune Tables*. Muon  $g - 2$  DocDB 11547. 2018.
- [49] A. Chapelain. *Data Quality Control - a.k.a. DQC*. Muon  $g - 2$  DocDB 15295. 2018.
- [50] H. Binney et al. *Data Quality Control for the 60-Hour Dataset*. Muon  $g - 2$  DocDB 16568. 2019.
- [51] K. Khaw. *How each dataset is different for Run 1 of E989*. Muon  $g - 2$  DocDB 15781. 2019.
- [52] H. Binney. *T0: update and current work*. Muon  $g - 2$  DocDB 10162. 2018.
- [53] A. Fienberg. *T0 Detector*. Muon  $g - 2$  DocDB 10911. 2018.
- [54] P. Kammel et al. *Inflector Beam Monitoring System Justification Document*. Muon  $g - 2$  DocDB 2722. 2015.
- [55] B. MacCoy and P. Kammel. *IBMS Update*. Muon  $g - 2$  DocDB 10944. 2018.
- [56] F. Gray. *Fiber Harp Beam Monitor*. Muon  $g - 2$  DocDB 8366. 2017.
- [57] A. T. Fienberg et al. “Studies of an array of PbF<sub>2</sub> Cherenkov crystals with large-area SiPM readout”. In: *Nucl. Instrum. Meth.* A783 (2015), pp. 12–21. DOI: 10.1016/j.nima.2015.02.028. arXiv: 1412.5525 [physics.ins-det].
- [58] J. Kaspar et al. “Design and performance of SiPM-based readout of PbF<sub>2</sub> crystals for high-rate, precision timing applications”. In: *JINST* 12.01 (2017), P01009. DOI: 10.1088/1748-0221/12/01/P01009. arXiv: 1611.03180 [physics.ins-det].
- [59] David A. Sweigart. “A new MicroTCA-based waveform digitizer for the Muon  $g - 2$  experiment”. In: *PoS ICHEP2016* (2016), p. 845. DOI: 10.22323/1.282.0845. arXiv: 1612.05145 [physics.ins-det].
- [60] A. Anastasi et al. “The laser control of the muon  $g - 2$  experiment at Fermilab”. In: *JINST* 13.02 (2018), T02009. DOI: 10.1088/1748-0221/13/02/T02009.
- [61] S. Charity. “Beam profile measurements using the straw tracking detectors at the Fermilab muon  $g - 2$  experiment, and a study of their sensitivity to a muon electric dipole moment”. PhD thesis. University of Liverpool, 2018.
- [62] W. Blum, W. Riegler, and L. Rolandi. *Particle Detection with Drift Chambers*. Springer-Verlag Berlin Heidelberg, 2008.

- [63] M. Raminsky. *Garfield*. Muon  $g - 2$  DocDB 905. 2012.
- [64] J. Mott. *Garfield Parameterisation: First Simulation Attempt*. Muon  $g - 2$  DocDB 6171. 2017.
- [65] W. Turner. “The construction and commissioning of the straw tracking detector in the new muon  $g - 2$  experiment at Fermilab”. PhD thesis. University of Liverpool, 2018.
- [66] C. Green et al. “The Art Framework”. In: *J. Phys. Conf. Ser.* 396 (2012), p. 022020. DOI: 10.1088/1742-6596/396/2/022020.
- [67] T. Walton. *Track Finding Overview*. Muon  $g - 2$  DocDB 7580. 2017.
- [68] T. Walton and J. Price. *Track formation details*. Muon  $g - 2$  DocDB 8555. 2017.
- [69] J. Price. *Track Finding - simple pattern recognition*. Muon  $g - 2$  DocDB 5793. 2017.
- [70] N. Kinnaird. *Geane Track Fitting*. Muon  $g - 2$  Note 184 DocDB 8102. 2017.
- [71] V. Innocente, M. Maire, and E. Nagy. “GEANE: Average tracking and error propagation package”. In: *MC 91: Detector and event simulation in high-energy physics. Proceedings, Workshop, Amsterdam, Netherlands, April 8-12, 1991*. 1991, pp. 58–78. URL: [http://innocentonnice.web.cern.ch/innocentonnice/napol99/geane\\_manual.ps](http://innocentonnice.web.cern.ch/innocentonnice/napol99/geane_manual.ps).
- [72] Lia Lavezzi. “The fit of nuclear tracks in high precision spectroscopy experiments”. pp. 57-86. PhD thesis. Pavia U., 2007. URL: [http://bamboo.infn.it/doc/L\\_Lavezzi.pdf](http://bamboo.infn.it/doc/L_Lavezzi.pdf).
- [73] K. Lassila-Perini and L. Urban. “Energy loss in thin layers in GEANT”. In: *Nucl. Instrum. Meth.* A362 (1995), pp. 416–422. DOI: 10.1016/0168-9002(95)00344-4.
- [74] A. Strandlie and W. Wittek. “Derivation of Jacobians for the propagation of covariance matrices of track parameters in homogeneous magnetic fields”. In: *Nucl. Instrum. Meth.* A566 (2006), pp. 687–698.
- [75] V. Innocente and E. Nagy. “Trajectory fit in presence of dense materials”. In: *Nucl. Instrum. Meth.* A324 (1993), pp. 297–306. DOI: 10.1016/0168-9002(93)90992-Q.
- [76] J. Mott, N. Kinnaird, and F. Azfar. *Residuals, Covariance & Correlation in Fitting Straight Line Tracks in UV*. Muon  $g - 2$  DocDB 3813. 2016.
- [77] Gaël Guennebaud, Benoît Jacob, et al. *Eigen v3*. <http://eigen.tuxfamily.org>. 2010.
- [78] N. Kinnaird. *Left/Right - What we do/have at the moment*. Muon  $g - 2$  DocDB 12017. 2018.

- [79] J. Price. *LR from wire fit*. Muon  $g - 2$  DocDB 6947. 2017.
- [80] J. Price and S. Charity. *Extrapolation uncertainty*. Muon  $g - 2$  DocDB 14920. 2018.
- [81] J. Mott. *Track Quality Cuts*. Muon  $g - 2$  DocDB 16282. 2019.
- [82] J. Mott. *Track Quality Cuts: Second Edition*. Muon  $g - 2$  DocDB 16420. 2019.
- [83] J. Mott et al. *CBO Frequency Change*. Muon  $g - 2$  DocDB 14208. 2018.
- [84] A. Fienberg. “Measuring the Precession Frequency in the E989 Muon  $g - 2$  Experiment”. PhD thesis. University of Washington, 2019.
- [85] W. Gohn. “Data Acquisition with GPUs: The DAQ for the Muon  $g - 2$  Experiment at Fermilab”. In: *PoS ICHEP2016* (2016), p. 174. doi: 10.22323/1.282.0174. arXiv: 1611.04959 [physics.ins-det].
- [86] A. Driutti et al. *Status of the STDP module and of the new IFG correction functions*. Muon  $g - 2$  DocDB 16003. 2019.
- [87] C. Ozben and Y. Semertzidis. *Eliminating Pileup from the  $g - 2$  Data*. E821 Muon  $g - 2$  Note 365. 2000.
- [88] J. Kindem. “The anomalous magnetic moment of the positive muon”. PhD thesis. University of Minnesota, 1998.
- [89] L. Duong. “A Precise Measurement of the Anomalous Magnetic Moment of the Positive Muon”. PhD thesis. University of Minnesota, 2001.
- [90] J. Paley. “Measurement of the Anomalous Magnetic Moment of the Negative Muon to 0.7 Parts Per Million”. PhD thesis. Boston University, 2004.
- [91] K. Labe. *E989 Clock System Manual*. 0.1. Muon  $g - 2$  DocDB 10995 v2. Cornell University. Mar. 2018.
- [92] L. Gibbons. *Binders: C++ class for blinding fits*. Muon  $g - 2$  DocDB 11232. 2018.
- [93] J. Mott. *CBO Frequency during EndGame dataset*. Muon  $g - 2$  Elogs Tracking Analysis ID 184. 2019.
- [94] J. Mott. *Personal communication*. 2019.
- [95] N. Kinnaird and J. Mott. *The Vertical Waist in the Ratio Method Analysis*. Muon  $g - 2$  Note 214 DocDB 19466. 2019.
- [96] T. Halewood-Leagas and J. Price. *Vertical Betatron Oscillations*. Muon  $g - 2$  DocDB 12894. 2018.
- [97] Jason Crnkovic et al. “Lost Muon Study for the Muon  $g - 2$  Experiment at Fermilab”. In: *Proceedings, 8th International Particle Accelerator Conference (IPAC 2017): Copenhagen, Denmark, May 14-19, 2017*. 2017, WEPIK119. doi: 10.18429/JACoW-IPAC2017-WEPIK119.

- [98] S. Ganguly. *Muon Losses - an Overview*. Muon  $g - 2$  DocDB 12912. 2018.
- [99] K. Labe. *Studying Muon Losses with Recon East*. Muon  $g - 2$  Note 188 DocDB 17695. 2019.
- [100] N. Kinnaird. *Analysis Note for 60H Dataset Relative Unblinding*. Muon  $g - 2$  Note 172 DocDB 16270. 2019.
- [101] F. Farley et al. *Estimation of Error in Differential Pileup Subtracted Data*. E821 Muon  $g - 2$  Note 377. 2000.

# Nicholas Kinnaird

512-922-0534 | nickkinn@bu.edu | 205 N Oakhurst Dr, Aurora, IL

## 6.1 Education

**Boston University**  
*Ph.D. in Physics*

Boston, MA  
2019

**Dissertation:** Measurement of the Magnetic Anomaly of the Muon to X parts per billion  
in Run 1 of the Fermilab Muon  $g - 2$  Experiment

**Boston University**  
*M.A. in Physics*

Boston, MA  
2016

**University of Texas at Austin**  
*B.S. in Physics*

Austin, TX  
2013

**University of Texas at Austin**  
*B.S. in Mathematics*

Austin, TX  
2013